Worcester Polytechnic Institute
Digital WPI

Masters Theses (All Theses, All Years) | Electronic Theses and Dissertations

2013-04-16

Multi-wavelength characterization of cadmium telluride solar cell: Development of Q-EBIC and NSOM measurement techniques

Anthony Giacomo Gianfrancesco
Worcester Polytechnic Institute

Follow this and additional works at: https://digitalcommons.wpi.edu/etd-theses

Repository Citation
Gianfrancesco, Anthony Giacomo, "*Multi-wavelength characterization of cadmium telluride solar cell: Development of Q-EBIC and NSOM measurement techniques*" (2013). *Masters Theses (All Theses, All Years)*. 213.
https://digitalcommons.wpi.edu/etd-theses/213

This thesis is brought to you for free and open access by Digital WPI. It has been accepted for inclusion in Masters Theses (All Theses, All Years) by an authorized administrator of Digital WPI. For more information, please contact wpi-etd@wpi.edu.

Multi-wavelength characterization of cadmium telluride solar cell: Development of Q-EBIC and NSOM measurement techniques

Submitted to the Faculty of the

WORCESTER POLYTECHNIC INSTITUTE

Department of Physics

in partial fulfillment of the requirements for the

Degree of Master of Science

By

Anthony Giacomo Gianfrancesco

Date: April 12, 2013

Dr. Nancy A. Burnham, Advisor

Dr. L. R. Ram-Mohan, Committee Member

Dr. R. S. Quimby, Committee Member

Abstract

Thin-film inorganic solar cells, such as CdTe ($E_g \approx 1.4$ eV), have demonstrated the most promise to date for a viable low-cost renewable energy resource. Their current performance, however, is far from the theoretical limit suffering from significant charge recombination losses due to grain boundaries and point defects. It is likely that the microscopic compositions of grain bulk and grain boundaries are significantly different and not optimal for the overall device performance. Good understanding of charge transport along and across the grain boundaries and other microscopic interfaces is lacking, preventing the development of reliable and predictive device models. The insufficient microscopic understanding hinders efficient characterization of photovoltaic materials and also holds back the development of process control techniques. We first show preliminary results for a novel technique, quantum-dot electron-beam induced current (Q-EBIC) to characterize semiconductors in the near-field. We also propose the use of near-field optical scanning microscopy (NSOM) for high precision optical excitation and for local, high-resolution characterization. The most important nanoscale phenomena being the separation of compositional and electrical effects. These imaging techniques are examined with the goal of synthesizing information obtained by both methods, Q-EBIC and NSOM, of material phenomena at the relevant length scales, to other measurement methods.

Contributions

In this section, I would like to mention my explicit contribution to the projects written in this thesis. In the Q-EBIC portion of the project, I helped obtain preliminary results for quantum dot deposition on a cadmium telluride solar cell. I also provided atomic force microscopy inspection of self-assembled quantum dots.

I performed a majority of the dip-coating procedure, with some help from H. P. Yoon, as well as calibration of the dip-coating machine used for this experiment. The cathodoluminescence, photoluminescence, and electron beam induced current measurements were performed by H. P. Yoon. The fabrication of cross-section and top-view devices were fabricated also by H. P. Yoon.

The other experiment in this thesis is the multi-wavelength near-field scanning optical microscopy. In this experiment, M. S. Leite and I helped assemble the optical configuration for the Fianium Supercontinuum laser. I helped fabricate some devices with e-beam deposition, while cross-section samples were fabricated using focused-ion beam milling by M. S. Leite. Data acquisition of multi-wavelength results were both completed by M. S. Leite and me.

Contents

List of Figures

1 Introduction

Energy demand of the world's largest nations grows significantly every year, and it is projected to increase over one-third by 2035. Despite the growth in low-carbon sources in 2011, fossil fuels remained a dominant industry that amounted to $523 billion, rising almost 30% from 2010 [1]. Fossil fuels, oil, coal, and natural gas, are the main sources for world energy demand. These non-renewable sources of energy will not last forever, in fact, a formula for calculating fossil fuel reserve depletion rate has been derived. This predicts that the fossil fuel reserve depletion times for oil, coal, and gas are approximately 35, 107, and 37 years, respectively [2]. These numbers present a dire situation that requires action from renewable energy technology enthusiasts.

Developing a reliable renewable energy generation system is important for quenching of the continuous thirst of energy demand. Though this task may seem daunting, preliminary results from the Renewable Electricity Futures study from the National Renewable Energy Laboratory indicates that renewable generation could play a more significant role in the United States electricity system than previously thought and that further work is warranted to investigate this clean generation pathway [3]. An initial investigation of the energy demands faced by the United States over the next few decades and examination the logistics of a large amount of electricity production coming from renewable sources was studied. It is claimed that by the year 2050, our current technology is sufficient enough to provide the entire United States with 80% renewable electricity production. It is evident that this study provides the motivation for maintaining interest in solar technology as a viable renewable electricity source.

Today, commercial solar modules (thin film solar cells) are made of a single layer of semiconductor material. The best available thin film solar cells are monocrystalline silicon solar cells which can reach efficiencies greater than 17% [4]. Though they are very efficient, purifying silicon to attain such high quality, uniform solar cells is incredibly expensive. These solar cells are not typically used in large-scale photovoltaic (PV) module applications because

of their large initial cost and lengthy payback period [5].

The best choice for PV material in a large scale solar cell application is a polycrystalline material such as polycrystalline silicon, cadmium telluride (CdTe), or copper indium gallium selenide (CIGS). Though polycrystalline solar cells are inherently full of defects because of their composition and growth methods, however their efficiency loss is offset by cost effectiveness. These materials are much cheaper to fabricate, when compared to the fabrication process of crystalline, or bulk, materials. Thin-film solar cells allow for high-speed, large area deposition of a semiconductor onto any substrate of choice, without an expensive, time-consuming purification process [5].

Currently, the only PV material to rival polycrystalline silicon in terms of cost for solar module application is CdTe. Cadmiun telluride p-layer does not abosorb the less abundant infrared photons from the sun, but does absorb the more abundant visible spectrum. The direct band gap and high absorption of CdTe over wide range of visible wavelengths is a near match to the solar spectrum. The more intense short-wavelength, ultra-violet and green light, from the sun is absorbed near the surface of CdTe, making it a perfect absorbing layer for thin-film photovoltaics [6]. Recent technological advances in commercial fabrication of CdTe polycrystalline PV have produced a solar module that reaches 14.4% total module efficiency. This achievement came shortly after First Solar achieved a solar cell efficiency of 17.3% [4]. Though these are record breaking efficiencies, they are still far from the theoretical maximum efficiency of 28% [6].

Typically, imperfections in a lattice are cause for a loss in overall device performance. This is especially true in the case of polycrystalline materials. The presence of grains with different crystallographic orientations introduces imperfections such as dislocations, vacancies, and distorted bonds at the interfaces, among other defects in the crystal lattice. The interfaces between grains where deformities are present normally are thought of as performance inhibiting characteristics, however, in the case of CdTe these imperfections are the cause for an introduction of electronic states and significant band bending. The effects of these defects

are not easy to separate and it is difficult to pin-point each type of imperfections' individual contribution to efficiency loss [7].

The physical characteristics of solar cells, specifically CdTe, have been probed under the effect of external forces, such as high temperature, stress/strain, and treatments, at various length scales. The most important characteristics that are probed will be discussed later in the background, Chapter 2, to motivate the analysis performed in this thesis. Chapter 2 will also define all of the necessary terms needed to understand the results of this thesis, as well as the results from experiments from other groups. After the background chapter, the methodology will be briefly outlined with a more detailed methodology included in the Appendix. The sequential chapters will introduce the data obtained and subsequent analysis. The thesis will then close with a description of further experimentation and analysis.

2 Background

In order to understand the methodology and results presented in this thesis, a brief synopsis of solar cell devices will be presented, while highlighting the overall physical processes involved. The material focused upon in the following chapters is CdTe, which was used in all of the experiments in this thesis. The last section of this chapter includes a summary of the results from other groups also working on the characterization of CdTe.

2.1 Definitions of Terms

The most important parameters of a semiconductor material for solar cell operation are the band gap, the absorption of incident light, and the generation and recombination of free carriers (electrons and holes) in response to incident light. As mentioned previously, joining a p-doped and n-doped semiconductor creates a p-n junction. In Fig. 1, a cadmium telluride p-layer is on top of a cadmium sulfide n-layer, to create a p-n junction. When the two semiconductors are joined, free carriers diffuse until the concentration of electrons and holes are the same across the junction. This area of neutral charge is defined as the depletion region. When the electrons and holes diffuse they leave behind cores, which are fixed to the crystal lattice. These ion cores create an electric field preventing other free carriers from crossing the depletion region. However, even at thermal equilibrium, some carriers have enough energy to cross the depletion region [8].

Electron-hole pairs are formed when an electron bound to the crystal lattice is given enough energy to become a free carrier. The energy required to form an electron-hole pair is defined as the band gap and is intrinsic to each material. The band gap for cadmium telluride is around 1.4 electron volts (eV) at room temperature. For the application of solar cells, the majority of the electron-hole generation comes from photons. Using Planck's constant and the speed of light, we can see that 1.4 eV corresponds to a wavelength of around 886 nm. This means that a photon corresponding to an energy below the band gap, or wavelength

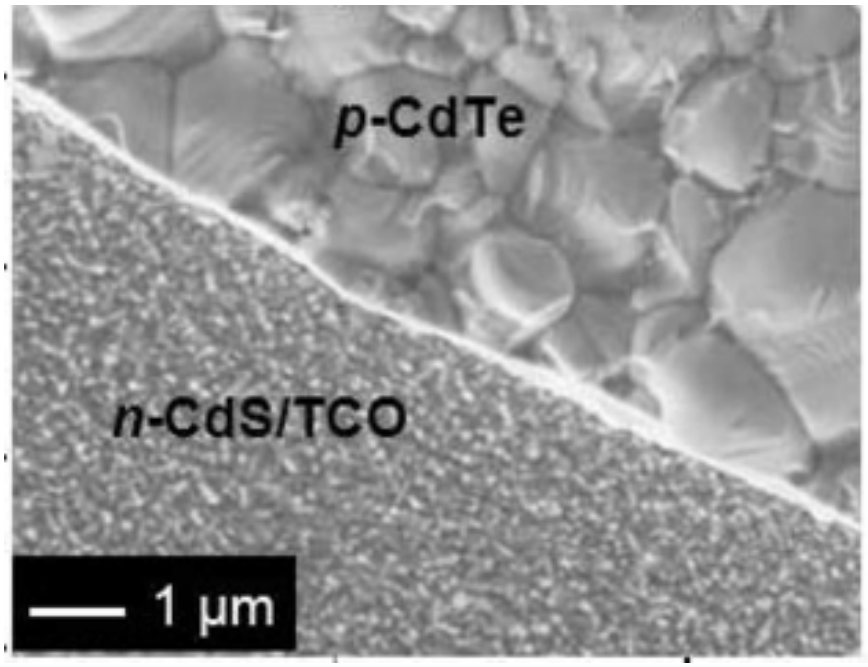

Figure 1: A scanning electron microscope (SEM) image of a p-layer CdTe from the top and an n-layer CdS. Placing these two materials adjacent to one-another produces a p-n junction. TCO here means transparent conducting oxide, used to carry away generated current. [9].

above 886 nm, should produce no electron hole pairs.

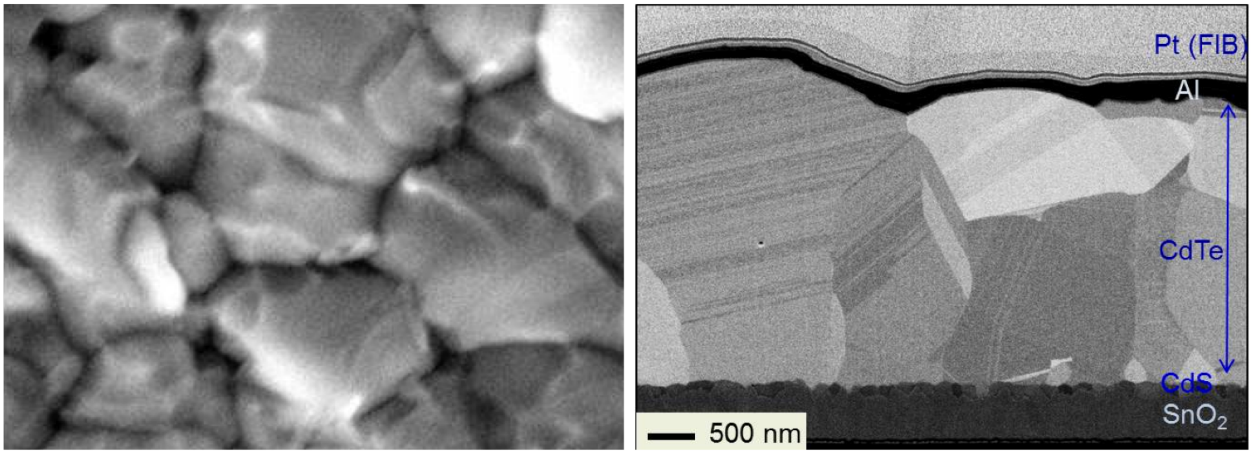

Figure 2: Left) Scanning electron microscope (SEM) image of a CdTe substrate from the top. It is easy to see in this image that the large gray shapes are the grains and the darker lines are the grain boundaries. The scale bar for this image is the same as that for the image on the right. Right) SEM image of a cross-section of a CdTe solar cell. Here we can clearly see the grain structure once again. The grains are different colors because the grains have different crystal orientations.

Polycrystalline solar cells are named as such because of their composition. They are made up of crystal structures with 'crystallographic misorientation' between them. Each crystal structure is a grain and the regions between them, or misorientations, are more commonly known as grain boundaries. Depending upon the technique of deposition, the grain size can vary from 3 μm to 0.2 μm. Grain boundaries can be thought of as discontinuities in the bulk lattice, therefore they hinder the performance of the solar cell as a whole [10]. It is a rather intuitive principle that imperfections in a system will decrease efficiency, however, a polycrystalline CdTe solar cell can be more efficient than its bulk, crystalline counterpart [6][10].

2.1.1 Thin Film Polycrystalline Solar Cells

The material investigated in this paper, as suggested by the introduction, is a thin film cadmium telluride (CdTe) p-n junction. The typical set up of a thin-film polycrystalline solar cell is shown below in Fig. 3. The typical cadmium telluride thin-film solar cell has a window layer and an absorbing layer. The device structure starts off with a glass "superstrate" which provides structural integrity to the CdTe device. This is usually followed by an anti-reflective coating (not shown in the figure). The next layer in the device is a transparent but electrically conductive layer called a transparent conducting oxide or TCO. In Fig. 3 this is shown as $SnO_2Cd_2SnO_4$ a highly resistive TCO layer. However, this can be made from other materials, such as indium tin oxide (ITO), fluorine doped tin oxide (FTO), and doped zinc oxide. There has also been research in using carbon nanotube networks and graphene, which can be fabricated to be highly transparent to infrared light [6].

The next step in creating the thin film solar cell is the window layer, which is a 50 nm thick, negatively charged cadmium sulfide layer (n-layer). The act of putting these two layers together creates an electric field, which causes very interesting phenomena that are typical of any p-n junction. The next layer in the structure is a relatively thick cadmium telluride layer which can range from 1 μm to 8 μm. The CdTe solar cell in this thesis is approximately 4-5

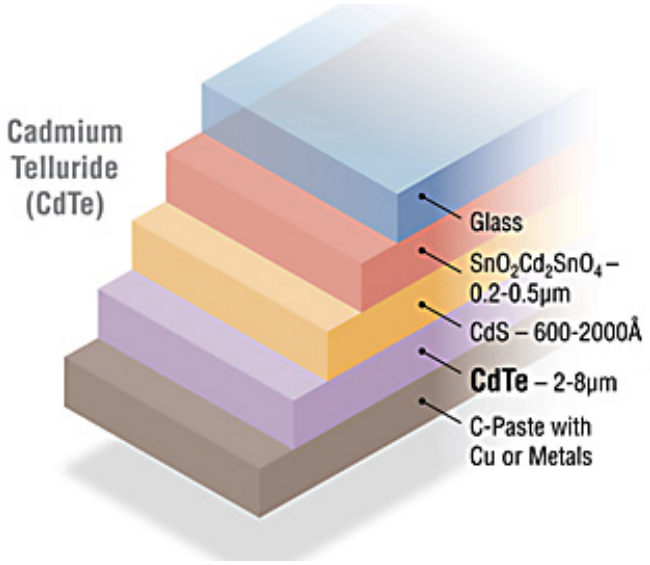

Figure 3: Schematic illustration of a typical CdTe superstrate thin-film PV device. In this design, the layers of the device are deposited onto a glass "superstrate" that allows sunlight to enter. The sunlight passes through the glass and produces electrical current and voltage in the lower layers. The world-record CdTe device from the National Renewable Energy Laboratory is based on this structure and demonstrates a conversion efficiency of 17.0% [11].

micronμm s thick and is positively charged (p-layer). Placing these two materials together creates a p-n junction, the physics of which have been studied since its invention in 1939. The next layer in the device is a copper (Cu) paste with a glass layer on top for structural support [12].

A measure of the current as a function of voltage (j-V curve) is the best way to obtain a general understanding of overall device performance. In fact, an j-V curve is the standard for measuring device performance on the research scale and commercial scale. Performing this measurement under illumination is typically called a *light* j-V and without any illumination is called a *dark* j-V. Figure 4 shows j-V curves with different surface treatments, explained in more detail later. It is favorable for a j-V curve to have a large area, this area is known as the fill factor (FF), calculated from the dark j-V curve. To obtain a good approximation of the power that a cell can provide FF must be multiplied by two more terms, found from the light j-V curve. Short circuit current, I_{sc}, is the value of current when no bias is applied and open circuit voltage, V_{oc}, is the voltage at which the current through the device is zero.

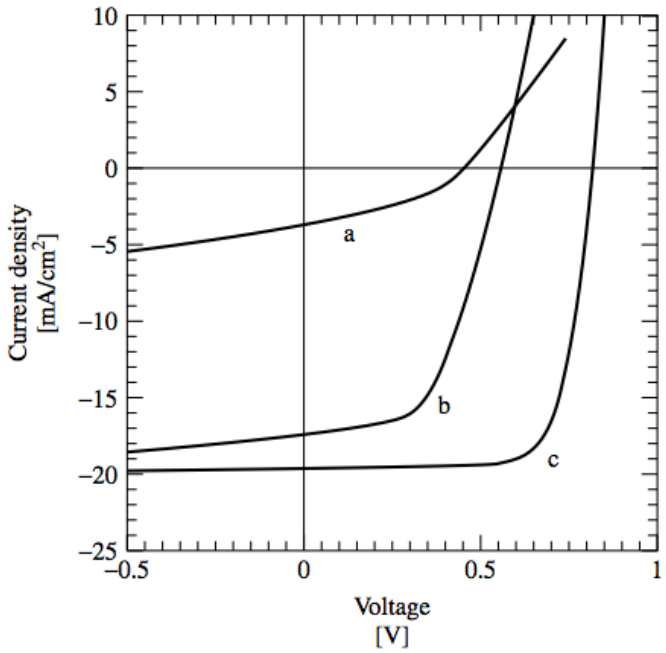

Figure 4: J-V curves, under illumination, of physical vapor deposition (PVD) devices with Cu_2Te/C contacts and different processing; (a) no heat treatment; (b) treatment at 550^o C for 5 min in air; (c) treatment in $CdCl_2$ vapor at 420^o C for 20 min in air [6].

Using these three numbers a device is given macroscopic number describing it as a whole, allowing it to be compared with other devices [13].

Typically, some sort of surface treatment is performed on the surface of CdTe to increase solar cell performance. It has been shown [6] that either treatment by air or cadmium chloride increases device performance. It has been shown that the introduction of chlorine and heat treatment to the CdTe/CdS structure can promote recrystallization and grain growth in films with submicrometer initial size. When the film has relatively large initial grain size, annealed prior to $CdCl_2$, film randomization of crystal orientation is the predominant effect. However, with small sized grains grown at lower temperatures than the former, the grains coalesce into larger structures with similar grain orientation [14]. Also, the $CdCl_2$ changes electronic properties and device performance. Figure 4 shows how different treatments can alter the device performance. The untreated device, (a), performs the poorest, while heat treatment plus $CdCl_2$, (c), treatment gives the best results.

The CdTe substrates used in this sample were purchased from a commercial photovoltaic company whose name cannot be released. Also, since the substrate was purchased commerically, information about growth, chemical treatment, and material are all unknown. However, the advantage to a purchase of a large CdTe module for experiment is the uniformity of the sample such that numerous samples can be created with similar device performance. Though information about the fabrication process is unknown, certain aspects can be measured. In this thesis, the mean grain size was approximately 0.5-1.5 μm, while thickness of the CdTe p-layer was around 3-5 μm and the CdS n-layer 10-50 nm. Also, it is important that CdTe is a superstrate solar cell device, and since this thesis investigates the CdTe p-layer, light was injected into the p-layer, instead of through the n-layer as intended.

2.1.2 Absorption of Photons

The sun emits a spectrum of wavelengths that eventually become parallel rays of white light incident onto a solar panel. The solar spectrum is shown in Fig. 5. The red line Air Mass (AM) 0 corresponds to solar emission in vacuum (space). However when the sun enters the earth's atmosphere the light gets scattered, absorbed, and reflected. If sunlight is incident normal to the earth's atmosphere, there will be no scattered light (AM0). However, if the sunlight is incident at any other angle, the light will be scattered; this is known as AM1.5. AM1.5 Direct accounts for direct irradiance onto a normalized incident area on the earth's surface, whereas AM1.5 Global includes AM1.5D and diffuse reflection [15].

Each semiconductor material absorbs light in a different way; this is described experimentally by the penetration depth and absorption coefficient. It is also important to note that as the wavelength of light increases, the photon penetrates deeper into the substrate until the wavelength is such that it passes through the substrate as if it were transparent. Figure 6 shows penetration depth for various wavelengths. As the incident photon's wavelength increases, the absorption depth becomes larger. When it approaches the band gap, 860 nm, it passes right through the 4 μm thick CdTe solar cell shown [16]. It should be no

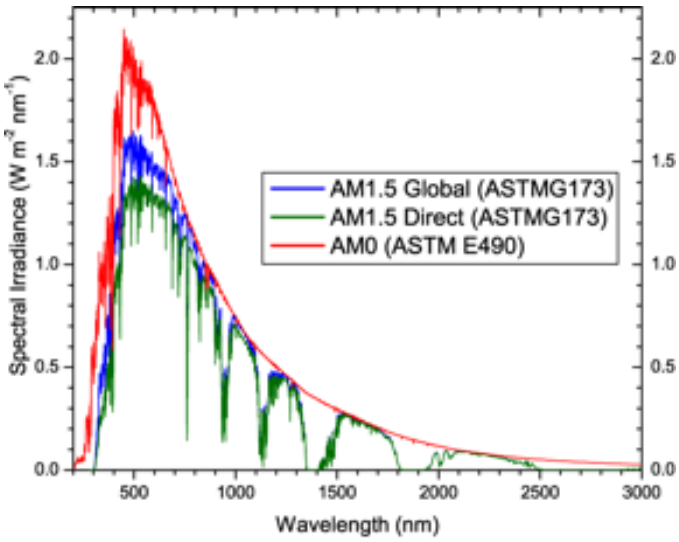

Figure 5: Solar spectral intensity as a function of wavelength. Air Mass (AM) 1.5 is the standard value to use for spectral intensity data. It accounts for the scattering effects of atmospheric molecules [15].

surprise that an optimum choice for p-layer thickness corresponds to the absorption depth of the band gap, 1.4-1.5 eV.

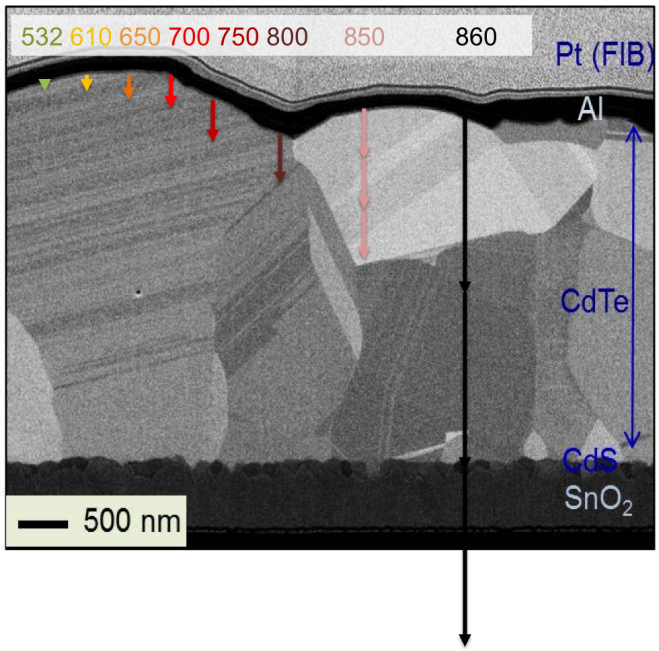

Figure 6: A "to scale" plot of penetration depth of several photons of different wavelength using a the scale bar present in the image.

Increasing solar cell absorption is a topic as closely studied as solar cells themselves. The most commonly found technology used on a solar cell is an anti-reflective coating. This coating is crafted to focus on absorbing a certain wavelength. Using thin-film diffraction physics, by choosing a certain material and thickness, this can be chosen easily. Another technique for increasing optical absorption is to texture the surface so that reflected light has more chances of entering the PV. Also the bottom of the absorbing layer can be textured to increase reflection back into the absorbing layer, instead of letting the light pass right through [6][17].

When light is absorbed into the material, the energy from the photon, if greater than the band gap, is used to excite an electron from the valence band to the conduction band. An electron-hole pair generated in a p-type material would produce a electron that would be called a minority carrier since the majority of carriers in the material are holes. The reverse is true in an n-type material. Once the carrier is generated, it must be collected. However, even in a perfect device the physics involved in collection are not wholly efficient [16].

2.1.3 Recombination

As previously mentioned, each wavelength of light has a corresponding energy to it. When a photon with energy above the band gap is absorbed by the semiconductor, there is a chance that an electron-hole pair will be created. Photon energies which are much higher than the band gap still have a chance of creating an electron-hole, but the electron quickly thermalizes back to the conduction band and the extra energy is wasted. Although an electron-hole pair has been created, there is an even smaller chance that the electron will be collected. This process which hinders the collection of electrons is called recombination. Recombination is defined as the return of an electron from the conduction band to the valence band with consequent disappearance of a hole.

The different types of recombination are defined by how they recombine and e-h pair. *Radiative* recombination is the process which makes a light emitting diode, a semiconductor

device, produce light. This occurs when an electron is excited across the band gap from the valence band to the conduction band. Any extra energy not used to help the electron cross the band gap will quickly thermalize so that the electron sits on the band edge in a meta-stable state. If the electron spontaneously recombines with a hole in the valence band, a photon with energy close to the band gap will be released. Since the energy of the photon is close to the band edge, it is weakly absorbed and does not contribute much to the collected photocurrent.

Another recombination event is called *Auger* recombination, and involves three carriers. An electron-hole pair is created, recombines, and the extra energy is given to third carrier. This third carrier now becomes a high-energy carrier that quickly thermalizes to the meta-stable state on the conduction band edge.

The last type of recombination is the interaction of electron-hole pairs with defects in the crystal lattice, defined as $Shockley-Read-Hall$ (SRH) recombination. Impurities or defects naturally or artificially occurring in a crystal lattice introduce energy levels within the band gap; these meta-stable equilibria are called defect levels or trap states. If an electron-hole pair is created, the electron/hole can move to a trap within the band gap, releasing energy as a photon or multiple phonons. If a hole/electron moves up to that same energy state before the trapped carrier can return to the conduction band, it will recombine [13].

Surface and bulk recombination dictate solar cell performance based on the rate at which generated minority carriers recombine, any free minority carrier can combine with any free majority carrier. The equilibrium state exists as dynamic equilibrium where e-h pairs are constantly being generated and recombined; but the average concentration stays constant. When light is incident upon the semiconductor, e-h pairs are generated and the equilibrium state no longer exists. The minority carriers are free for a certain period; this is called the minority carrier lifetime. This is a constant for each material and is determined as the time is takes for the minority carrier concentration to reach a value of 1/e; as long as the concentration is not too far from the equilibrium value. The carriers are not fixed

to the lattice but move around with an average velocity. The average distance in which a minority carrier travels before it is recombined is called the diffusion length [8]. Eliminating recombination centers will lengthen the lifetime of minority carriers, allowing for the carriers to freely travel a longer time and therefore distance.

2.1.4 Special Properties of Grain Boundaries

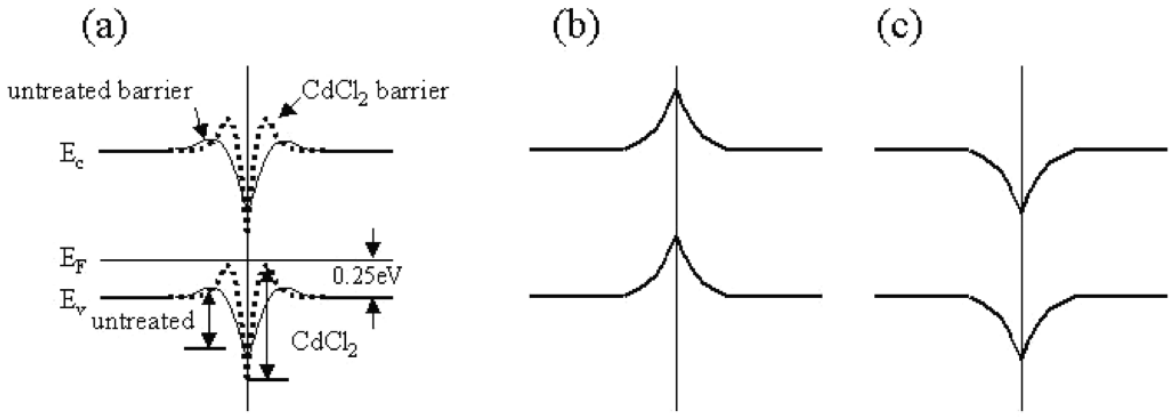

Figure 7: Models of grain boundary potentials from different experimental studies. a) Device CdTe, in-plane conductivity work by Woods et al. [18]. b) Device CdTe, injection dependent EBIC by Galloway et al. [19] c) Bulk CdTe, EBIC work by Durose et al. [20].

The largest contributor to efficiency losses in polycrystalline CdTe is grain boundary recombination. The first study which passivated grain boundary states, and increased quantum efficiency, of a CdTe solar cell was by Thorpe et al. [10]. This paper preceded the widespread use of the $CdCl_2$ treatment to boost device performance. After this discovery, a large effort in CdTe research has been focused on dissecting the effects of the $CdCl_2$ treatment. Even before Thorpe et al. it was known that CdTe imperfections introduced by grain misorientation create electronic states and significant band bending, however the addition of $CdCl_2$ treatment has resulted in research groups with different interpretations from each other.

More recent studies using EBIC, has inferred the form of the grain boundary potential in CdTe in layers stripped from commercial solar cells, using in-plane conductivity measure-

ments. The inferred band diagram is shown in Fig. 7a) [18]. Another EBIC study using planar injection deduced grain boundary potential by injecting large amounts of energy into the p-n junction and measuring spatial dependencies of the high injection threshold. This study indicates high carrier concentrations near the grain boundaries, with band diagram in Fig. 7b) [19]. Another EBIC method, measures the displacement current, as a function of probe position, flowing between two Ohmic contacts placed on either side of a grain boundary. This paper suggests a lower potential at the grain boundary as seen in Fig. 7c) [20]. Each paper shows a different physical understanding of the structure of grain boundary potential, however other experimental results have agreed upon one structure of band bending.

It is commonly agreed upon that these band states are spatially localized to the grain boundary. These trap states give rise to an accumulation of positively charged holes at the grain boundary, where holes are trapped in the lower potential state [21]. Though grain boundary passivation is known to increase device performance, contributions from either compositional or electronic effects have not been explicitly separated. It is important to dissect the inhomogeneities of the material to completely uncover the recombination sources on the interfaces of the grains.

2.2 Local Characterization of Solar Cells

2.2.1 Electron-Beam Induced Current

The most common use of an SEM is the detection of back-scattered and secondary electrons from an electron beam to produce an image. The contrast in the image depends upon the number of collected secondary electrons dislodged from the substrate by the electron beam. However, sometimes, this technique does not provide enough information to detect certain defects or failures within a device. Electron-beam induced current (EBIC), provides additional information by using an electron beam from an SEM and to induce a current in the device, which can then be mapped with the help of additional software.

This approach is especially useful for semiconductor defect and failure analysis. An

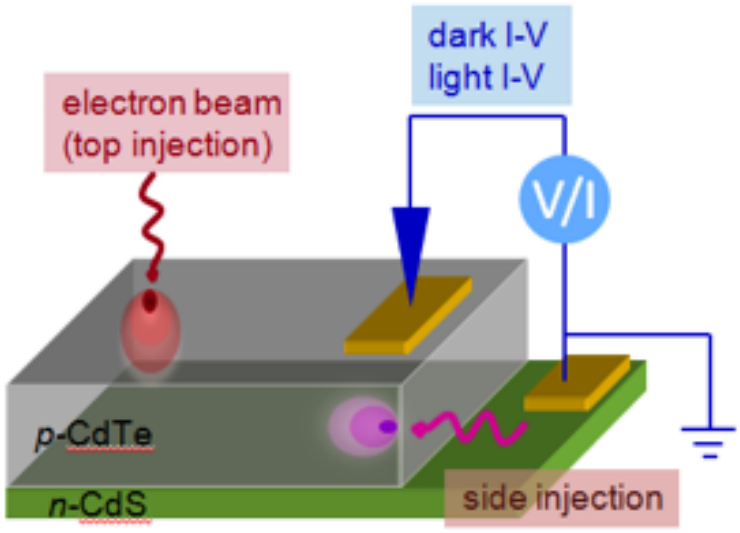

Figure 8: Schematic illustration of an electron-beam induced current (EBIC) measurement. Here, either top-view injection or side-view injection is possible, depending on the orientation of the sample. The bottom contact is CdS and the top is the CdTe. The incident electron beam of a specific acceleration voltage produces e-h pairs similar to how photons create e-h pairs.

electron beam is incident upon a semiconductor from either the p-side, n-side or normal to the p-n junction. Figure 8 shows a schematic representation of a semiconductor device used for EBIC, where an electron beam produces an interaction volume, resembling a "bulb" of accelerating voltage, where e-h pairs are formed and then later collected [22].

Typically EBIC is used for defect analysis, however one group studied nanoscale collection efficiency of a CdTe solar cell purchased from a commercial company [9]. They imaged p-layer CdTe on its cross-section and top-view showing photocurrent collection efficiency variations under a nanometer, as seen in Fig. 9. Also seen in this figure are collected current for different accelerating voltages. The higher the acceleration the voltage, the bigger the interaction volume or excitation bulb, and therefore, less resolution in the variations seen in the image. With a Monte Carlo simulation, this group saw that accelerating voltages of 5kV, 10kV, and 20 kV correspond to interaction volumes of 110 nm^3, 390 nm^3, and 1.3 um^3. Also, when a cross-section EBIC is performed, it is seen that there is an exponential decrease

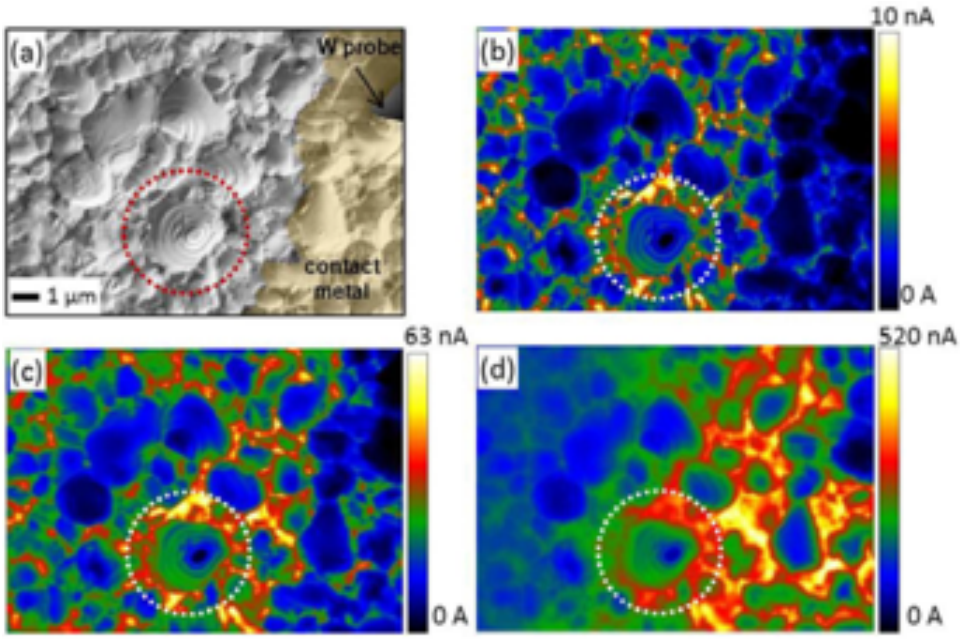

Figure 9: (a) Top-view SEM image of a small portion of the solar cell where a probe tip places on a metal contact (n-CdS is grounded). Corresponding EBIC images at the acceleration voltage of (b) 5 KV (c) 10 kV, and (d) 20 kV. Accelerating voltages correspond to interaction volumes of 110 nm^3, 390^3, and 1.3 um^3, respectively. Circle indicates a single grain [9].

in generated current as distance away from the p-n junction is increased, as intuition would expect.

Most of the results in figure 9 were expected, however there was one much more intriguing result that is not intuitive. Figure 9 shows relatively sharp variations in contrast of collected current between grain interiors and grain boundaries. This figure suggests that the grain boundaries are areas where collection efficiency is much higher, even though grain boundaries are intuitively thought of as recombination centers. Similar results are obtained for cross-section EBIC measurements performed at similar accelerating voltages. To rule out any topographical effects, a polished sample using a Focused Ion Beam mill was prepared, similar results were obtained. This paper attributes the EBIC enhancement to a large-built in electric field at grain boundaries, or a reduced recombination rate [9].

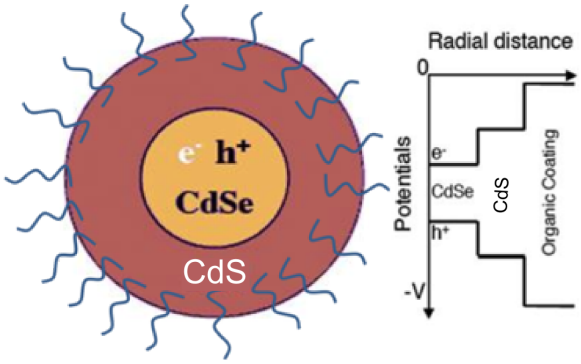

Figure 10: A CdSe/CdS core/shell quantum dot with corresponding quantum potentials (right). The blue lines denote an organic coating. If a quantum dot is given an energy greater than the core band gap, then an e-h hole pair is created. Unlike solar cells, it is favorable for radiative recombination to occur, this relaxation always occurs at the band gap energy. Therefore a photon of specific wavelength can be attained by choosing different core diameters (band gap energy) of quantum dots [23].

2.2.2 Quantum Dot - Electron Beam Induced Current (Q-EBIC)

This section introduces the idea behind a novel measurement technique developed in this thesis, quantum dot - electron beam induced current (Q-EBIC). Before this topic is introduced, a brief overview of quantum dots will be given.

A quantum dot or (q-dot) is a piece of matter with dimensions less than the quantum state it holds. For example, a q-dot with a size of 100 nm can emit a photon of 800 nm. It contains a quantum state with an wavelength (energy) larger than the dimensions of the nanoparticle itself. An example of a quantum dot is shown in Fig. 10; this specific image shows a core/shell quantum dot, with a quantum potentials plot shown for each layer. Quantum dots can similarly be created with two or three shells. Most quantum dots also have an organic coating, which can also alter the optical properties 12 [24].

Quantum dots are nanoscale semiconductors, so it is important to measure the absorption, conversion efficiency, and emission. Typically experiments performed to obtain a measure of how well the quantum dot emits photons are photoluminescence and optical absorption experiments. Photoluminescence is the optical radiation emitted by a physical system (in excess to black-body radiation) resulting from excitation to a nonequilibrium

state by irradiation with light. A similar type of measurement technique like photoluminescence is cathodoluminescence, where an electron beam is used to excite the quantum dot and the subsequent emission is measured. Absorption can simply be measured using a spectrophotometer, which is widely used to measure transmission/reflection/absorption through a colloidal sample [24].

Quantum dots have many different applications, such as the biomedical field where they are used as detection mechanisms in molecular and cell biology. They are also used in PV applications in an effort to increase solar cell performance [26]. In this thesis, yet another use for q-dots is explored. Figure 12 is a schematic representation of a device prepared for Q-EBIC measurement. Like EBIC, Q-EBIC uses an same e-beam to excite q-dots, supplying them with enough energy to fluoresce at the emission wavelength. The emitted photons radiate outward spherically from the recombination center in which they spawned.

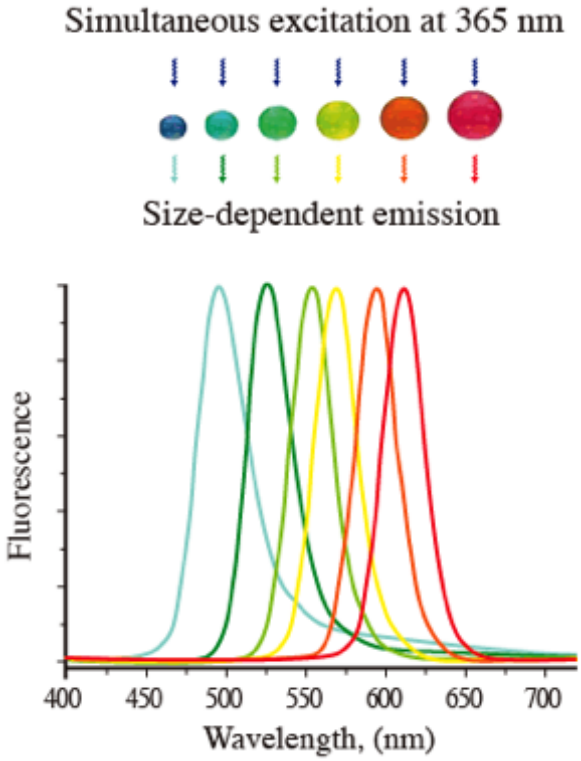

Figure 11: The emission wavelength of a quantum dot is dependent upon its size. A typical schematic representation of emission wavelength shows blue fluorescence is emitted from the smallest particles, while red and IR come from the largest in diameter [25].

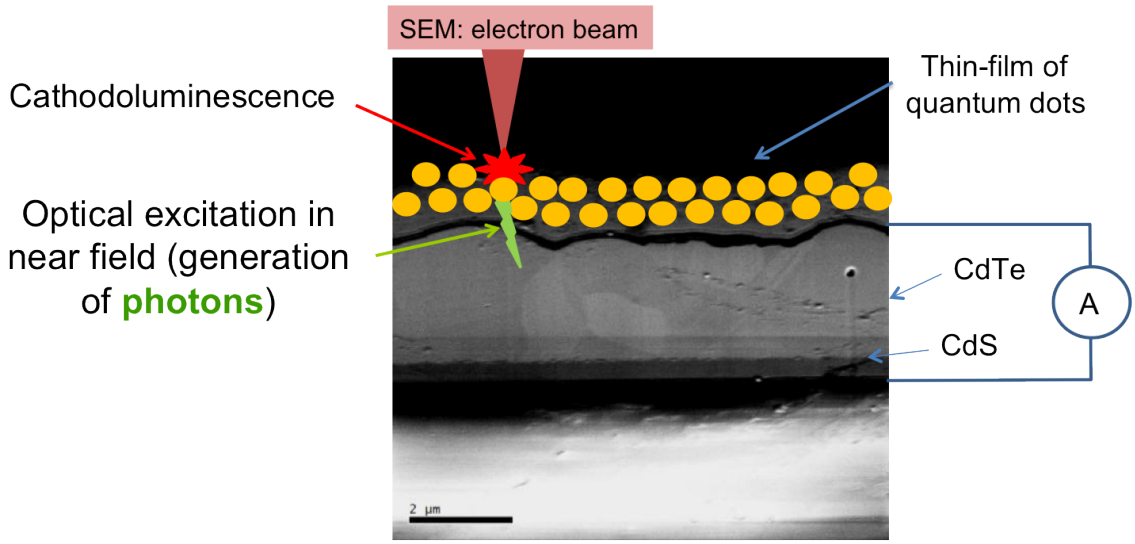

Figure 12: A schematic representation of how Q-EBIC works. Electron beam excites a quantum dot, that quantum dots then emits a photon at the emission wavelength, and the photon gets absorbed by the solar cell to generate an e-h pair and eventually photocurrent.

The photons can either be absorbed by the semiconductor, other q-dots, or lost completely. Since the photons are generated extremely close to the surface of the semiconductor, the emitted photons can be considered as near-field radiation.

2.2.3 Light-Beam Induced Current (LBIC)

To advance the technology of semiconductors, it is imperative that the fundamental losses of efficiency are understood. Light-beam induced current (LBIC) is useful because it allows for a small laser spot size to examine specific areas of a solar cell to detect variations in conversion efficiency. The spot size, however, is limited to a diameter as small as 1 μm, larger than most grains in a CdTe cell. For laser spot sizes larger than one micron, this technique is more useful to study failure of an entire module, not micro- or nanoscale defects. Research using LBIC to examine microscale effects of surface treatment on CdTe solar cells has resulted in unexpected results [27].

The most interesting results are shown in Fig. 14 and 15. Under an illumination intensity of one Sun and a spot size of 1 μm, a CdTe solar cell passivated with a cadmium

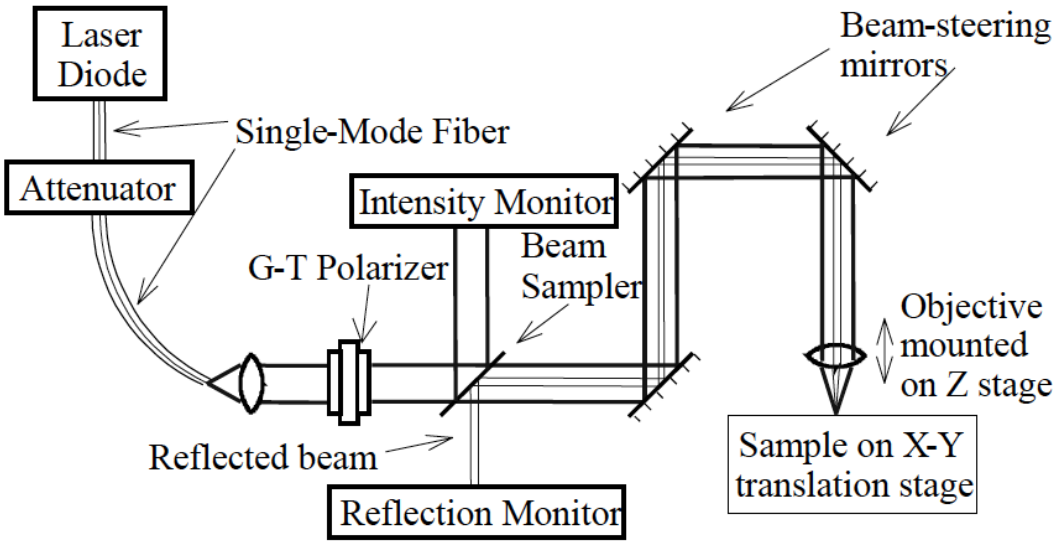

Figure 13: The typical setup of an LBIC experiment, where a laser of arbitrary wavelength is coupled to an optical fiber, attenuated and is incident on a semiconductor surface [27].

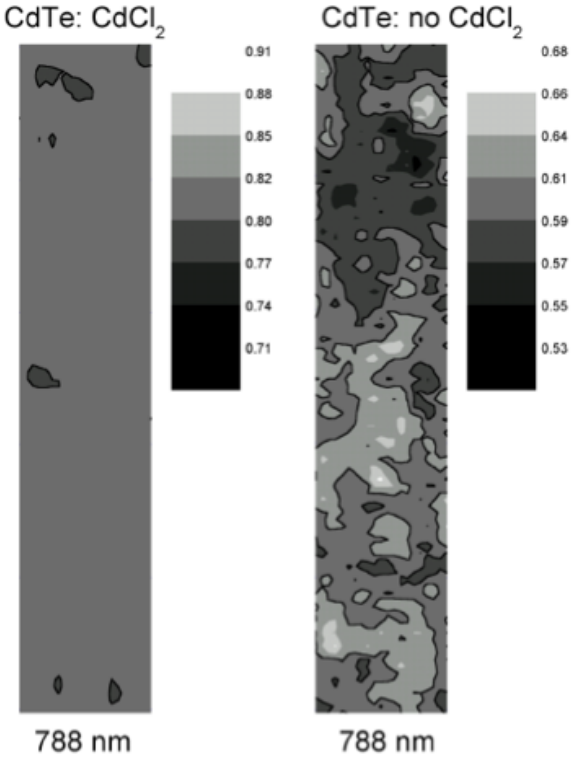

Figure 14: LBIC measurement on treated CdTe and non-treated CdTe solar cell. 50x10 um area^2 with 1 micron spot size and intensity of 1 sun. Results show more variation for below bandgap energy when no treatment is performed. The scale bar corresponds to external quantum efficiency of the [27].

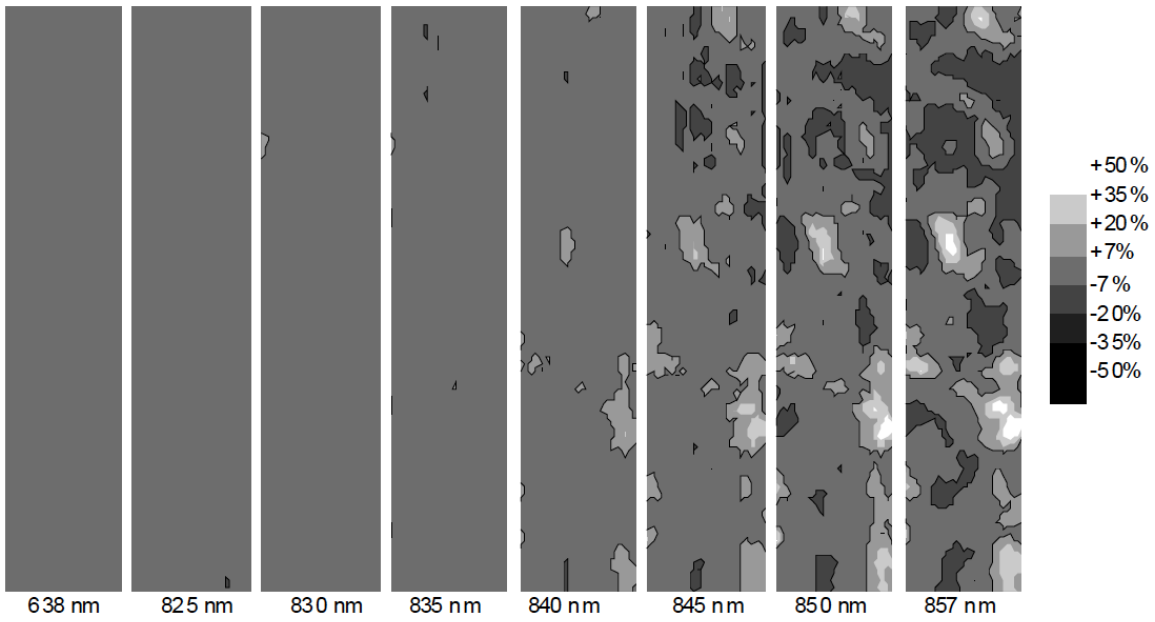

Figure 15: Response over a 50x10 um area on a $CdCl_2$ treated cell with multiple wavelengths as labeled. The contrast in each case is consistent with the variation from the mean value. This data set is taken with a probe size of 1 micron and intensity of one sun [27].

chloride ($CdCl_2$) treatment is examined using LBIC. This experimental setup allowed multiple wavelengths to be incident on the same area. Figure 14 shows external quantum efficiency variations versus position. The CdTe cell not treated with $CdCl_2$ shows the largest variation for above bandgap photon energies. However, when photon energies slightly below the CdTe band gap are used, variations in response are largest for the $CdCl_2$-treated cell. A standardized practice for producing CdTe solar cells is to passivate the surface with a $CdCl_2$ treatment. This paper shows that when this is done, there is much larger and more uniform photocurrent collection.

Also performed, was a multiple wavelength LBIC measurement on the same area. Figure 15 shows variations from the mean current value, white means higher current and lower current values are shown as black. As the wavelength is increased to the CdTe bandgap, more variation is present. This paper suggests that variations in collection efficiency are due to the $CdCl_2$ treatment creating a $CdTe_{1-x}S_x$ alloy changing the absorption of photons with energy below the pure-CdTe bandgap. The cell which was not treated with $CdCl_2$

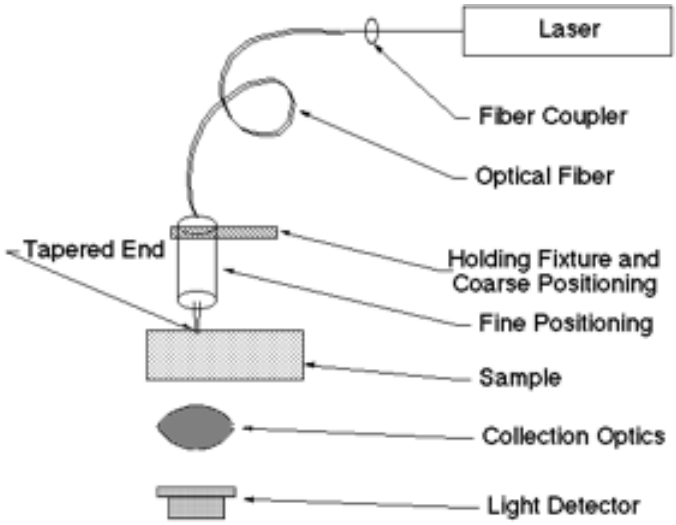

Figure 16: A typical setup of an NSOM. First a laser emitting photons of some wavelength is coupled into an optical fiber. This optical fiber is special in the sense that it is eventually tapered down to nanometer size. This tapered end is usually covered in a metal cladding which controls the size of the aperture of which the photons exit. This tapered end of the fiber is attached to a tuning fork, where the NSOM is lowered to the surface using the AFM feedback loop. The transmitted light is then collected by a photodetector and measured [28].

does not show this behavior, strongly suggesting that variations in band gap are due to the treatment. This thesis also suggests that $CdCl_2$ penetrates non-uniformly to the CdS/CdTe surface, creating unpredictable local increases in photocurrent [27].

2.2.4 Near-Field Scanning Microscopy (NSOM)

The resolution of many focused light microscopy techniques is limited by the wavelength of the radiation. NSOM allows for a nondestructive imaging method independent of the wavelength of radiation. Compared to the limitations of other high resolution scanning probe microscopy techniques, NSOM holds a competitive edge. For example, an SEM requires a highly conductive surface to produce images, whereas NSOM requires only that the sample be transparent enough to detect far-field photons. In certain applications, it is definitely more advantageous to use an NSOM over an SEM [29]

A NSOM does not require modification to the surface of a sample, as long as it is transparent, allowing for high resolution imaging of samples in their native environment. Not

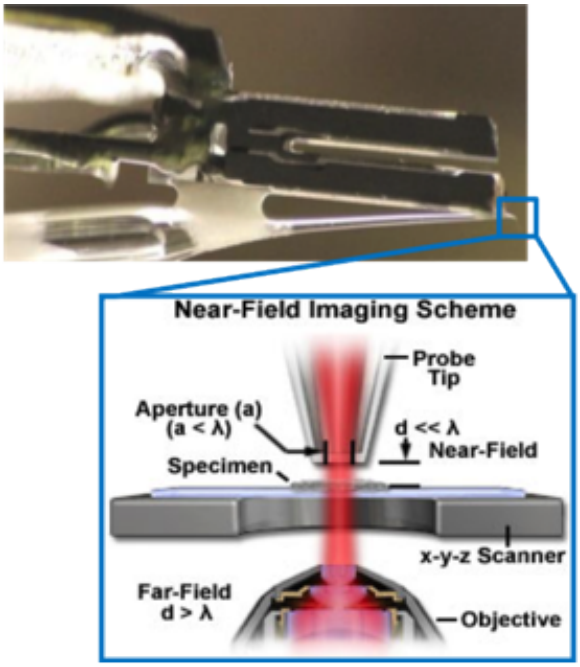

Figure 17: An image of a AFM tuning fork with tapered optical fiber attached. Here it can be seen that the tapered fiber is glued to the bottom of the tuning fork. The image fails to capture the tip of the tapered fiber because the dimensions of it are under 500 nm. The blue frame denotes a zoomed in cartoon of the area of interest. In this cartoon it is shown that the aperture is less than the wavelength of radiation, the distance from the sample is much less than the emission wavelength and the collection is in the far field [30].

only will this technique provide high resolution, but due to its non-damaging property, it will be able to follow the temporal evolution of macromolecular assemblies in living cells [29]. Though this thesis does not use NSOM for its intended use, the far-field collection of near-field scattered photons, it is important to understand how a typical NSOM works in order to appreciate it's use for nanoscale characterization of non-transparent inorganic solar cells.

A typical NSOM set-up is shown schematically in Fig. 16. Photons are initially emitted from a laser source or arbitrary wavelength, however some wavelengths may not be compatible with certain optical fibers and if too much power is delivered through the fiber; it can melt or burn. With the use of a multi-mode fiber, different wavelengths can be coupled through the same probe. The optical fiber is eventually tapered down to a much smaller

diameter, around a few microns, and has a metal cladding around it for structural support. The part with metal cladding can be seen in Fig. 17, which is glued to an AFM tuning fork; the cladding also covers the end of the tapered fiber where the photons exit. The NSOM is especially useful here because it allows a simultaneous action of performing a measurement of topography and shining a laser over the same spot. The feedback loop of the atomic force microscope (AFM) allows the emitted light from the probe aperture to remain in the near-field. In the case of an NSOM measurement, the near-field light would be diffracted by the transparent substrate and eventually collected in the far-field by a photodetector. The measurement of transmitted light in the far-field provides additional information of the substrate because the resulting pattern no longer resembles the diffraction pattern of the aperture [29].

The measurements performed in this thesis do not focus on high resolution measurements by way of collecting near-field diffraction patterns in the far-field through a transparent substrate. We simply use the AFM feedback and the tapered fiber simultaneously to obtain information about topography while shining a laser on the sample. In the case of a semiconductor, this is very similar to an LBIC measurement, however we obtain topography while also using a smaller laser spot size. An LBIC approach is limited by geometric optics, whereas an NSOM can go beyond this limit. Two groups have published notable works in the field of NSOM measurements on a CdTe solar cell substrate, the results will be summarized below [21],[31].

The first group performed near-field imaging on the surface of a p-type zinc telluride (ZnTe) back-contacted CdTe solar cell. The spot size of the NSOM tip was 100 nm in diameter. A 635 nm laser, measured to have an output of approximately 1 nW coming out of the NSOM fiber to the semiconductor surface, was used in this experiment to locally generate photocurrent in the near-field. Though there is an optically thin layer, 50 nm, of ZnTe, aside from small defects, the AFM topography scans should still largely reflect the same grains and grain boundaries as seen in a typical polycrystalline CdTe solar cell.

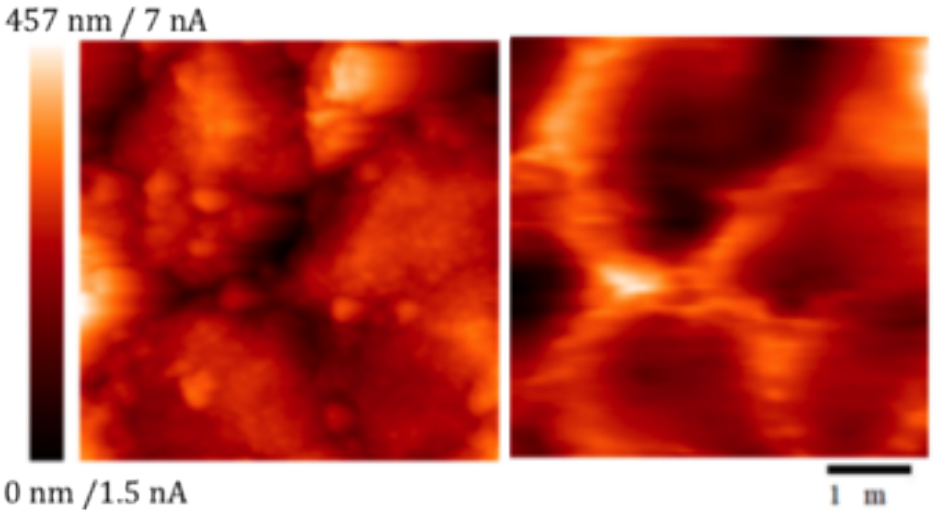

Figure 18: Left) AFM image of polycrystalline CdTe/CdTe/ZnTe:Cu solar cell. Right) NSOM image showing collection of photocurrent in the same region. The small artifacts are likely to be non-uniformities presented from the ZnTe optically thin, 50 nm, layer [21].

Figure 18 indeed shows this. This figure also shows small defects, or finer grain structures, present in the topography scan, this is most likely to be the ZnTe. The 5x5 μm scan shown in Fig. 18 shows a simultaneously obtained photocurrent signal in nano-Amperes. The grain boundaries have up to five times larger collected photocurrent in contrast to the grain interior. The success of the grain boundaries relatively high collection efficiency is attributed to bending of the energy band structure at the grain boundaries. This bending effect is due to the chlorine ions introduced to the CdTe solar cell during a $CdCl_2$ surface treatment. Specifically, these ions at the grain boundary introduce a local electric field and drive away holes, thus facilitating charge separation and decreasing the probability of both recombination and hole-trapping near the grain boundary [21].

The other group performed an investigation of sulfur diffusion between the CdTe p-layer and the CdS n-layer. This task was completed by performing NSOM measurements on a cross-section sample of CdTe, as seen in Fig. 19 (a), at multiple wavelengths around the band egde. This study cites the specific use of a tunable Ti:sapphire laser and a 632.8 nm HeNe laser which were simultaneously coupled into the fiber probe. The HeNe laser provided

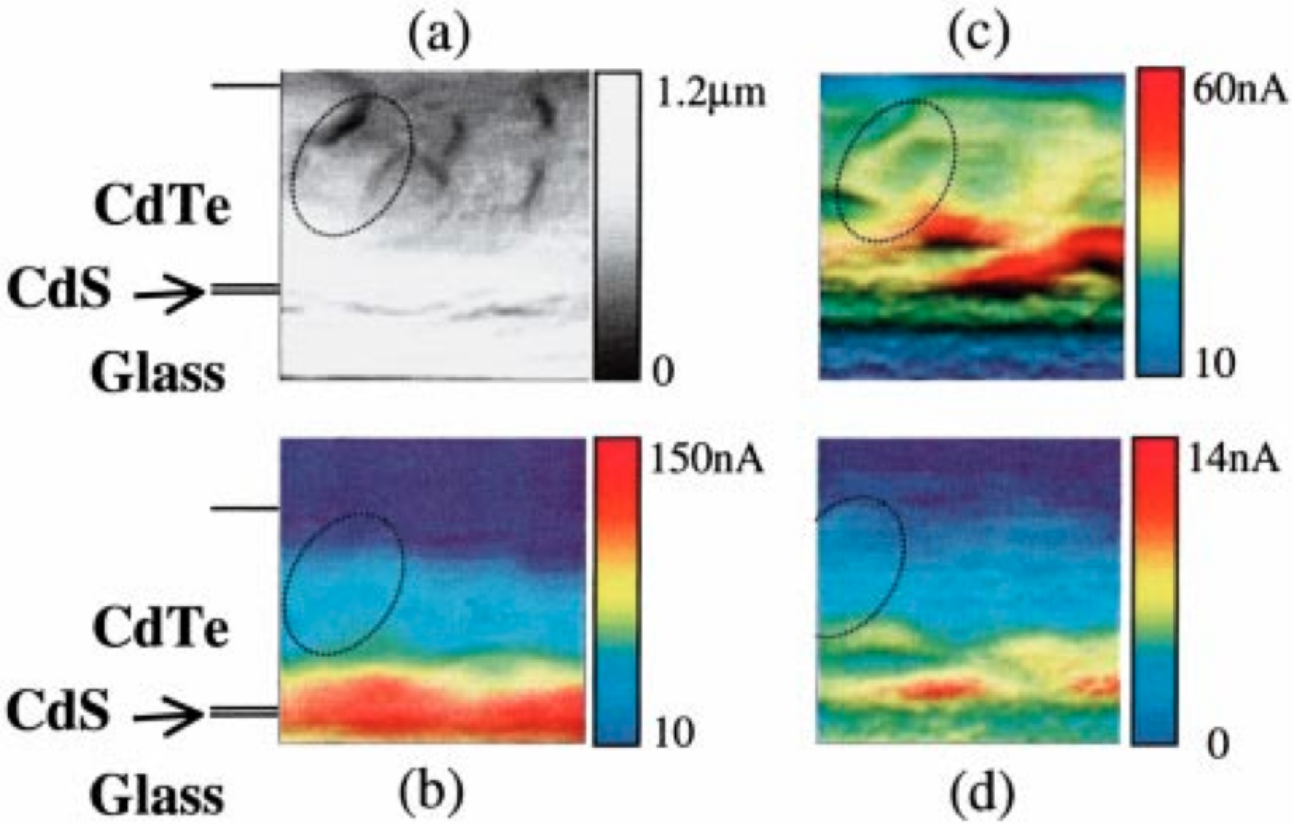

Figure 19: (Color) 4.8 micron topography (a) and photocurrent (b)-(d) NSOM measurements taken on the cross-section of a CdTe/CdS solar cell. The location of one particular grain has been outlined in each image. The shift in its position is due to drift which was tracked using the topographic images. (b) Excitation energy is 1.615 eV, above band gap. (c) Excitation energy is 1.463 eV, 50 meV below CdTe band gap. Increased width of the collection region in the CdTe layer is observed compared to (b). For the marked grain, the collection is much greater at the boundary than in the interior. (d) Excitation energy is 1.422 eV [31].

a control to compare each measurement to ensure uniformity in probe and scan conditions. The scans of the cross-section started at the p-n junction and slowly moved to the back contact on top of the p-layer CdTe. Figure 19 shows topography scans of the p-n junction along with three different excitation wavelengths. When the probe is located on the CdS n-layer, there is a high chance that the laser will shine through the glass front face, as it would under normal operation. This causes a large amount of noise in the signal located at the p-n junction. In spite of this, a large amount of contrast was observed for excitation energies below the band gap. The contrast in the images is attributed to a spatial variation in the band gap due to variations in sulfur content presented by annealing the solar cell during fabrication [31].

2.3 Summary

Nanoscale characterization with sub-grain resolution is extremely important for understanding the physics behind efficiency losses in polycrystalline semiconductor materials, specifically CdTe. Some groups have performed LBIC experiments with sub-grain resolution using an NSOM, however the results of such measurements are in common agreement. While it is known that the grain boundaries in polycrystalline CdTe induce band, or trap, states that allow for spatially localized area of relatively dense hole concentration. Though we have documentation of how the grain boundaries change this specific material property, there is still not a consensus as to why these trap states produce enhanced photocurrent collection.

Two techniques are presented in this thesis to test for their viability in being used for nanoscale characterization of photocurrent collection efficiency. In the Q-EBIC experiments, more effort was focused in testing the technique as a viable photon induced current measurement. The other measurement technique tested in this thesis, NSOM, is not as novel as Q-EBIC, however it is still important to test and confirm this techniques ability for high-resolution and versatility. Both techniques are similar in the sense that they can be used to

locally excite e-h pairs and discern between grain interior and grain boundary photocurrent collection.

The goal of this thesis is to present a methodology that is reproducible, it is also important to clearly present data obtained so that a transparent analysis can be followed in the next few sections. This will include analysis of preliminary results with an explanation for areas for further experimentation. The preliminary results will motivate further experiments for separating electrical and chemical effects of enhanced grain boundary photocurrent collection relative to grain interior. This can be done with different techniques which all offer their own advantages. Much can be learned by performing similar measurements with different apparatuses.

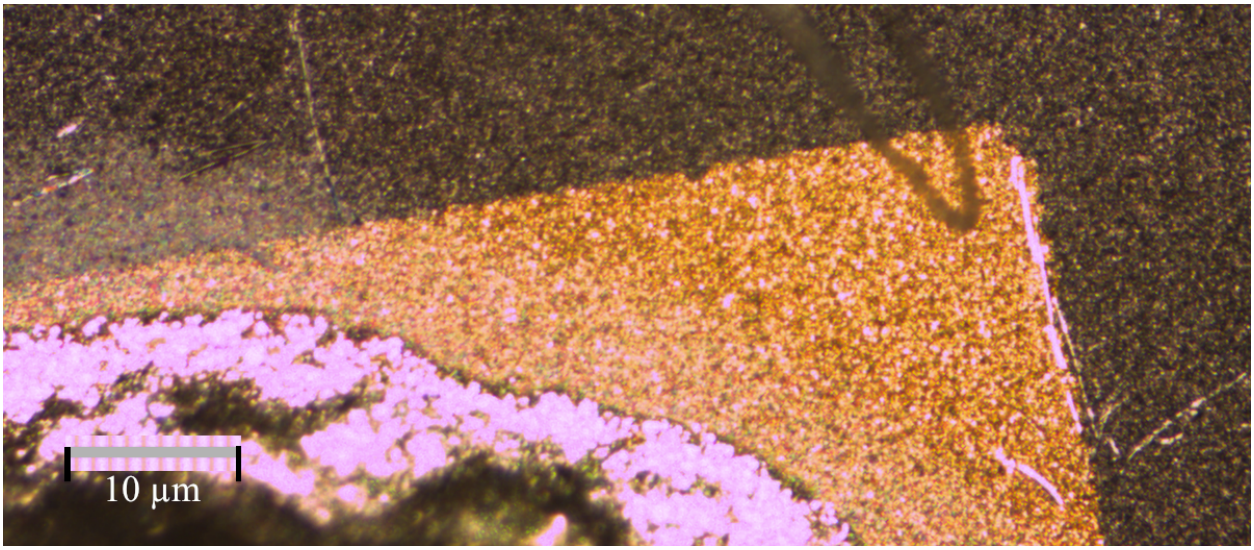

Figure 20: The portion of the device shown here is the top contact of a CdTe/CdS p-n diode. Where the out-of-focus silver part is conductive epoxy, the gold part is e-beam deposited Au, and the gray portion is CdTe. This is a device that can be used for high-resolution, low-noise measurements.

3 Methodology and Results

This section presents the necessary information for reproduction of the experiments performed in this thesis. The information provided in the previous chapter was to assist in developing an understanding for the methodology described below. Every experiment performed in this thesis involves creating a small device, for low-noise, high resolution measurements, from a commercial solar cell. As well as exciting e-h pairs with photons and collecting the amplified signal. First, since both of the experiments, NSOM and Q-EBIC, involve similar device fabrication methods, this will be explained in context for both chapters with further details explained at the beginning of the respective chapters.

3.1 Basic Sample Fabrication

Without careful fabrication of devices, fruitful data acquisition would not be possible. Figure 20 shows an image of a device fabricated for use in experiment. Not shown in the figure is the bottom contact, a CdS n-layer which can be seen in Figure 1. Figure 20 was

taken under a x10 objective microscope lens. Shown in the image is the top contact, a p-layer, on CdTe. Bromine etching was used to strip away all of the CdTe layer leaving behind the CdS (window layer) n-layer. Since the bromine did not strip away the window layer, it remained in the bromine-methanol solution until all of the CdTe was visibly removed from the surface. Scanning electron micrograph images, as seen in Figure 1, show only CdS remains. With both p- and n-layer exposed, an e-beam evaporator can be used to deposit contacts on p-layer CdTe. On the devices used, an approximately 1 mm x 1 mm Au contact was placed on the p-layer CdTe.

To ensure the device performance is preserved through the fabrication process, it is important to perform light and dark j-V curves of devices at each step of creating the device. If the device still performs reasonably well, e.g. not short-circuited or extremely ohmic, then the device can still be used for experiment. Though the physics involved in producing photocurrent from the samples are almost identical, the different experiments require separate machinery.

3.2 Q-EBIC

3.2.1 Q-EBIC: Methodology

Physical parameters of the q-dots were tested. Figure 21 shows a fluorescence spectrum and PL spectrum of the q-dots used in this thesis. Both of the figures show an intense peak around 620 nm with a full-width half-maximum value of the peak of $\approx$ 20 nm. The next examination of physical parameters was q-dot size. Figure 22 shows a histogram of the measured diameter of 174 q-dots imaged with transmission electron microscopy. The q-dots have an average diameter of (8.8 $\pm$ 1.2) nm.

A Q-EBIC measurement requires a uniform layer of colloidal q-dots on the surface of the CdTe device. The dip coater used in this experiment was a TL0.01 Desktop Dip Coater from MTI Corporation. The dip coater retracted all samples from the colloidal q-dot solution at approximately 1 mm/s. Simply dipping the CdTe substrate into the colloidal q-dot solution

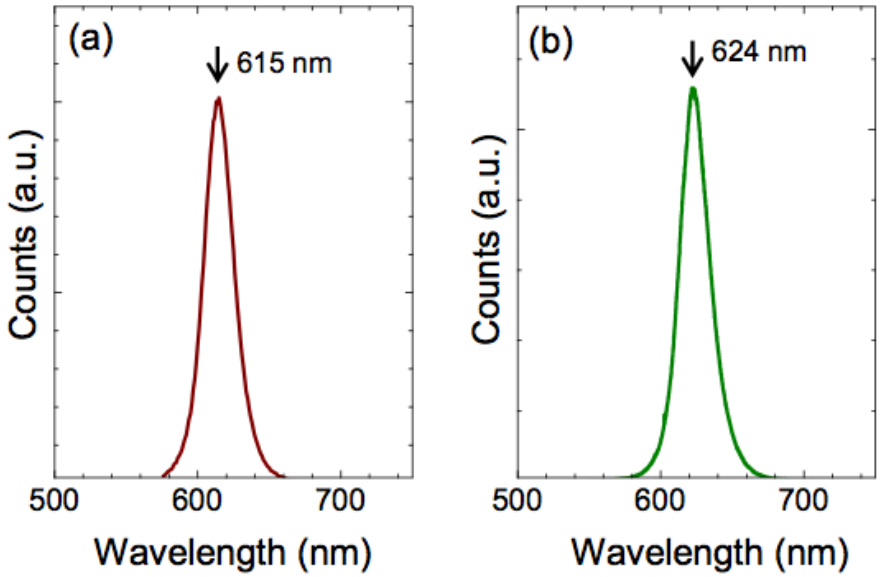

Figure 21: (a) Fluorescence spectrum of the colloidal q-dots used in this work showed an intense peak at ≈ 615 nm. (b) A drop of the colloidal q-dot solution was deposited on a glass substrate and dried for photoluminescence spectroscopy. Full-width half-maximum of the peak is ≈20 nm for both cases.

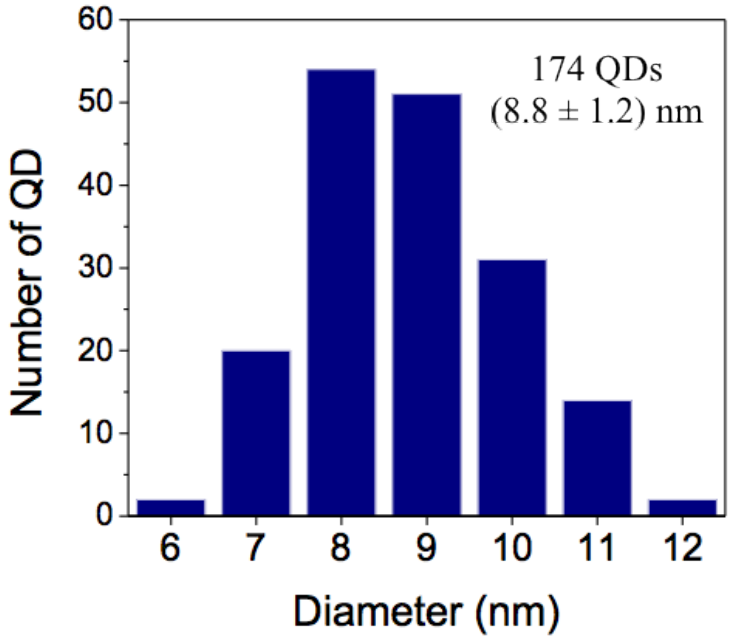

Figure 22: The average diameter of the q-dots was (8.8 ± 1.2) nm based on analyzing 174 q-dots using transmission electron microscopy.

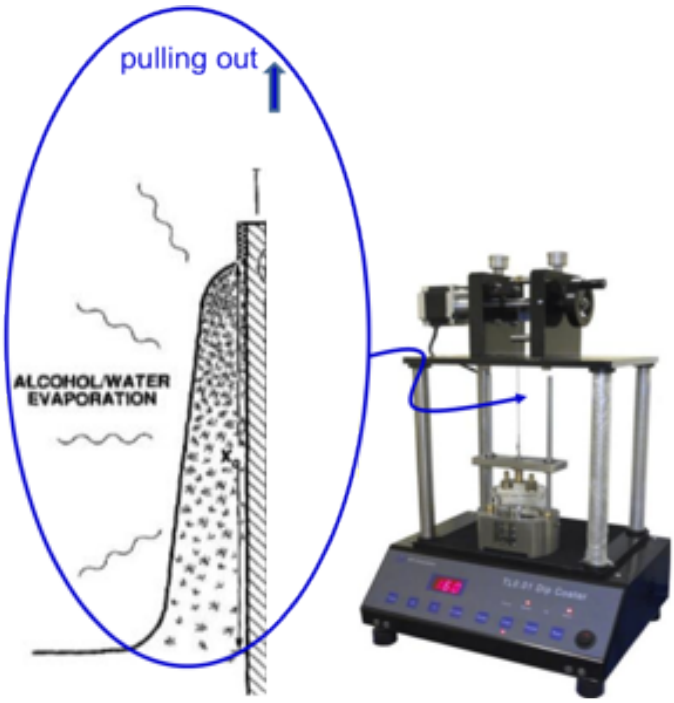

Figure 23: Left) A schematic of the sol-gel technqiue for coating substrates [32]. Right) The dip-coater used in this experiment [33].

was not enough to ensure a uniform thin ($\approx$ monolayer) layer of q-dots, as will be explained in Chapter 3.2.2. The interaction of q-dot with CdTe substrate required modification of surface chemistry.

It was much simpler to attach the q-dots onto an Au substrate, where the gold would serve as a contact to collect photocurrent as well as a substrate for modified surface chemistry. The Cu/Au contact (2nm/7nm thick) contact was deposited using an e-beam evaporator. Figure 24 shows the transmission spectrum of a thin metal film of Cu/Au on a glass slide, where $\approx$ 65% of of the visible light around 620 nm is transmitted. With transmission through the Cu/Au contact confirmed, the experiment could proceed.

To assist in q-dot self-assembly, the sample was dipped into 0.1 M of 1,3 propanedithiol (PDT) in acetonitrile and was pulled out. After the dip, the sample was rinsed with acetonitrile to wash away unbound thiol. The substrate was then dipped into the colloidal q-dot solution and pulled out, quickly drying in air. A subsequent dip in toluene rinsed away the

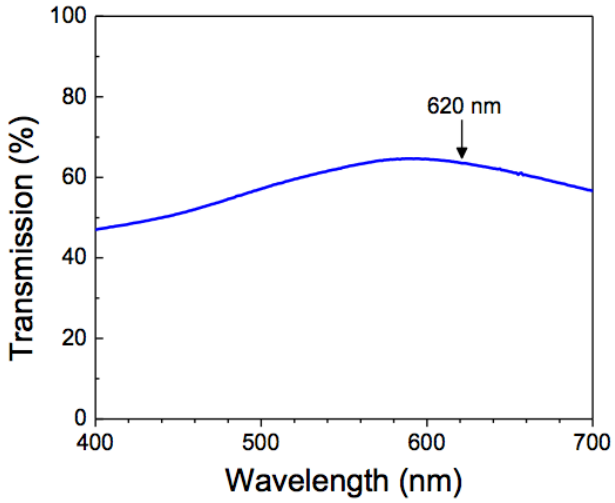

Figure 24: A representative transmittance spectrum of a thin metal film (Cu/Au = 2nm / 7nm) deposited on a glass slide. The transmittance at 620 nm (arrow) is 65 ± 5 %.

unbound q-dots. This process was repeated three times, to ensure a uniform coating on the Au contact. The thickness of the q-dot layer, after three dips, was ≈ 50 nm. Using the average size of q-dots, 8.8 nm, this results in ≈ 6 q-dot layers.

For the cross-sectional Q-EBIC measurement, another procedure had to be followed or else the p-n junction would be short-circuited by a Cu/Au gold contact. The CdTe was placed in a focused-ion beam (FIB) for milling to create a flat surface for Q-EBIC imaging. The CdTe sample was then submerged in 2 mM of hexadecanethiol in ethanol solution for 8 hours, allowing the colloidal q-dot solution to coagulate more, hydrophobic-like, instead of rapidly spread out, hydrophilic-like. The sample was then rinsed in ethanol and blow-dried with a N_2 gun. The sample was mounted onto the dip coater and pulled out with the same conditions as above.

The physical measurement setup is seen in Fig. 12 on Pg. 19, where the top and bottom contact are connected through a preamplifier. Not shown in the figure is a nano-manipulator inside the SEM with a tungsten probe (100 nm tip radius) placed on top of the contact to p-CdTe. The electron beam from the SEM induces emission photons from the q-dots, which

simultaneously induces photocurrent as well as pass through a detector for cathodoluminescence. As acceleration voltage of the e-beam is increased, the penetration volume also increases. The cathodoluminescence detector discerns between emission signal generated from q-dots or CdTe substrate. After this test is performed, the data acquisition for Q-EBIC generated photocurrent can begin. A more detailed description of this test is explained in Fig. 25, which will be interpreted in the next section.

3.2.2 Q-EBIC: Results and Discussion

Once a uniform layer of q-dots are self-assembled on the surface, a Q-EBIC measurement can be performed. As mentioned previously, it is important to perform a cathodoluminescence (CL) measurement, as seen in Fig. 25. A cathodoluminescence measurement was performed for different accelerating voltages. The larger the acceleration voltage, the larger the excitation bulb. Figure 25 shows Q-EBIC image with the adjacent image being the corresponding CL spectrum. The q-dots' emission wavelength is roughly 620 nm, and the CdTe has an emission wavelength of $\approx$ 810 nm, corresponding to a band gap of $E_g = 1.5$ eV. Figure 25 indeed shows that q-dots induce a measurable amount current in the solar cell.

Figure 25 (b) shows, however, that if an insufficient amount of accelerating voltage is incident on the q-dot layers, photons generated on the surface of the q-dot layer, may not reach the solar cell. This image shows dark spots, zero collected current, at certain grain boundaries. This means that in the specific area, the grain boundary valley is exceptionally steep and full of quantum dots. There are so many q-dot layers in this valley, that the q-dots absorb the emitted photons. Clearly, Fig. 25 (c) shows fewer dark spots, and Fig. 25 (d) shows no dark spots when the CdTe surface and q-dots emission are equally collected by the CL detector.

To eliminate topological effects such as grain boundary trenches, another measurement on p-CdTe can be performed. By using a focused ion beam (FIB), a cross-sectional sample be made that has less variation than an unmodified CdTe surface. Variations in this surface

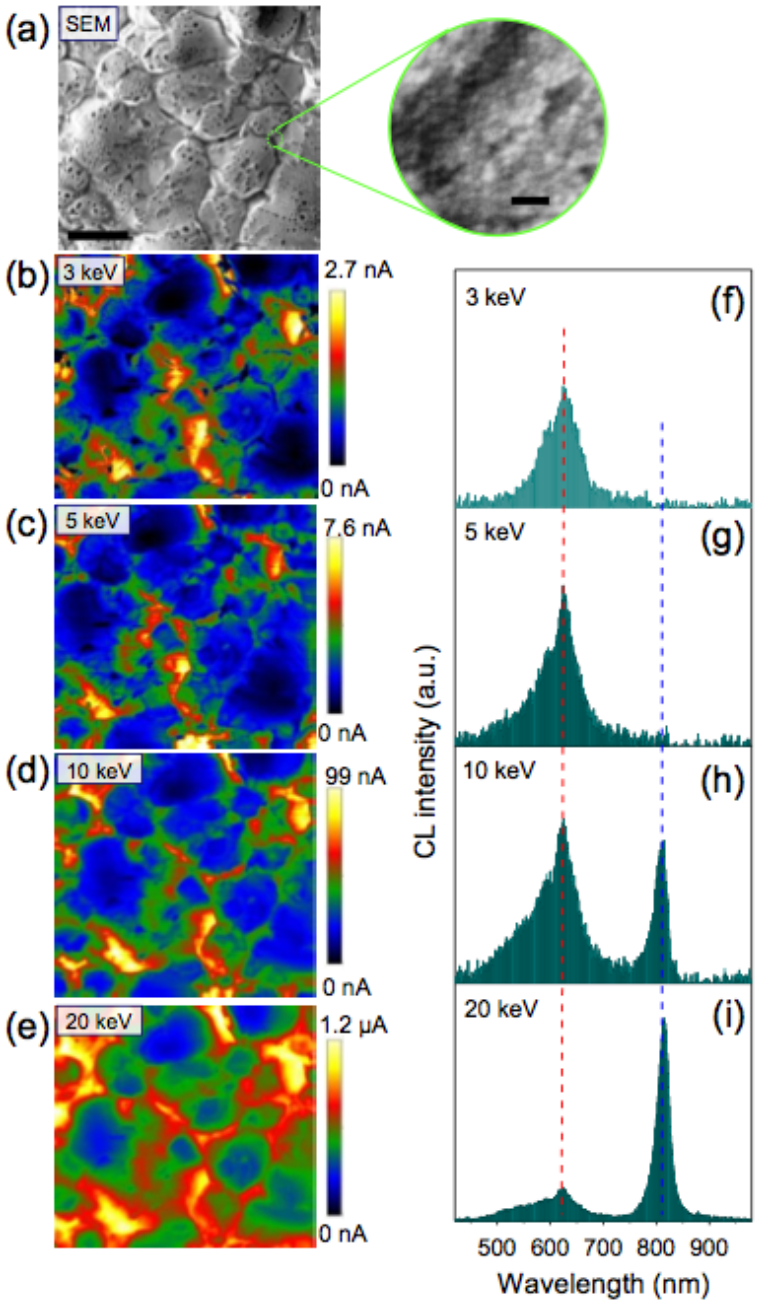

Figure 25: SEM image of a q-dot layer assembled on a p-CdTe / n-CdS solar cell. Inset shows the high magnification of the conformal assembly of the q-dot (scale bar 50 nm). Q-EBIC images (b-e) and the coresponding CL spectra (f-i) as a function of electron beam voltage (3 keV, 5 keV, 10 keV, and 20 keV), respectively. The bright contrast seen at many grain boundaries indicates higher excess carrier collection as compared to grain interiors. The prominent peaks at 620 nm (red line) and 810 nm (blue line) arise from band-to-band radiative recombination in the q-dot (E_g = 2 eV) and the CdTe absorber (E_g = 1.5 eV).

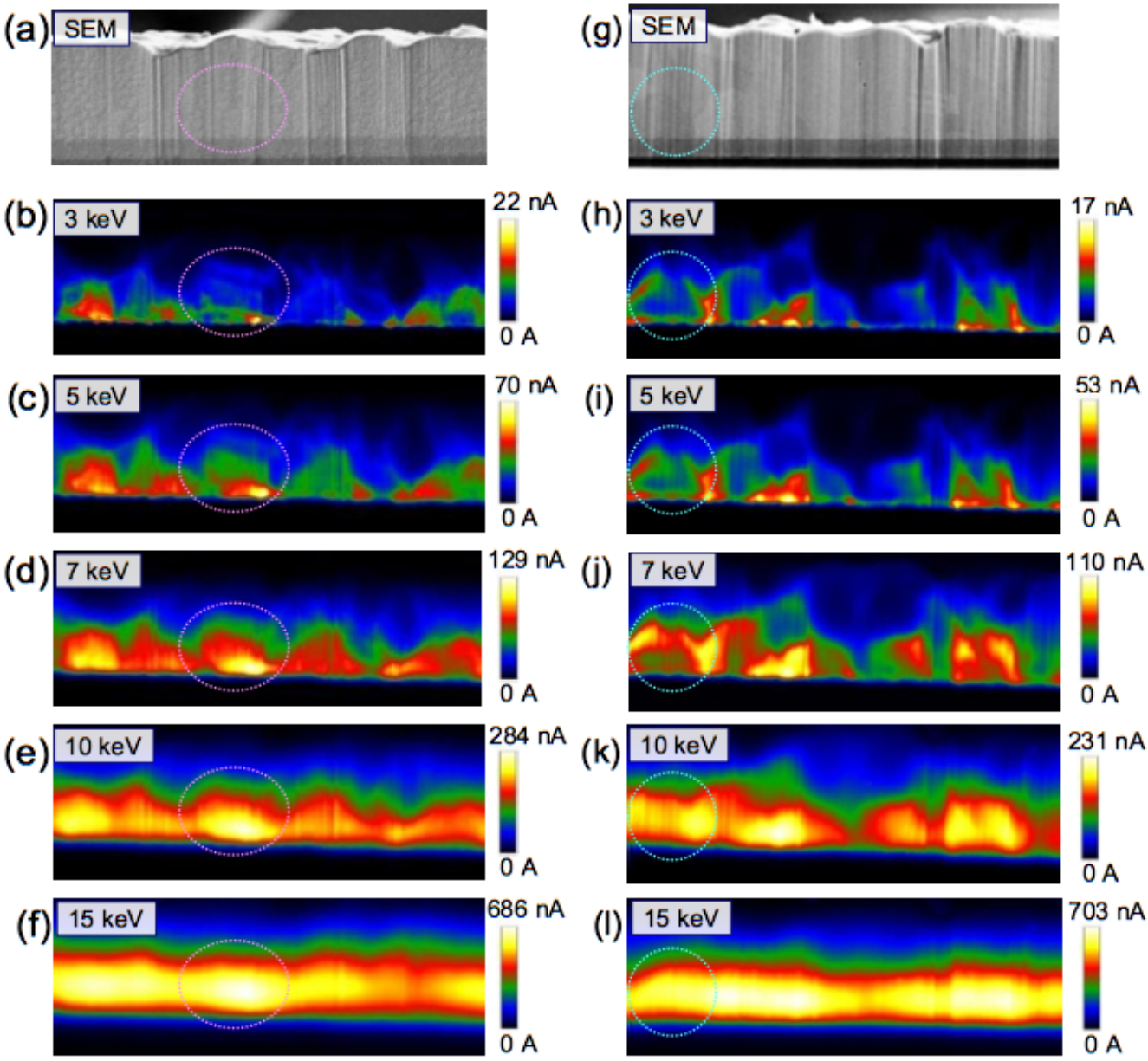

Figure 26: Cross-sectional SEM images of n-CdS / p-CdTe solar cell with (a) and without (b) an assembly of q-dots. A series of corresponding Q-EBIC (b-f) and EBIC (h-l) images at different electron beam voltages. The top value of each scale bar represents an average of the 50 highest pixel current in the 1024 x 1024 current map (electron beam step size ≈ 16nm). The circle in the images identifies a single grain in the CdTe absorber.

are a product of FIB milling and are only on the order of ≈ 70 nm, much flatter than a typical CdTe surface. The technique for obtaining data is similar to the last, however, the sample now is rotated so that the p-n junction is normal to the electron beam.

Figure 26 shows an SEM image of a milled cross-section of CdTe with q-dots (a) and without q-dots (b). The q-dot layer seen in Fig. 26 (a) has an ≈ 50 nm thickness. Images (b-f) show Q-EBIC images corresponding to EBIC images (h-l) with similar accelerating voltages. Though the FIB milling was supposed to remove topographical effects completely, the ≈ 70 nm "curtains" distort the image in an obvious way. They can easily be seen in both EBIC and Q-EBIC images. Examination of grain boundaries reveals that, at lower accelerating voltages, EBIC has a higher resolution of grain boundaries than Q-EBIC.

Both EBIC and Q-EBIC exhibit similar results, when the electron beam is injected closer to the p-n junction, more photocurrent is collected, since minority carriers have less distance to travel and therefore have less of a chance to recombine. It is important to note that Q-EBIC produces a larger photocurrent than EBIC in the case of lower accelerating voltage. This is because photons with a wavelength of 620 nm penetrate a distance of ≈ 150 nm into the CdTe substrate, before the original intensity drops by a factor of 1/e.

3.2.3 Q-EBIC: Summary

A new photocurrent imaging technique is demonstrated on a CdTe solar cell. Though less resolution was achieved than EBIC, it is still a viable technique for measurement of photocurrent collection efficiency. This technique can also be used with different sized q-dots, for multi-wavelength spectroscopy. This approach combines the high speed and versatility of electron microscopy with optical microscopy by down-converting high energy electrons to local photons through cathodoluminescence in q-dots. The CdTe solar cell was not exposed to the high energy of the electron beam, as confirmed with CL spectra, as it is fully absorbed by the q-dots.

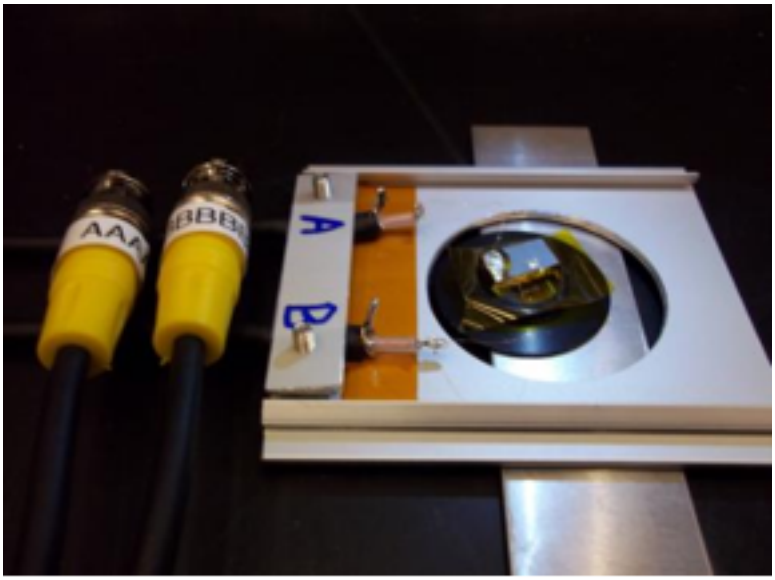

Figure 27: The sample holder used for the NSOM experiment. The wires are connected to BNC cable by indium solder.

3.3 NSOM

3.3.1 NSOM: Methodology

3.3.1.1 Sample Preparation As suggested in the beginning of section 3.2.1, the sample fabrication process is almost identical for both experiments. However, for the NSOM experiment, it is not crucial that the Au contact be transparent. Therefore, the only difference between fabrication methods, aside from q-dots, is a 100 nm Au contact instead of a 3 nm/7 nm Cu/Au contact.

The Q-EBIC experiment used a tungsten probe to collect photocurrent. However the NSOM experiment requires wires to be fastened to the Au contact. To fasten wires to the contact, a conductive epoxy was used. The large silver, out-of-focus, portion of Fig. 20 is a conductive silver epoxy which provides an electrical connection to the Au contact, shown as the corner of the gold-colored square, as well as a rigid mechanical support for the micron-sized wires. This epoxy was also used for completing the device circuit as the bottom, n-layer, contact.

The last part in creating the sample is to mount it on a custom-made sample holder designed for this experiment. Figure 27 shows the sample holder with CdTe sample mounted on it. The black disk located under the CdTe sample is a typical NSOM holder. The aluminum plate with BNC cable holders was designed for the special purpose to have a stable mount for the BNC cables within a near proximity of the sample. The wires connected the sample's contacts were connected to the BNC cables with indium solder. This whole stage was placed onto the NSOM stepper motor with double-sided tape.

3.3.1.2 Laser setup The ideal laser for this experiment would be one that is tunable across the visible and IR range, as well as holding a low-powered continuous output. Lasers like this can be custom made for an application, however for the scope of this project, attaining a laser of this quality would take a very large amount of time. The lasers used in this experiment were loaned from neighboring research groups. This allowed for quick setup and assistance.

The first laser used in this experimental setup was a 14 mW, 532 nm continuous wavelength (CW) laser. This was used for preliminary measurements to test the NSOM and the viability of the methods use for coupling with other lasers. The CW laser was focused to an optical fiber through a microscope objective. Though this is not the most efficient way to couple a laser to optical fiber, the fibers used in this experiment were only capable of holding 10 mW of power.

The next laser used in this experiment was a Ekspla NT242 optical parametric oscillator (OPO). An OPO laser consists of three different optical beams, a pump, a signal, and an idler. The pump laser, in this case, was a nanosecond pulsed neodymium-doped yttrium aluminum garnet (Nd:YAG) laser. The pump laser is incident upon a non-linear birefringent material. The electric field in the pump laser drives electrons in the nonlinear material. The oscillating electrons respond by generation of linearly and nonlinearly polarized waves determined by the polarizability of the medium. The induced nonlinear polarization couples

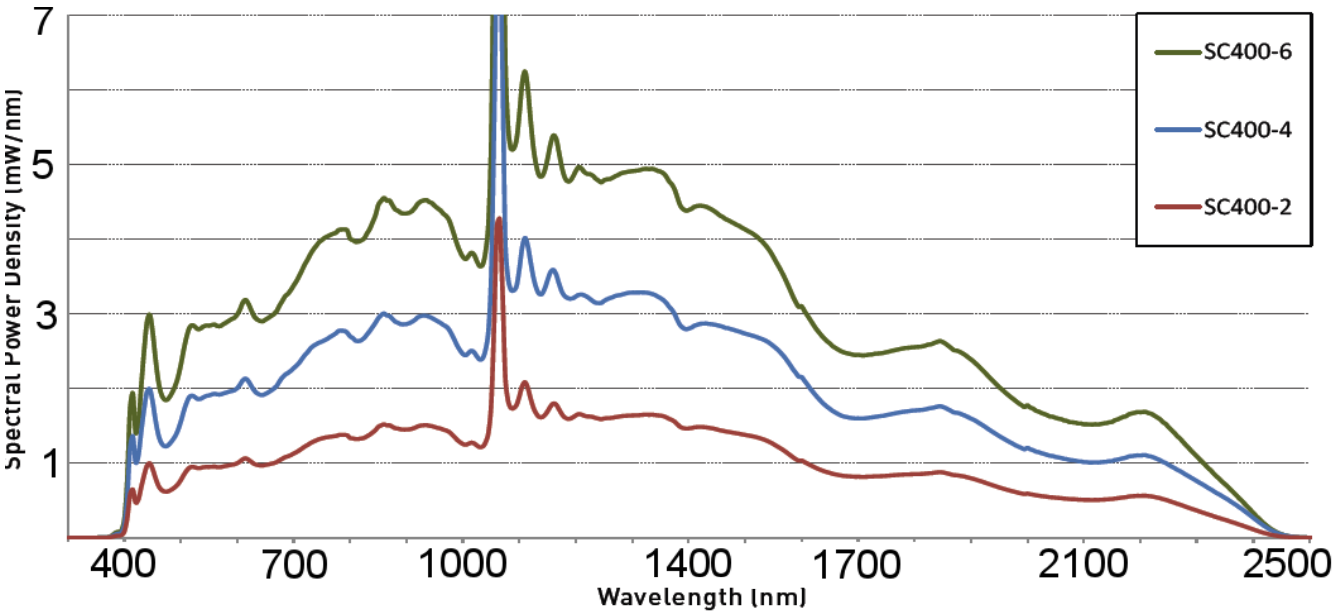

Figure 28: Fianium Supercontinuum laser output spectrum. The laser used in this experiment was the SC400-2, meaning maximum output of 2 W, integrated over the whole spectrum. The center wavelength used for spectral broadening is 1060 nm, with intensity dropping rapidly from there, producing the broad spectrum seen above [35].

the energy from the pump wave into two new tunable frequencies, signal and idler waves. Conservation of energy is demonstrated through the conservation of pump frequency, such that the frequency of the pumped laser is the sum of the signal and idler frequencies [34].

The OPO laser has a 1 nm tunable range of wavelengths from 405 nm to 2600 nm. The repetition rate of the laser beam is 1 kHz and the pulse width is 6-8 ns. For wavelengths ranging from 405-709 nm, it has a horizontal polarization, and for 710-2600 nm, it is vertical. Clearly this versatile laser can be used in many applications [34]. The OPO laser was coupled to the NSOM fiber with the use of neutral density filters and a parabolic reflector. The NSOM fiber was attached to a FC/APC patch cord, which easily connected to the parabolic reflector.

The last laser used in the NSOM experiment was a Fianium Supercontinuum Advanced Laser Platform (ALP). Supercontinuum lasers are made in several different ways. The laser in this experiment starts with a central wavelength of 1060 nm, as should be evident from

Fig. 28. This laser uses a femtosecond laser pules, at the central wavelength, through a photonic crystal fiber which broadens the spectrum of the beam to produce a white light laser beam with a large spectrum of wavelengths [36].

Figure 28 shows the spectrum of wavelengths from three different Fianium Supercontinuum lasers. The laser used in this experiment was SC400-2, the 2 denoting ≈2 W of integrated output power. The data sheet of the Fianium laser indicates that the repetition rate of the laser is 20 MHz, with a pulse width of ≈ 6 ps. This laser produces a circularly polarized beam of light containing a white light spectrum of wavelengths shown in Fig. 28. On average the spectrum contains spectral power of 1 mW/nm of power [35].

The set up for this laser was complete with some additional components. After the fiber output of the Supercontinuum laser, a dichroic mirror was used to reflect a large portion of the incident light, and transmit the rest, with >90% transmission for the wavelengths 520-985 nm. The dichroic mirror reflects ≈800 mW of power into a beam dump. The rest of the beam is transmitted without disruption into a double filter wheel containing several optical bandpass filters. The bandpass filters used for data acquisition were 532, 590, 610, 650, 700, 750, 800, 850, 860, 870, 880, and 900 nm all with a FWHM of 10 nm. The bandpass filters only allowed at most ≈ 5-6 mW of power into the parabolic reflector which then coupled the beam into an optical fiber, by use of FC/APC patch cord.

3.3.1.3 Measurement setup Adjusting the NSOM for a photocurrent measurement was trivial because the data acquisition box contains two extra auxiliary channels allowing for an undisturbed experimental set up. Figure 29 shows how the NSOM was adjusted for our photocurrent measurement. It can be viewed as a measurement external to the system. In fact, had the semiconductor substrate been transparent, an NSOM measurement could be obtained as well as photocurrent, however this was not in the scope of the thesis.

The AFM feedback loop allows for near-field photon injection, ≈ 10 nm, into the semiconductor. The resolution of the NSOM measurement is restricted by the tip of the NSOM

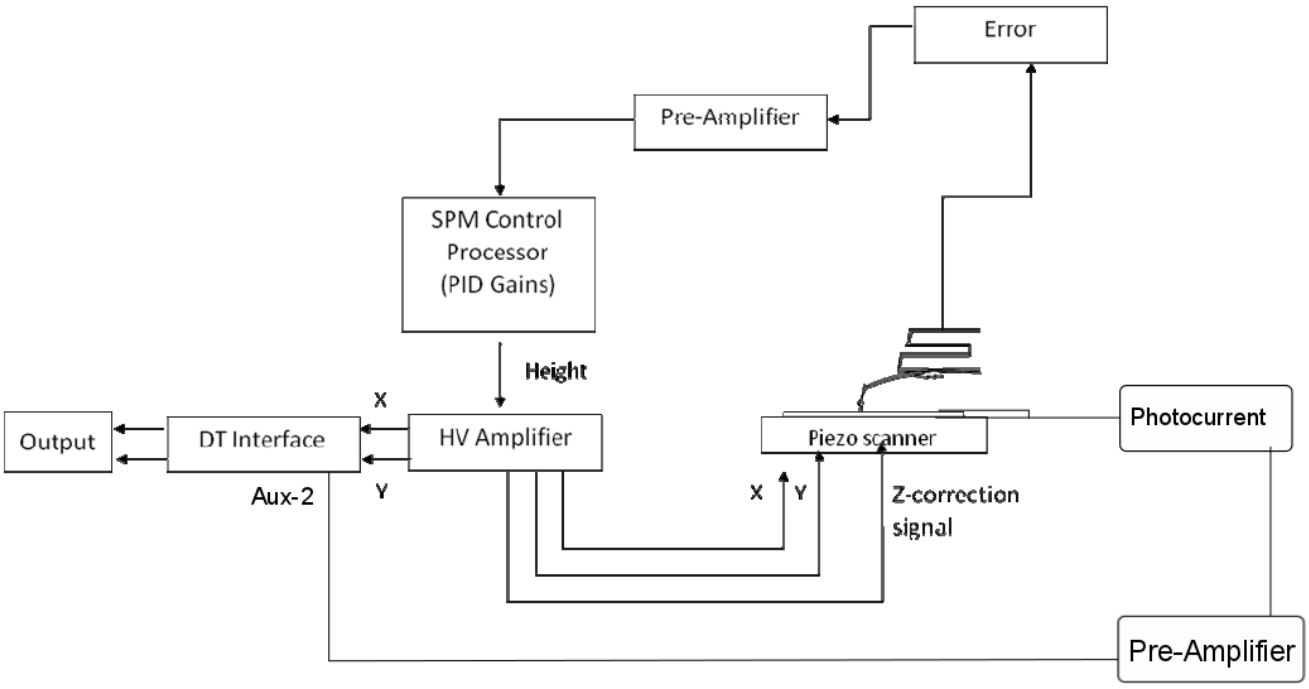

Figure 29: Experimental set-up used for the NSOM data acquisition. The operation is of a typical NSOM with AFM feedback loop, except we do not collect far-field diffraction data. Instead, the AUX-2 channel is used to collect photocurrent data after it passes through the current amplifier.

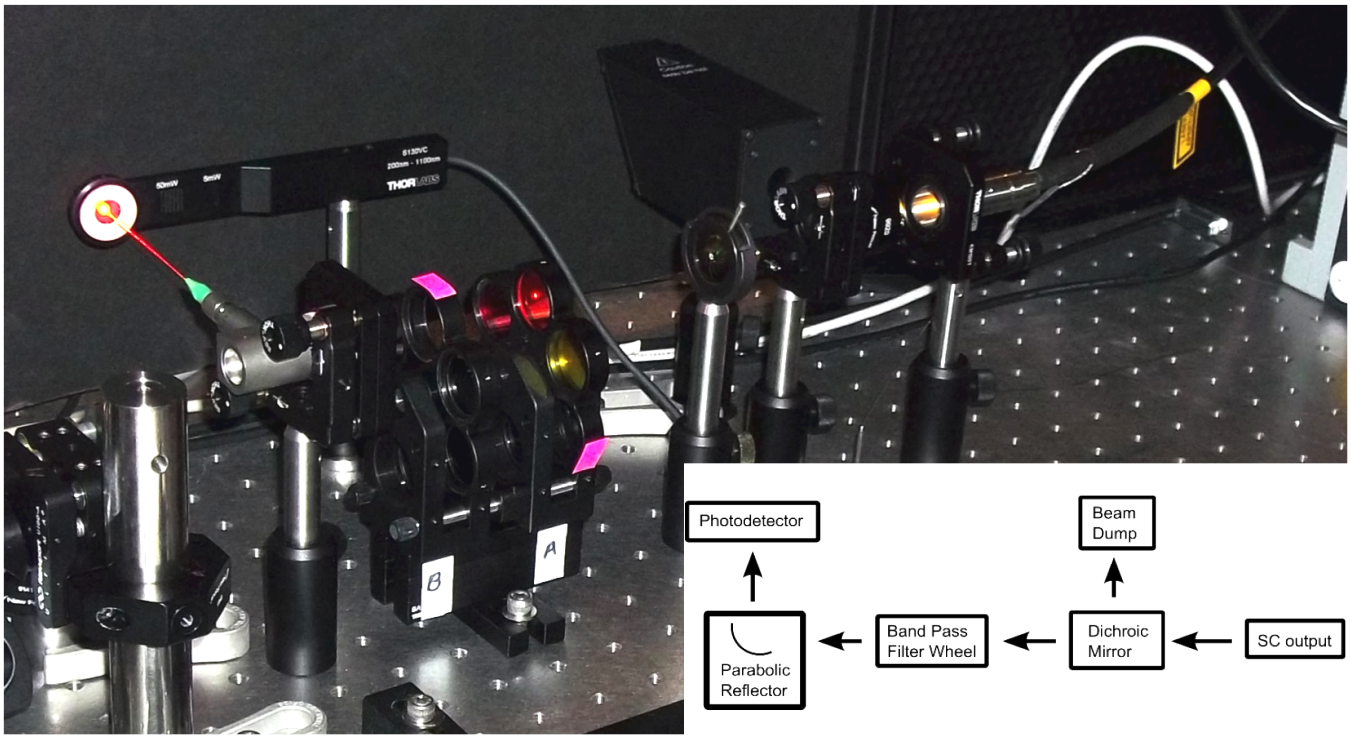

Figure 30: Experimental set-up of Fianium laser on optical table. Inset shows the layout and beam direction, as well as labels of the optical items used. Beam starts from the supercontinuum fiber output in a collimated beam, then goes through a dichroic mirror and bandpass filters. The parabolic mirror focuses the beam and couples it to the optical fiber. The photodetector is used as a calibration tool.

probe, 50-500 nm, and the absorption depth of the specific injected wavelength. Using the feedback with an XY scanning stage, topography and spatial variation of photocurrent are obtained. Light is either injected normal to the p-layer or through the cross-section.

To measure the power output coming from the NSOM fiber into the surface of the semiconductor, we placed a commercially purchased photodetector on the NSOM scanning stage and simulated a regular measurement with NSOM tip approached. This was done for each laser setup. The amount of power injected into the device was largely based on the power coupled to the fiber, as well as the diameter of the NSOM tip. If the tip of the NSOM probe is damaged, a larger amount of power would be transmitted.

The Fianium laser required an adjustment each time the bandpass filter wheel was turned. Microscopic changes in the position of the bandpass filter or parabolic reflector resulted in

a misalignment, or loss of power, of the beam to fiber coupling. It was important that the NSOM tip stay in contact with the sample being measured, so recalibrating the NSOM fiber output was not an option. To go around this, we used a "mock" NSOM fiber, which was a terminated optical fiber from a broken NSOM probe. Figure 30 shows this terminated fiber shining light onto a photodetector. By optimizing the same fiber outside of the measurement apparatus, we could ensure that the optimized alignment would be sent to the substrate in the NSOM apparatus. This procedure had to be repeated for each bandpass filter, because the optical alignment changed for each filter, due to microscopic changes in filter alignment.

3.3.2 NSOM: Results and Discussion

Each measurement was taken with the same incident power onto the substrate. This was attained by ensuring that the power coming out of the fiber was the same for each wavelength. Also, measurements with variation in incident power were performed for the green CW laser. The results shown here are interesting because measurements were performed with large topography variations and with none, by using a FIB to mill a wedge into the CdTe substrate.

3.3.2.1 Measurement with CW Laser The first measurement performed was to vary incident power to the semiconductor substrate with the use of a neutral density filter. This was to examine the change in photocurrent collection under different illumination intensity. To measure the intensity of the incident laser beam, we used a silicon photodetector and the NSOM feedback loop to approach the surface of the photodetector.

The neutral density filters on a filter wheel allowed us to easily vary the incident power while still scanning on the same area. Figure 31 shows the topographic scan of p-layer CdTe, with a peak to valley value of 1.5 μm. The center image is a photocurrent image of p-layer CdTe where the incident power was $\approx$ 27 nW. There are large peaks in photocurrent at the grain boundaries and reduced photocurrent at the grain centers. When the incident power

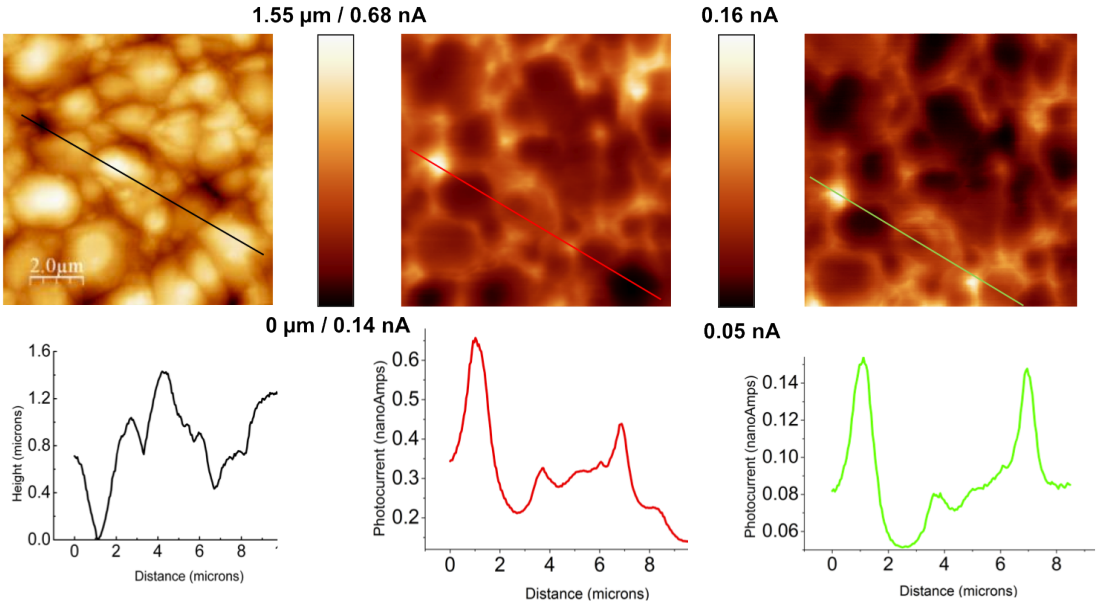

Figure 31: Left) The topography of a CdTe p-layer. The black line corresponds to a line scan of topography from the image. Mid) Photocurrent response on same spot of solar cell as obtained topography. Notice large spikes in photocurrent collection at GB. Incident power from tip is 27 nW. Right) Photocurrent response from an incident power of 2.2 nW. All of the line scans are over the same peaks and valleys of topography.

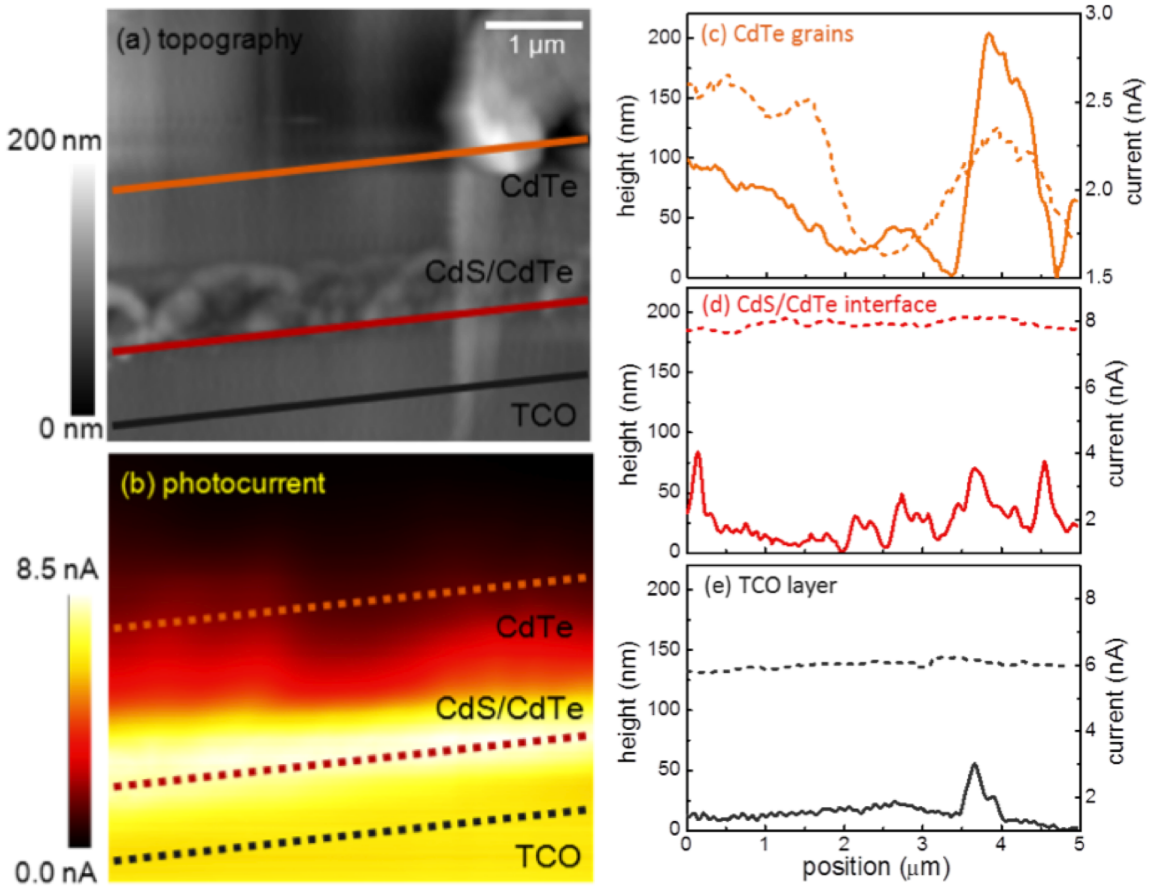

Figure 32: a) Topographic scan of a cross-section of CdTe/CdS p-n junction. b) Photocurrent image of cross section. c) photocurrent line scan corresponding to orange (color) line in topographic and photocurrent image. Solid line corresponds to topography and dotted line with photocurrent. d) Line scan of collected photocurrent, on the p-n junction. e) Topography and photocurrent line scan of glass portion of p-n junction. Optical beams travel through glass, through the window layer to produce photocurrent.

is reduced to 2.2 nW, as in the right figure of Fig. 31, the same features remain, but with different magnitude. Below each image is a line scan corresponding to the same spot for topography and both photocurrent images.

It is clear from these adjacent images that photocurrent is indeed increased in the grain boundaries. Also, it should be clear that even though values in maximum and minimum collected photocurrent may vary, the overall device variations remain proportionally the same.

The next measurement performed with the CW laser was a cross-section topography and

photocurrent scan. Figure 32 shows images of topography and photocurrent of the same area as well as line scans of different distances away from the p-n junction. The topography scan a) shows variations in surface height of around 200 nm, which may be a result of tilted substrate or large artifacts present in the image. It is clear that the smaller grain portion of the image is the n-type CdS.

The corresponding photocurrent image b) shows a large amount of photocurrent collected at the p-n junction, with exponential decay of collected photocurrent as distance away from p-n junction is increased. Variation in photocurrent collection is seen across a line scan of p-type CdTe c), while little to no current variation is present on the p-n junction d). Spatial variations along the same distance away from p-n junction show variations in photocurrent. Though no grain structure can be seen in a), the photocurrent image, b), shows them.

Though it seems as though there is some collected photocurrent on the glass/TCO substrate, e), this is due to a non-local scattering effect. Photons travel through the glass substrate, through the window layer and into the p-type absorber CdTe. Figure 33 shows the fundamental difference between EBIC and NSOM. In EBIC we use an electron beam to excite e-h pairs, however, when an EBIC beam is placed over glass, electrons cannot reach the semiconductor to produce current. In NSOM, the photons easily travel through the glass.

3.3.2.2 Multi-wavelength NSOM with OPO laser The OPO laser used in this experiment allowed for great flexibility in terms of wavelength tuning. However, the pulse rate of the OPO laser was a factor of ten slower than the resonant frequency of the NSOM tip. Figure 34 shows the laser illumination points as a function of tuning fork amplitude. Every 100 ms, a 1 ns long blast of photons would hit the solar cell surface, this type of illumination caused for noise in the photocurrent images. To overcome this setback, the pre-amplifier was set to use a 10 Hz low pass filter. The low-pass filter allowed the photocurrent pulses from slow laser pulses, shown in Fig. 34, to disappear.

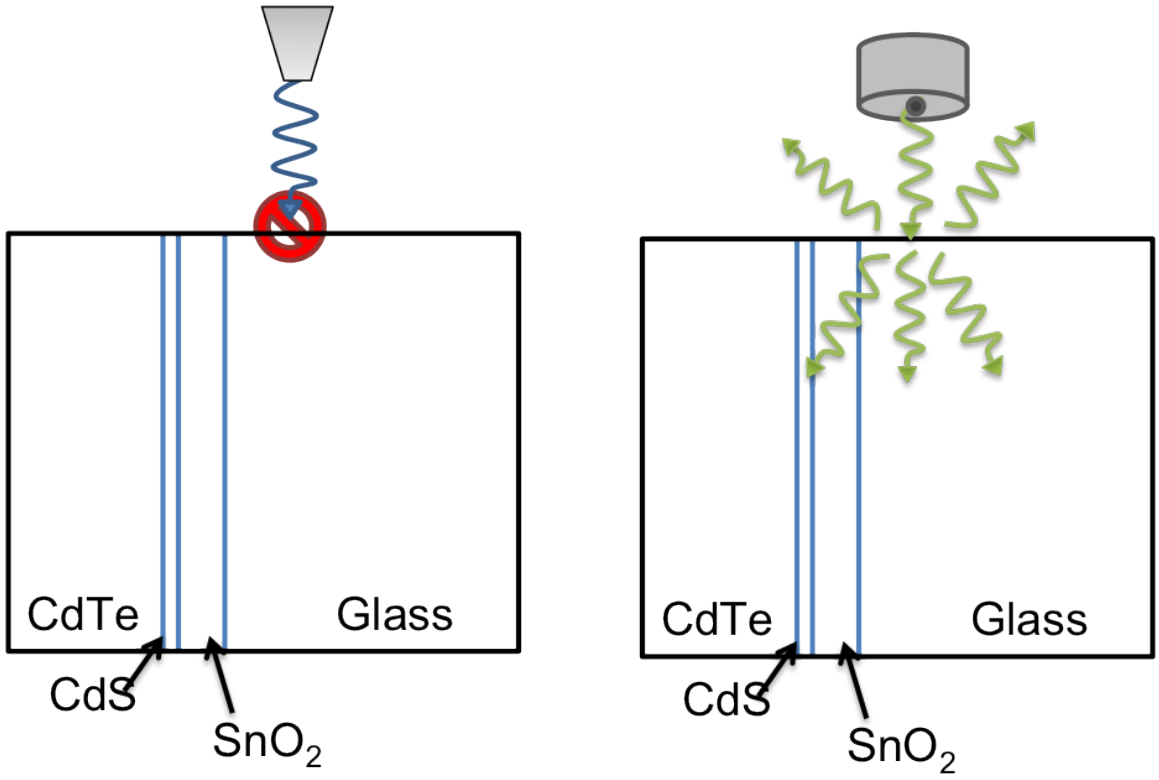

Figure 33: When an electron beam is placed over glass, no current is induced because no electrons can travel thorough the insulator. However, photons can travel through glass and produce non-local photocurrent after being scattered.

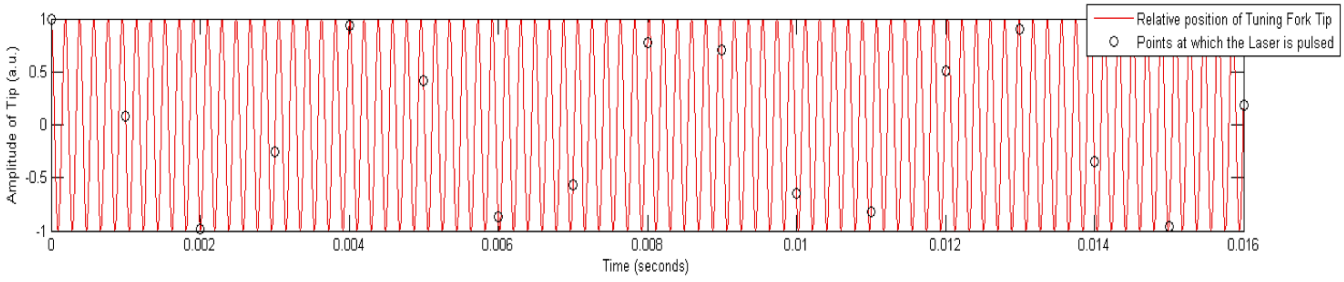

Figure 34: The tuning fork has a resonant frequency of approximately 32 kHz. The OPO laser has a pulse width on the order of nanoseconds, with a pulse rate of 1 kHz. A simulation of the NSOM tip and tuning fork are shown here.

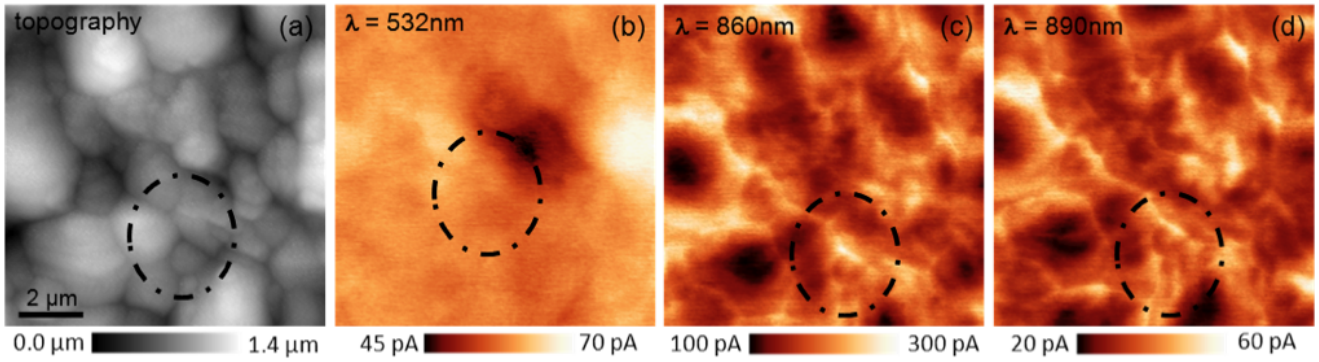

Figure 35: Multi-wavelength NSOM scans for green photons, wavelength of 532 nm, and infrared photons, >850 nm, near the band gap. Here we can see significantly different behavior from the three different photocurrent scans. The injection volume of the larger wavelengths increases with wavelength, however resolution is not destroyed, and finer grain structures are revealed.

The most interesting results were obtained with wavelength of 532 nm and wavelengths both above and below the band edge. As the band edge is approached, the injection volume is expected to increase as penetration depth increases, as shown in Fig. 36. It is also important to examine the change in collected photocurrent as a function of injected wavelength. Figure 35 shows a multi-wavelength NSOM measurement of p-layer CdTe with topography, in a), and three different wavelengths. A wavelength of 532 nm is chosen for comparison with the CW laser used in the previous measurement setup.

The low amount collected photocurrent in Fig.35 a) was competing with the noise of the system, thus resulting in a noisy image. The variation in the collected photocurrent, however, does match that of the images shown in the previous section for 532 nm. As the incident wavelength is increased, photon energy is lowered, and finer grain structures start to appear even though absorption depth is increasing. When the incident wavelength was at the band edge, 860 nm, a relatively large amount of photocurrent was still being collected. When the wavelength was increased further, less photocurrent was collected and the fine grain structures remained, with very small changes.

The fundamental operation of the OPO laser produces intrinsic noise into the signal of

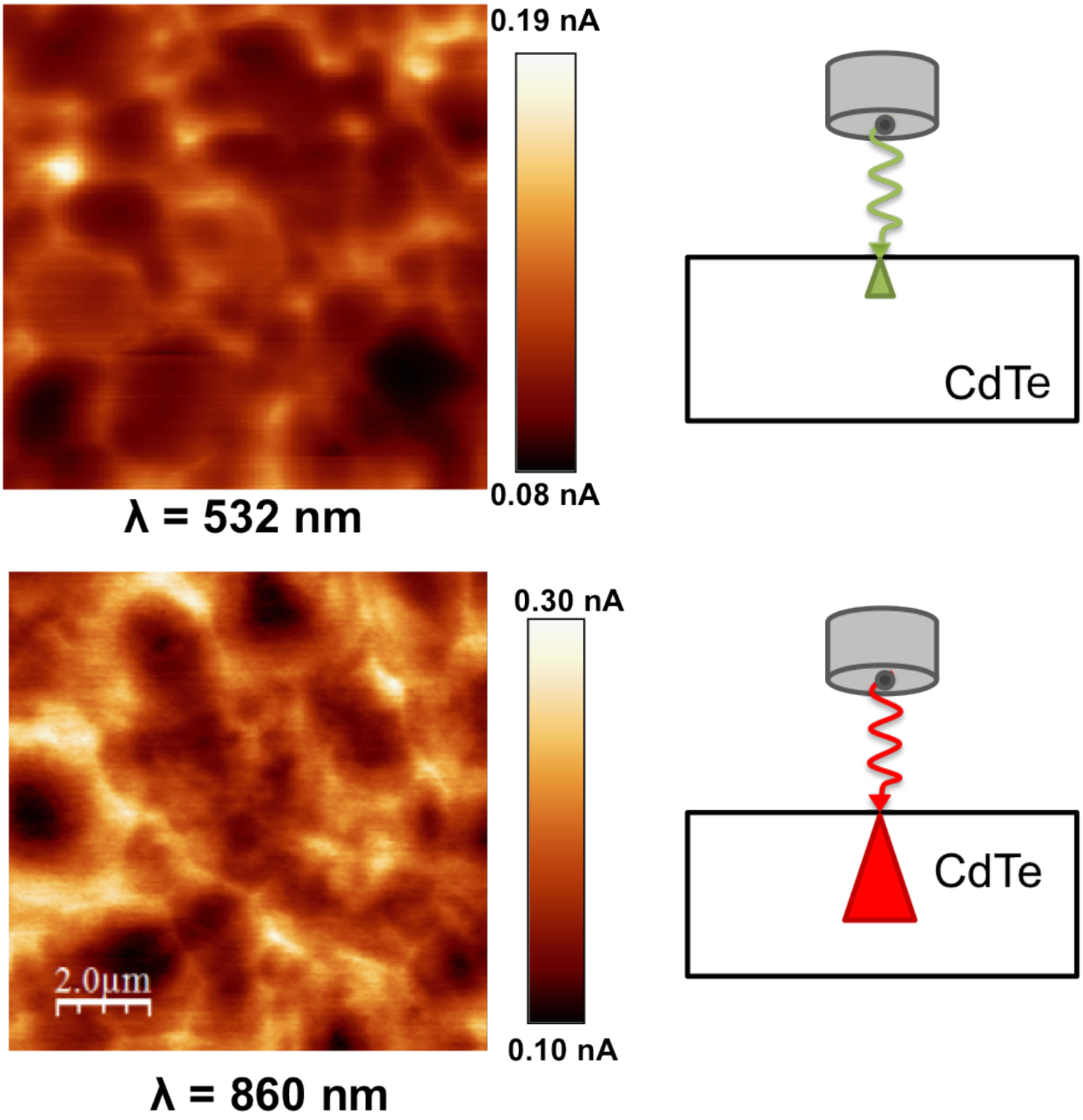

Figure 36: Penetration depth and injection volume of green photons versus red photons. Green photons should produce an image with better resolution because of the small injection volume, whereas red photons inject a larger area, creating more photocurrent, and thus less spatial resolution. Though the images for larger wavelength should become blurry, they are actually more detailed.

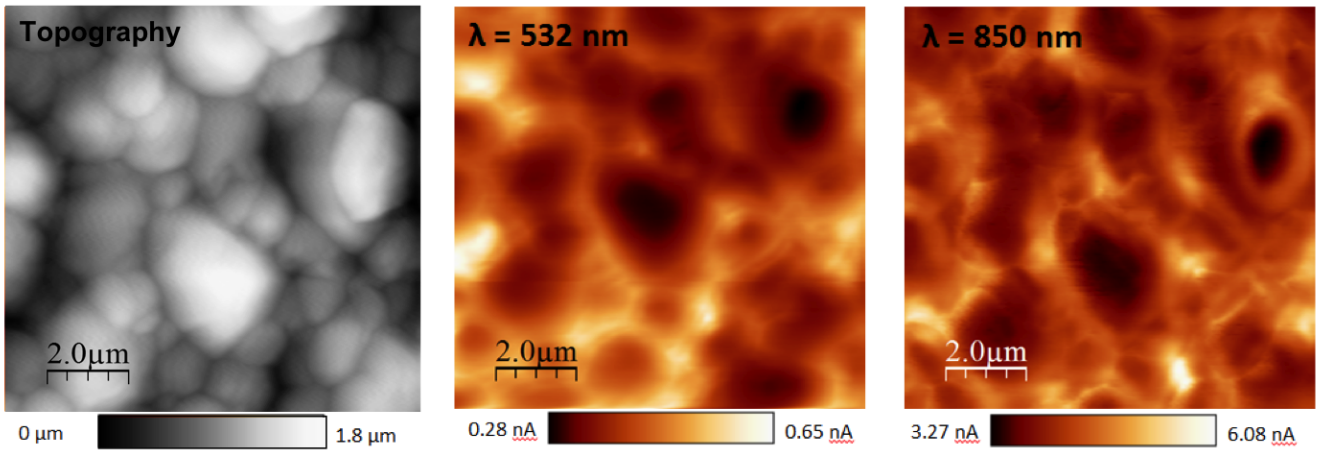

Figure 37: Left image shows topography of scanned area. Middle image shows photocurrent map of 532 nm bandpass filter. Right image shows 850 nm bandpass filter. Notice how fine structures appear at the wavelength close to the band edge similar to the OPO laser.

photocurrent collection. The oscillations used to produce the output wavelength cause in a non-steady value for incident power. Though extra noise was introduced, the OPO laser was very useful for examining variation in incident wavelength. It was found that as penetration depth is increased, finer grain structures are revealed, contrary to intuition.

3.3.2.3 Multi-wavelength NSOM with Fianium Supercontinuum laser To further examine the results found with the OPO laser, another laser was introduced to compare results. The Fianium Supercontinuum laser allowed for a steady output of power, with repetition rate on the order of nanoseconds, similar to the CW laser. The only difference was that optical bandpass filters were used, so single wavelength variation was not achieved. Instead the variations consisted of a 10 nm FWHM grouping around the center wavelength, as previously explained.

The results with the Supercontinuum laser are shown in Fig. 37. The image labeled topography shows the typical grain structure of p-layer CdTe. Next to it is the photocurrent map of the 532 nm bandpass filter. The same contrast is seen in this image as with the CW and OPO laser. As bandpass filter is gradually changed, by increments of 50 nm, fine structures begin to appear. At 850 nm, the photons should be penetrating through the

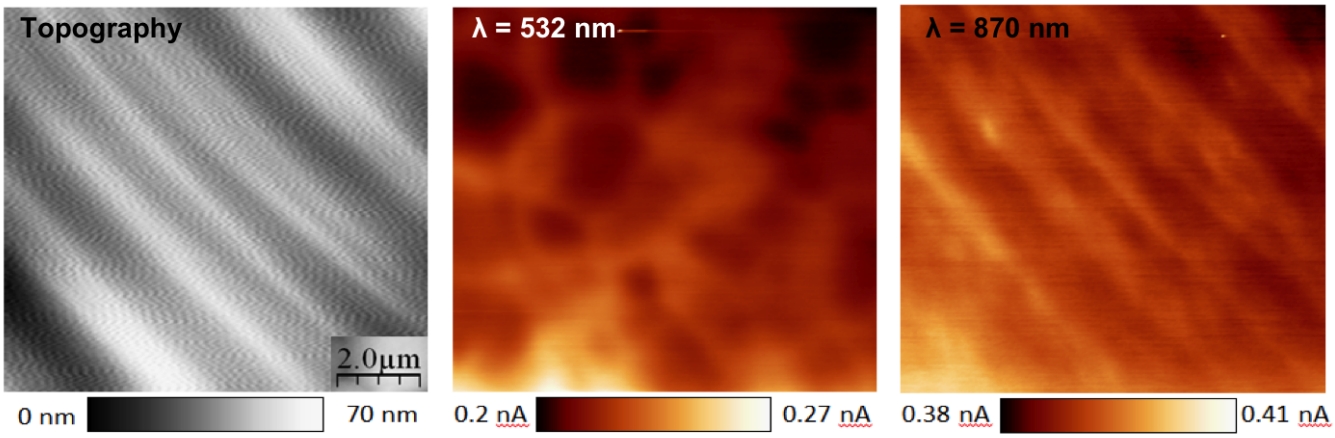

Figure 38: Left image shows topography of scanned area. Middle image shows photocurrent map of 532 nm bandpass filter. Right image shows 850 nm bandpass filter. Notice how fine structures appear at the wavelength close to the band edge similar to the OPO laser.

p-layer CdTe, however, as seen with the OPO laser, we see fine grain structures not seen with the 532 nm bandpass filter.

To eliminate the possibility of topography interacting with probe tip, a focused ion beam was used to mill away the ≈ 1.5 μm peak to valley crystal structure. The resulting topography scan, shown in Fig. 38, is a 70 nm height variation. The diagonal lines in the image are artifacts created from the milling process, they have no relation to the ≈ 1.5 μm grains that were once present. In the middle image of Fig. 38, we see the same variations that were present in all other images using 532 nm photons. When the wavelength is changed closer to the band edge, the variations are less obvious, but still present.

It is seen that at wavelengths where the penetration depth is close to the surface of the substrate. With this type of wavelength, it is clear that the GBs are indeed more efficient local photocurrent transporters than the GIs. However, when the wavelength is increased, along with penetration depth, finer structures appear. These finer structures arise from increased photocurrent deep within the p-layer CdTe. Since we have no information about grain depth when doing topography scans, it is impossible to say whether or not the increased photocurrent is within a grain or below it.

3.3.3 NSOM: Summary

The local measurement of the electronic properties of the grains and their interfaces in thin film solar cells by multi-wavelength NSOM represents an important step towards the understanding of enhanced device performance. The increased photocurrent collection at grain boundaries has been verified with the use of multi-wavelength NSOM and a milled CdTe sample. Unexpectedly, fine grain structures were revealed at large penetration depths. The use of NSOM as a viable multi-wavelength measurement technique has been confirmed.

4 Summary and Future Work

To properly dissect the nanoscale physics occurring in a semiconductor, it is important to have a developed measurement technique. It is also important that the resolution of the technique is on the relevant length scale. This was indeed the case when Q-EBIC measurement images were placed next to EBIC images. We could see that even though the images had slightly less resolution, the same physics was observed. When the same measurements were performed with a laser, NSOM, still the same physics was observed, confirming these two techniques as viable measurement methods.

This thesis presents a successful new photocurrent imaging approach that combines the high speed and versatility of electron microscopy with optical microscopy by down-converting high energy electrons to local photons through cathodoluminescence (CL) in quantum dots. The near- field CL of the q-dot layer emits very bright light, and the generated photocurrent exceeds the direct EBIC signal within a usable range of parameters. Beyond the immediate application to the local characterization of various types of solar cells and optoelectronic devices, the approach has general advantages for a broad range of microscopies. The sample under study is not exposed to direct electron beam irradiation as the incident beam is fully absorbed in the layer of quantum dots conforming to the sample surface. We also tested the possibility of using an NSOM for multi-wavelength spectroscopy, and have successfully created a methodology to do so.

The next step in the measurement process is to compare the physics presented by both methods on similar length scales. By introducing different sized q-dots to the surface of CdTe, a multi-wavelength Q-EBIC can be successfully demonstrated using the methodology presented in this thesis. The techniques presented demonstrate the versatility to be used in a variety of different ways not presented here. For example, the technique can be used to probe the photo-electronic properties of the devices under forward bias (at V_oc operation) and can be expanded to other polycrystalline materials, such as Copper Indium Gallium Selenide, crystalline Si, and amorphous Si.

Further work, important for understanding loss in efficiencies of CdTe, will be focused on obtaining calibrated samples with known fabrication processes. Having a sample with known properties is extremely important for developing a detailed model to simulate the behavior between the CdTe and near-field Q-dot emission or NSOM probe to surface coupling.

We were able to map and quantify the photocurrent generated at CdTe solar cells GBs under different illumination conditions. The local measurement of the electronic properties of the GBs and GCs in thin film solar cells by Q-EBIC and LBIC microscopy represents an important step towards the understanding of how GBs favor device performance, and can be used to engineer the chemical composition of the grains in order to enhance the V_{oc} and I_{sc} of the device.

References

[1] International Energy Agency. World Energy Outlook 2012: Executive Summary. booklet, IEA PUBLICATIONS, 9 rue de la Feferation, 75739 Paris Cedex 15, November 2012.

[2] S. Shafiee and Erkan Topal. When will fossil fuel reserves be diminished? *Energy Policy*, 37(1):181–189, 2009.

[3] M. M. Hand, S. Baldwin, E. DeMeo, J. M. Reilly, T. Mai, D. Arent, G. Porro, M. Meshek, D. Sandor,. Renewable Electricity Futures Study (Entire Report). Technical report, National Renewable Energy Laboratory, Golden, CO, 2012.

[4] Martin A. Green, Keithe Emery, Yoshihiro Hishikawa, Willhelm Warta, Ewan D. Dunlop. Solar cell efficiency tables. *Progress in Photovolatics: Research and Applications*, 21(1):1–11, January 2013.

[5] Rolf Brendel. *Thin-Film Crystalline Solar Cells*. Wiley-VCH, 1 edition, March 2003.

[6] Brian E. McCandles and James R. Sites. *Hanbook of Photovoltaic Science and Engineering*. John Wiley and Sons, 2003.

[7] I. Visoly-Fisher, S. R. Cohen, K. Gartsman, A. Ruzin, D. Cahen. Understanding the Beneficial Role of Grain Boundaries in Polycrystalline Solar Cells from Single-Grain-Boundary Scanning Probe Microscopy. *Advanced Functional Materials*, 16:649–660, 2006.

[8] Neil W. Ashcroft, N. David Mermin. *Solid State Physics*. Brooks Cole, 1 edition, January 1976.

[9] H. P. Yoon, D. A. Ruzmetov, P. M. Haney, M. S. Leite, B. H. Hamadani, A. A. Talin, N. B. Zhitenev. High-Resolution Local Current Measurement of CdTe Solar Cells. *IEEE Photovoltaic Specialists Conference*, 38:003217–003219, October 2012.

[10] T. P. Thorpe, Alan L. Fahrenbruch, R. H. Bube. Electrical and optical characterization of grain boundaries in polycrystalline cadmium tellruide. *Journal of Applied Physics*, 60(10):3622, July 1986.

[11] National Renewable Energy Labratory. NREL: Photovoltaics Research - Polycrystalline Thin-Film Materials and Devices R and D. webpage, October 2011.

[12] D. H. Rose, F. S. Hasoon, R. G. Dhere, D. S. Albin, R. M. Ribelin, X. S. Li, Y. Mahathongdy, T. A. Gessert, P. Sheldon. Fabrication Procedures and Process Sensitivities for CdS/CdTe Solar Cells. *Progress in Photovolatics: Research and Applications*, 7(5):331–340, October 1999.

[13] Peter Wurfel. *Physics of Solar Cells*. Wiley-VCH, 2 edition, March 2009.

[14] B. E. McCandless, L. V. Moulton, R. W. Birkmire. Recrystallization and sulfur diffusion in $CdCl_2$-treated CdTe/CdS thin films. *Progress in Photovolatics: Research and Applications*, 5(4):249–260, July 1997.

[15] Newport. Oriel Product Training: Solar Simulation. Online Product Manual, Stratford, CT, 2012.

[16] M. C. Teich B. E. A. Saleh. *Fundamanetals of Photonics*. John Wiley and Sons, 1991.

[17] D. Zuba, C. Lopez, M. Rodrigues, A. Escobedo, S. Oyer, L. Romo, S. Rogers, S. Quinonez, J. Mclure. Ordered CdTe/CdS Arrays for High-Performance Solar Cells. *Journal of Electronic Materials*, 36(12):1599–1603, 2007.

[18] L. M. Woods, G. Y. Robinson, and D. H. Levi. The effects of $CdCl_2$ on CdTe electrical properties using a new theory for grain-boundary conduction. *28th IEEE Photovoltaic Specialists Conference*, pages 603–606, 2000.

[19] P. R. Edwards, S. A. Galloway, and K. Durose. EBIC and luminescence mapping of CdTe/CdS solar cells. *Thin Solid Films*, 361-362:364–370, 2000.

[20] B. G. Mendis and K. Durose. Prospects for electron microscopy characterisation of solar cells: Opportunities and challenges. *Ultramicroscopy*, 199:82–96, November 2012.

[21] T. A. Gessert, S. Smith, T. Moriarty, M. Young, S. Asher, S. Johnston, A. Duda, C. DeHart, A. L. Fahrenbruch. Evolution of CdS/CdTe Device Performance During Cu Diffusion. *IEEE Photovoltaic Specialists Conference*, 31, February 2005.

[22] S. I. Maximenko. Application of CL/EBIC-SEM techniques for characterization of irradiation induced defects in triple junction solar cells. *IEEE Photovoltaic Specialists Conference*, 35:001753–001758, June 2010.

[23] Jian Cui. Bawendi Group Research. webpage.

[24] G. A. Farias, J. S. de Sousa. *Handbook of Nanophysics: Nanoparticles and Quantum Dots*. Number Chapter 35. CRC Press, 1 edition, September 2010.

[25] Hideki Ooba. Advanced Industrial Science and Technology No. 21 Summer 2006. Research Booklet, June 2006.

[26] Tapas Kar. 21st Century Physics Flexbook "Nanoscience". eBook, September 2009.

[27] Jason F. Hiltner. Investigation of Spatial Variations in Collection Efficiency of Solar Cells. PhD Thesis, May 2001.

[28] Hans Hallen. Introduction to NSOM. webpage, Septmeber 2000.

[29] E. Betzig, A. Lewis, A. Harootunian, M. Isaacson, E. Kratschmer. Near-Field Scanning Optical Microscopy (NSOM). *Biophysical Journal*, 49:269–279, January 1986.

[30] Olympus America. Olympus Microscopy Resource Center — Near-Field Scanning Optical Microscopy. webpage, October 2012.

[31] M. K. Herndon, A. Gupta, V. Kaydanov, R. T. Collins. Evidence for grain-boundary-assisted diffusion of sulfur in polycrystalline CdS/CdTe heterojunctions. *Applied Physics Letters*, 75(22):3503, July 1999.

[32] C. J. Brinker A. J. Hurd. Fundamentals of sol-gel dip-coating. *Journal of Physics III (France)*, 4:1231–1242, July 1994.

[33] MTI Corporation. TL0.01 Desktop Dip Coater: Operation Manual. Operation Manual, 860 19th ST, Richmond, CA 94804, USA.

[34] H. Rabin and C. L. Tang. *Quantum Electronics: A Treatise (Nonlinear Optics)*, volume 1. Academic Press Inc, 1 edition, April 1975.

[35] T. Naugler. WhiteLase-SC4x0. Product datasheet, Fianium, 2010.

[36] M. Suzuki, M. Baba, S. Yoneya, H. Kuroda. Efficient spectral broadening of supercontinuum in photonic crystal fiber with self-phase modulation induced by femtosecond laser pulse. *Applied Physics Letters*, 101(19), November 2012.

[37] A. F. E. Hezinger, A. M. Goepferich, J. K. Tessmar. *Handbook of Nanophysics: Nanoparticles and Quantum Dots*. Number Chapter 36. CRC Press, 1 edition, September 2010.

[38] James P Connolly and Denis Mencaraglia. *Materials Challenges: Inorganic Photovoltaic Solar Energy - RSC Energy and Environment Series*, volume 1. Royal Society of Chemistry, 1 edition, July 2013.

[39] Frank Kreith and D. Yogi Goswami, editors. *Handbook of Energy Efficiency and Renewable Energy*. CRC Press, 2007.

A Additional Data: NSOM

A.1 Unmodified CdTe Surface

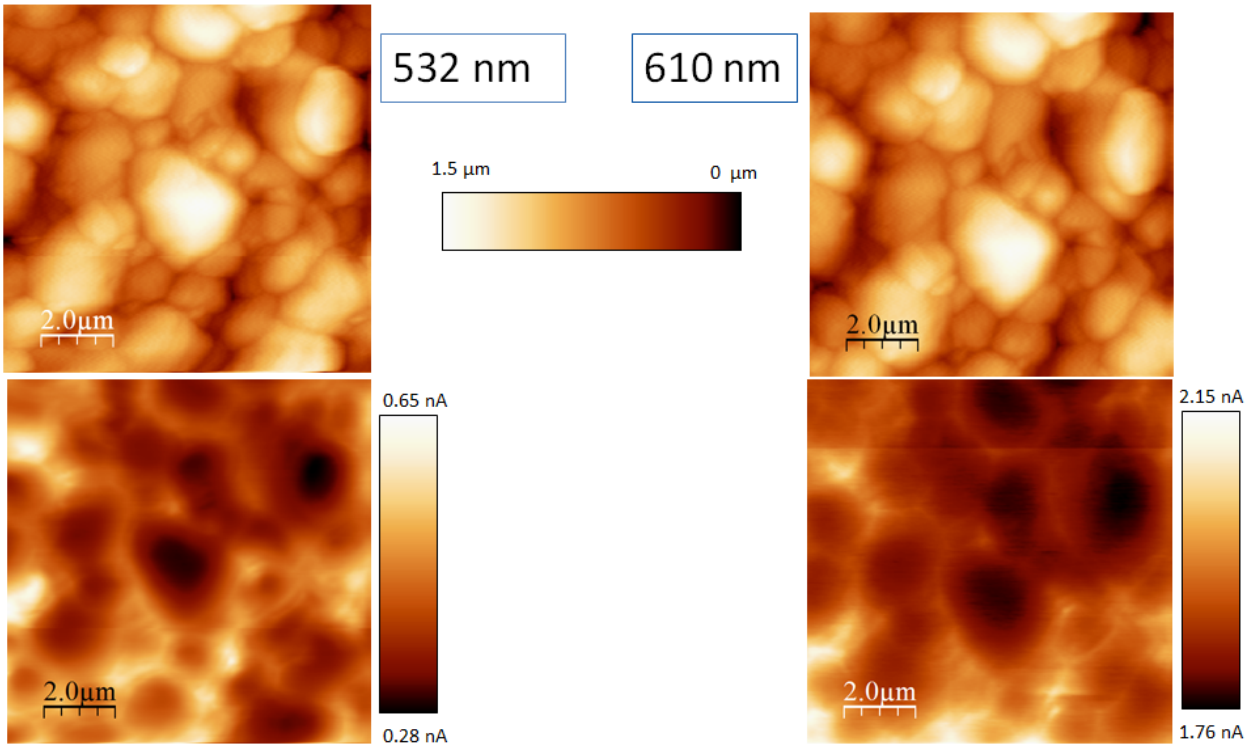

Figure 39: Simultaneously obtained topography (top) and photocurrent (bottom) images of CdTe topography. The image on the left was taken with a 532 nm optical band pass filter, and the image on the right was obtained with 610 nm. The scale bar in the middle of the image corresponds to both topography images.

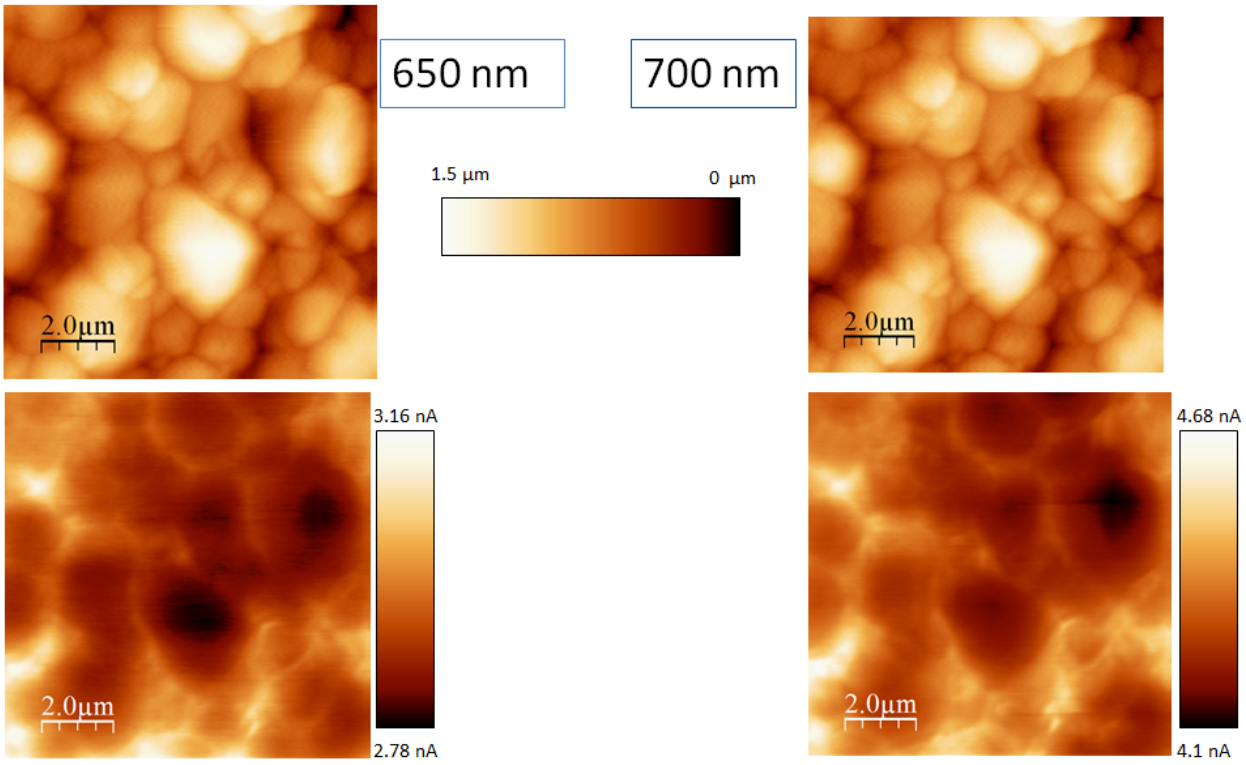

Figure 40: Simultaneously obtained topography (top) and photocurrent (bottom) images of CdTe topography. The image on the left was taken with a 650 nm optical band pass filter, and the image on the right was obtained with 700 nm. The scale bar in the middle of the image corresponds to both topography images.

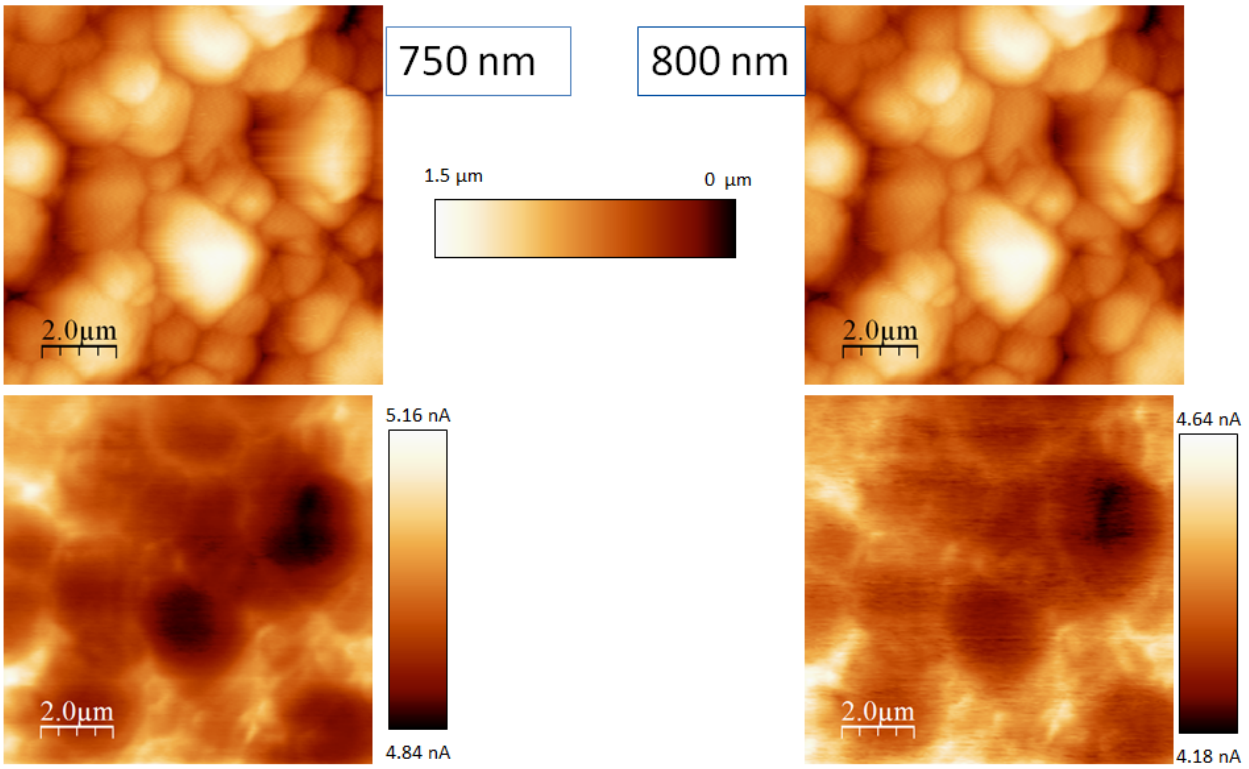

Figure 41: Simultaneously obtained topography (top) and photocurrent (bottom) images of CdTe topography. The image on the left was taken with a 750 nm optical band pass filter, and the image on the right was obtained with 800 nm. The scale bar in the middle of the image corresponds to both topography images.

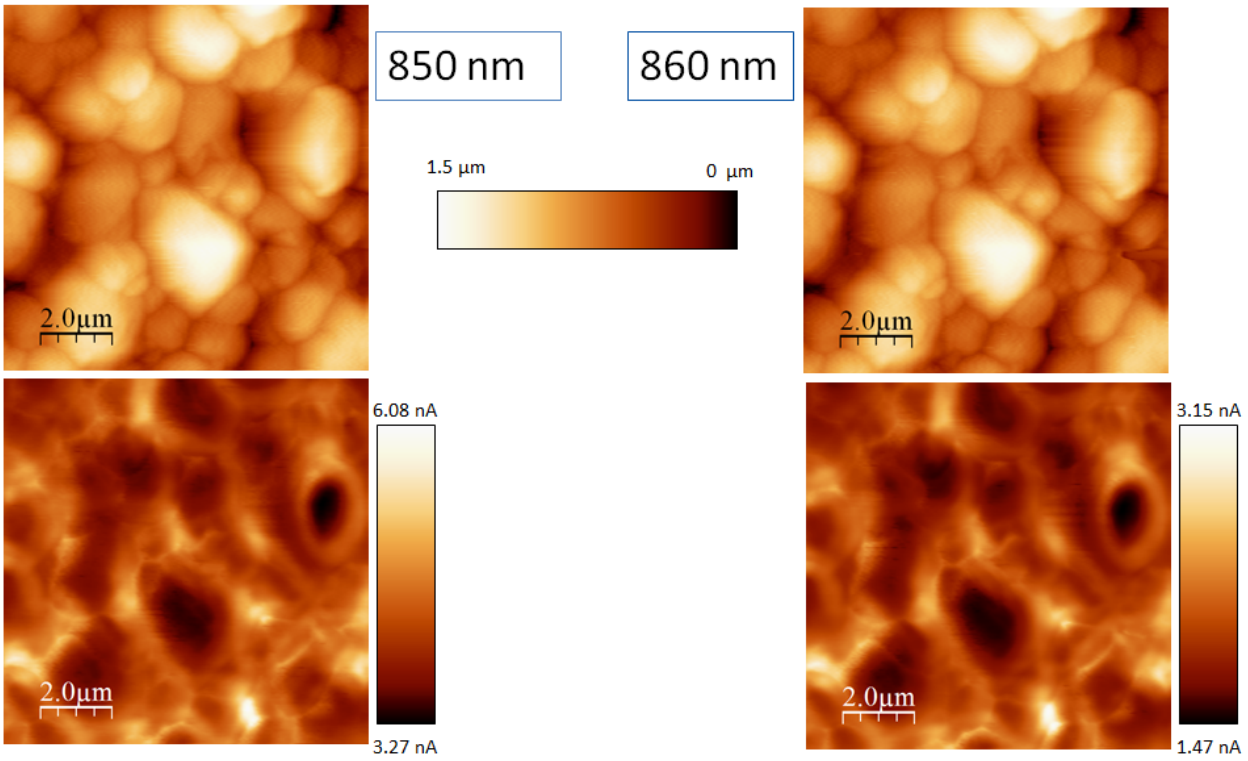

Figure 42: Simultaneously obtained topography (top) and photocurrent (bottom) images of CdTe topography. The image on the left was taken with a 850 nm optical band pass filter, and the image on the right was obtained with 860 nm. The scale bar in the middle of the image corresponds to both topography images.

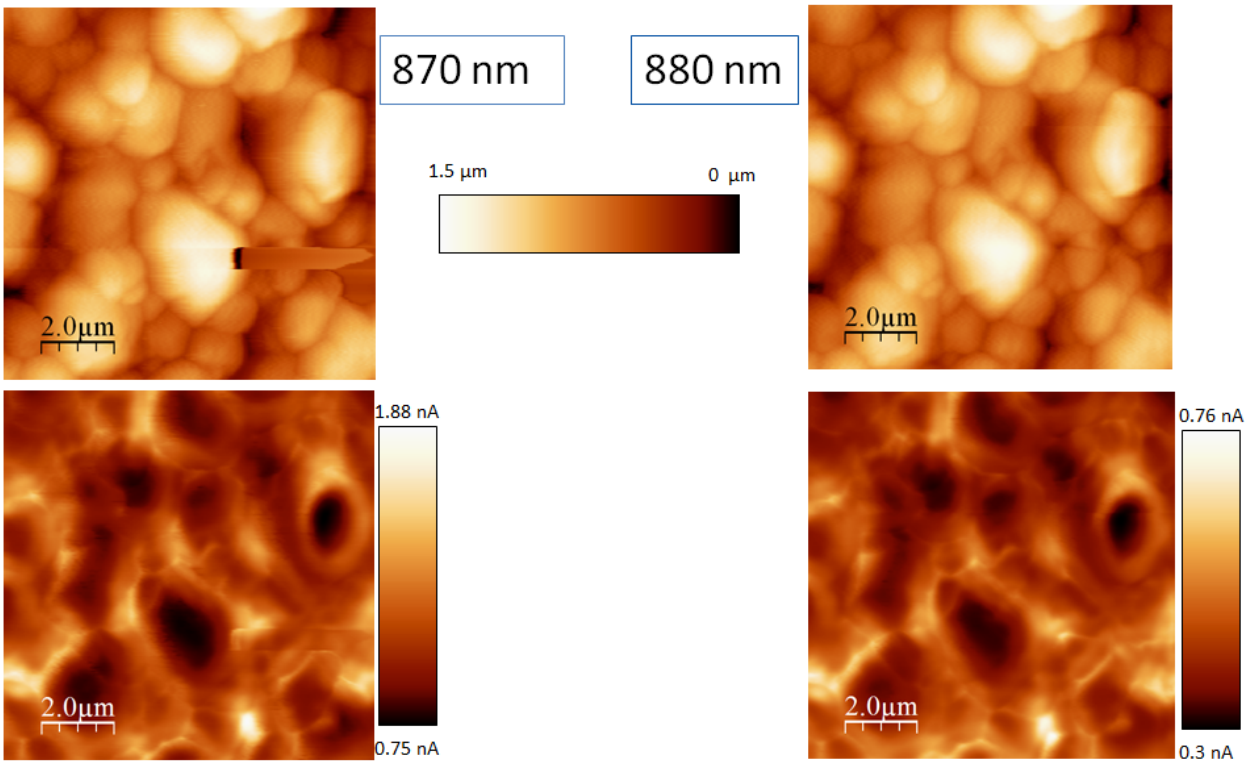

Figure 43: Simultaneously obtained topography (top) and photocurrent (bottom) images of CdTe topography. The image on the left was taken with a 870 nm optical band pass filter, and the image on the right was obtained with 880 nm. The scale bar in the middle of the image corresponds to both topography images.

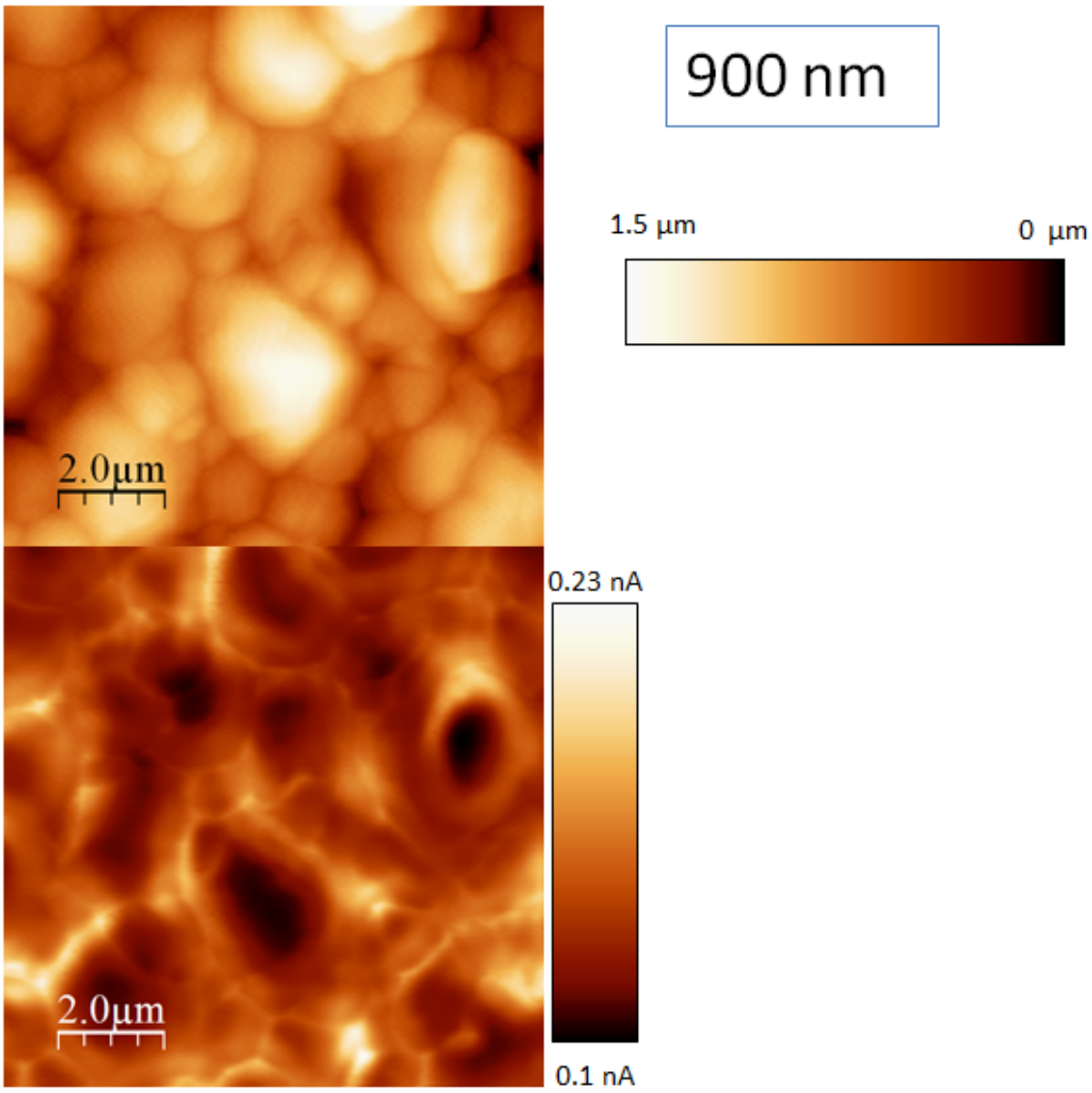

Figure 44: Simultaneously obtained topography (top) and photocurrent (bottom) images of CdTe topography. The image on the left was taken with a 900 nm optical band pass filter.

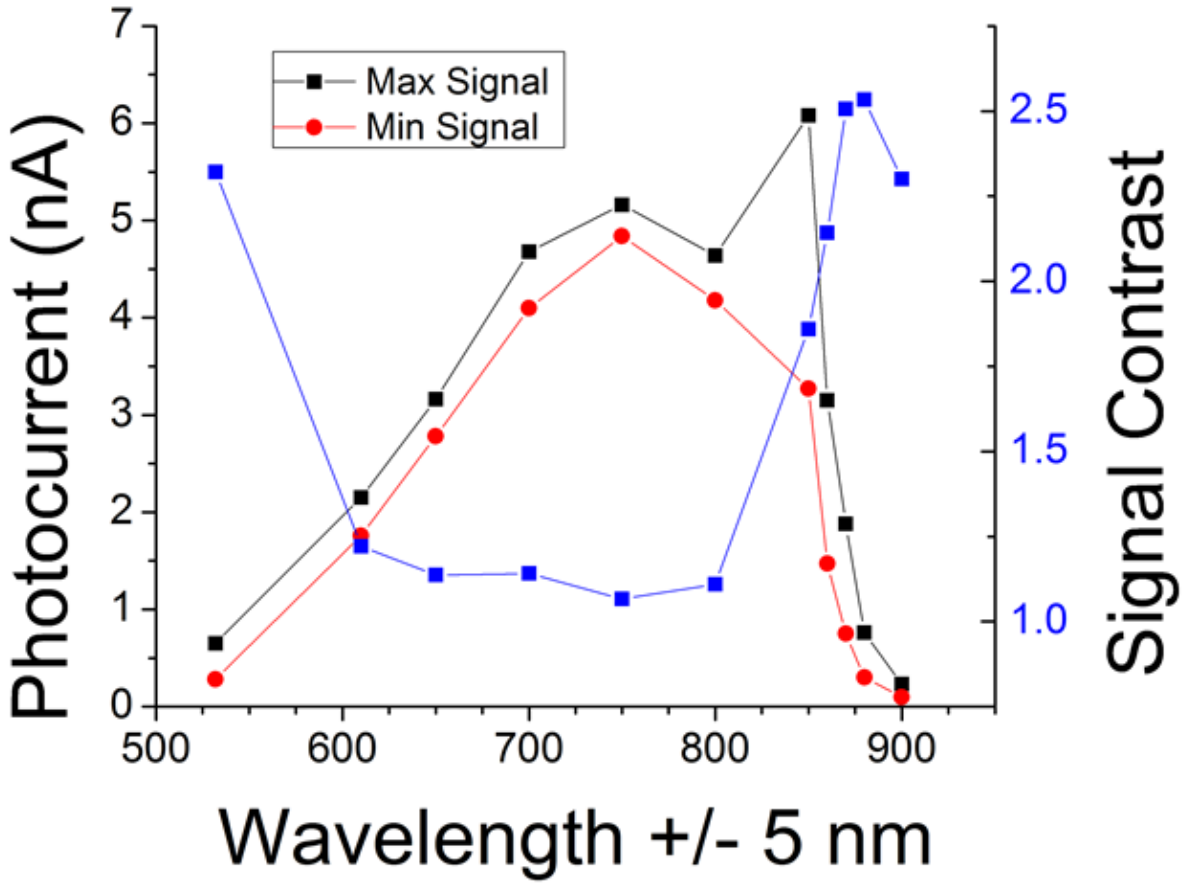

Figure 45: Plot of collected photocurrent versus incident wavelength. The right axis is max photocurrent divided by the min at each incident wavelength.

A.2 Focus Ion Beam Wedge into CdTe Surface : Spot 1

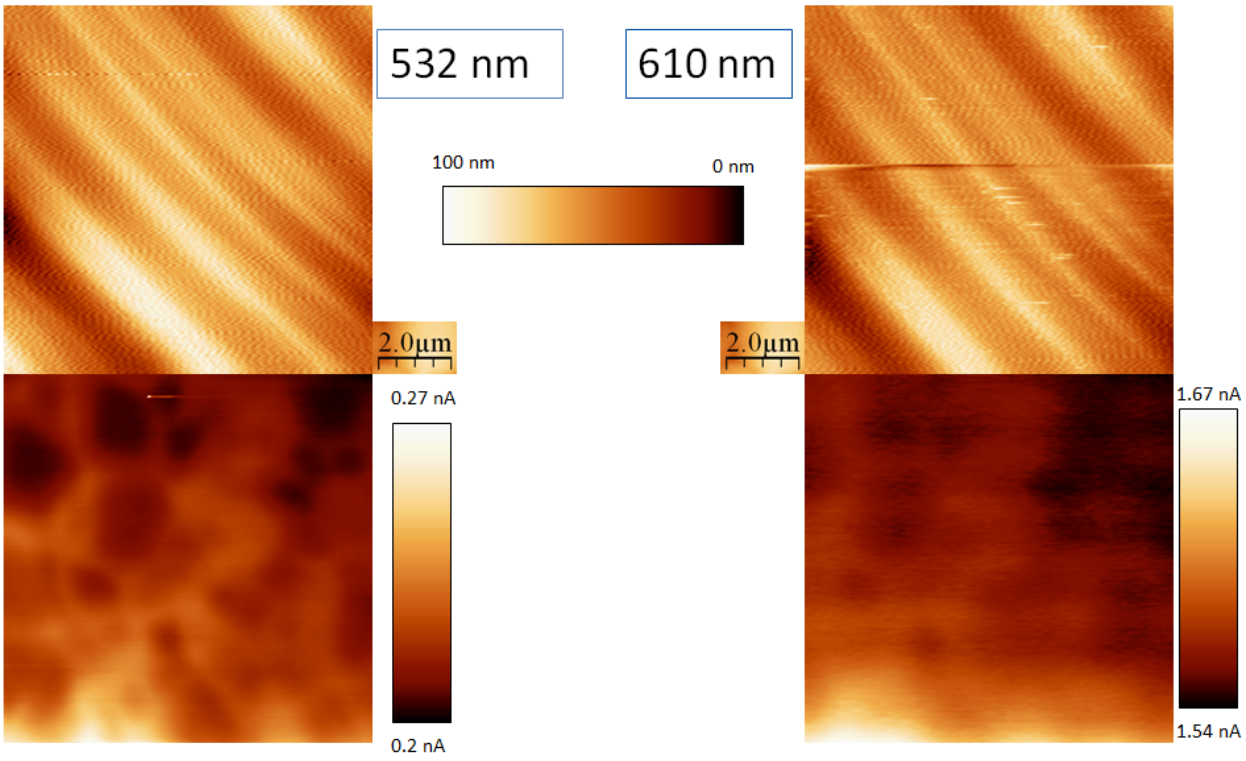

Figure 46: Simultaneously obtained topography (top) and photocurrent (bottom) images of CdTe topography. The sample substrate has a wedge, using focused ion beam, to eliminate topographic effects. The image on the left was taken with a 532 nm optical band pass filter, and the image on the right was obtained with 610 nm. The scale bar in the middle of the image corresponds to both topography images.

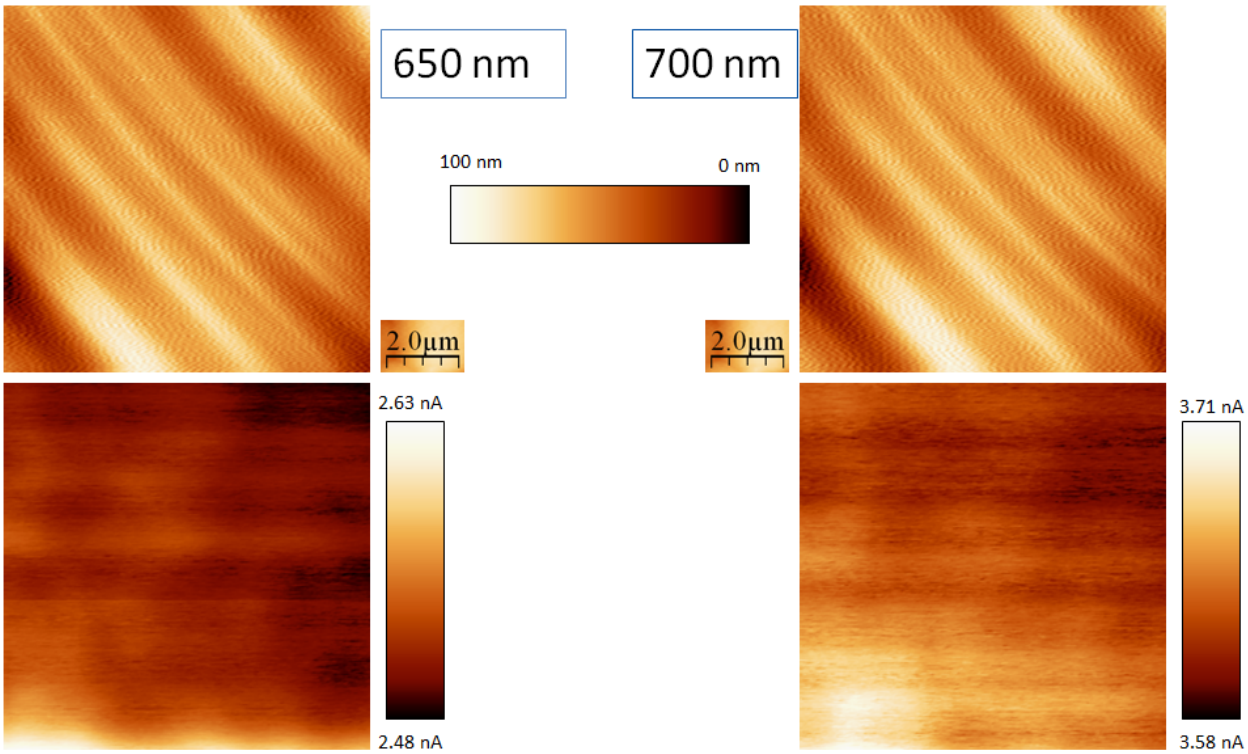

Figure 47: Simultaneously obtained topography (top) and photocurrent (bottom) images of CdTe topography. The sample substrate has a wedge, using focused ion beam, to eliminate topographic effects. The image on the left was taken with a 650 nm optical band pass filter, and the image on the right was obtained with 700 nm. The scale bar in the middle of the image corresponds to both topography images.

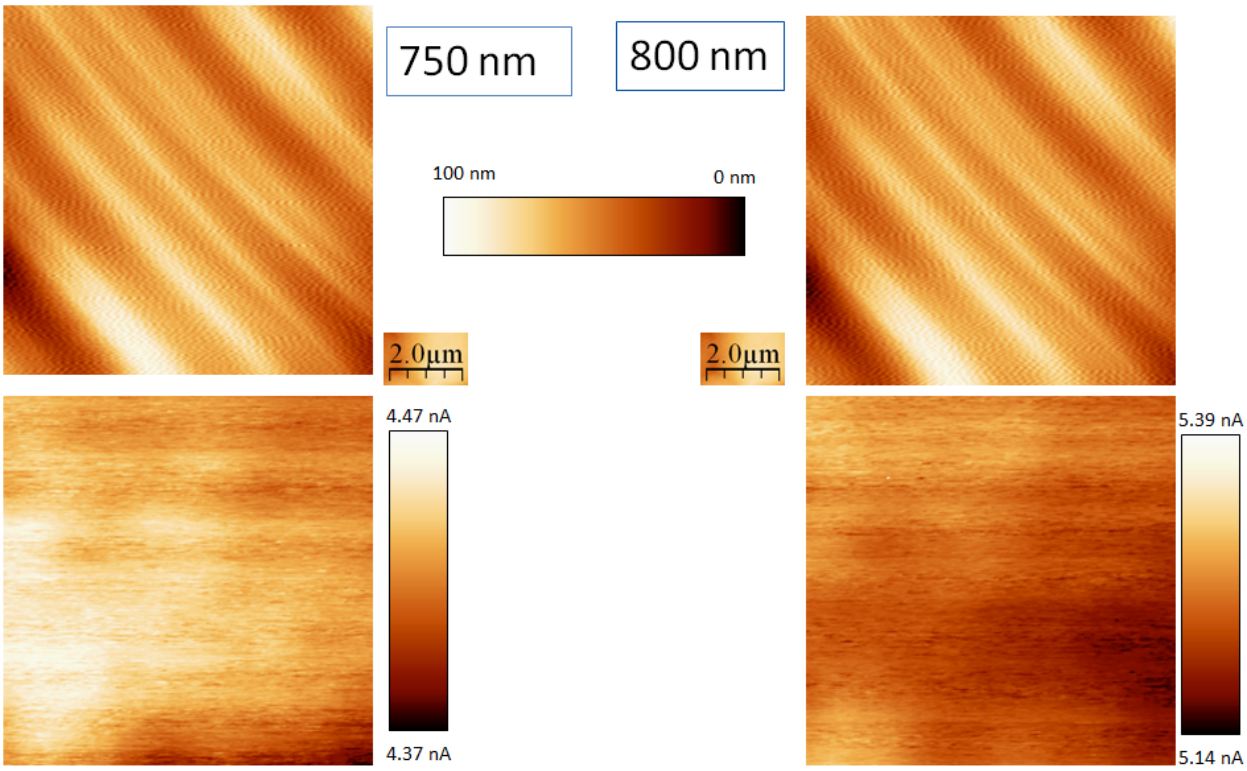

Figure 48: Simultaneously obtained topography (top) and photocurrent (bottom) images of CdTe topography. The sample substrate has a wedge, using focused ion beam, to eliminate topographic effects. The image on the left was taken with a 750 nm optical band pass filter, and the image on the right was obtained with 800 nm. The scale bar in the middle of the image corresponds to both topography images.

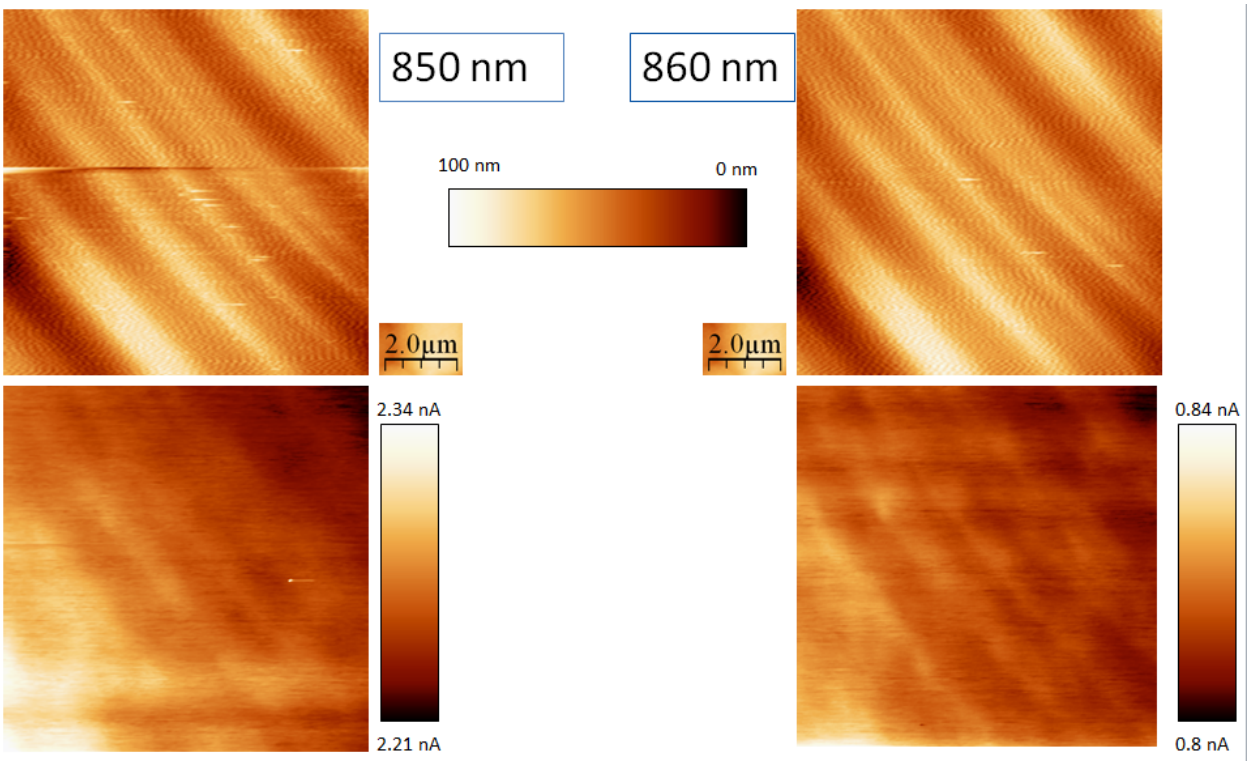

Figure 49: Simultaneously obtained topography (top) and photocurrent (bottom) images of CdTe topography. The sample substrate has a wedge, using focused ion beam, to eliminate topographic effects. The image on the left was taken with a 850 nm optical band pass filter, and the image on the right was obtained with 860 nm. The scale bar in the middle of the image corresponds to both topography images.

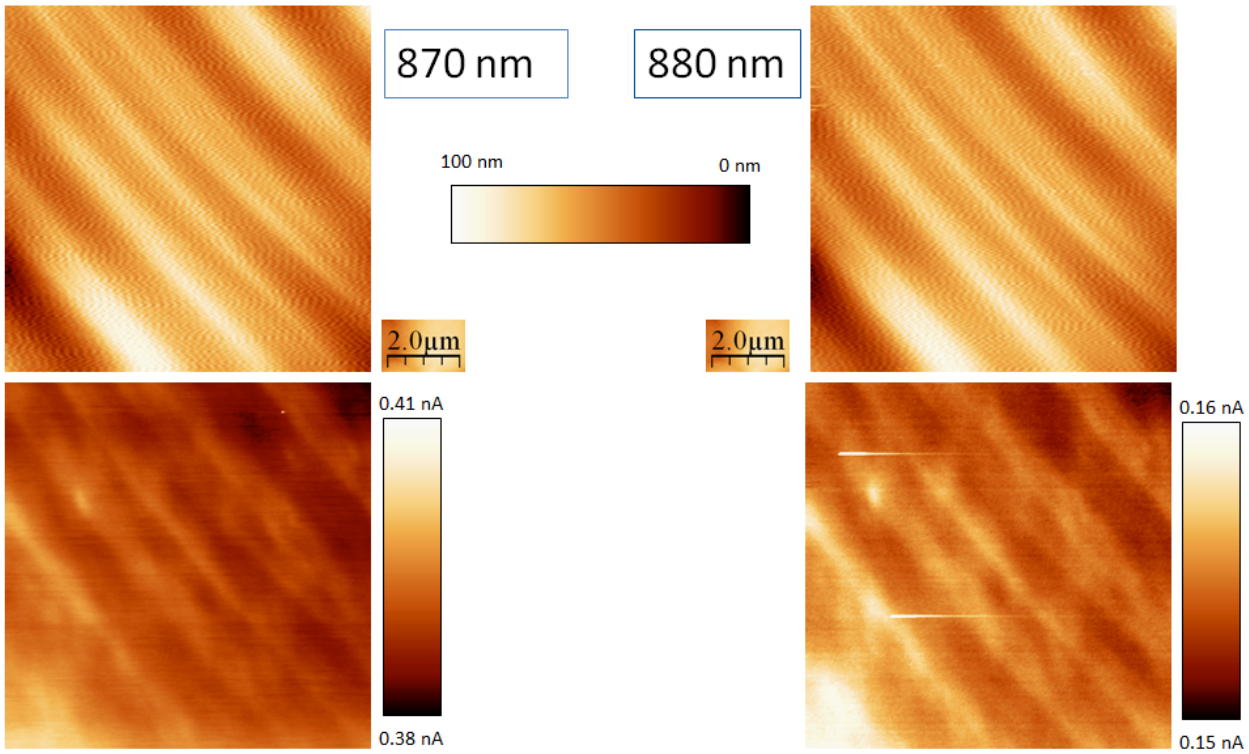

Figure 50: Simultaneously obtained topography (top) and photocurrent (bottom) images of CdTe topography. The sample substrate has a wedge, using focused ion beam, to eliminate topographic effects. The image on the left was taken with a 870 nm optical band pass filter, and the image on the right was obtained with 880 nm. The scale bar in the middle of the image corresponds to both topography images.

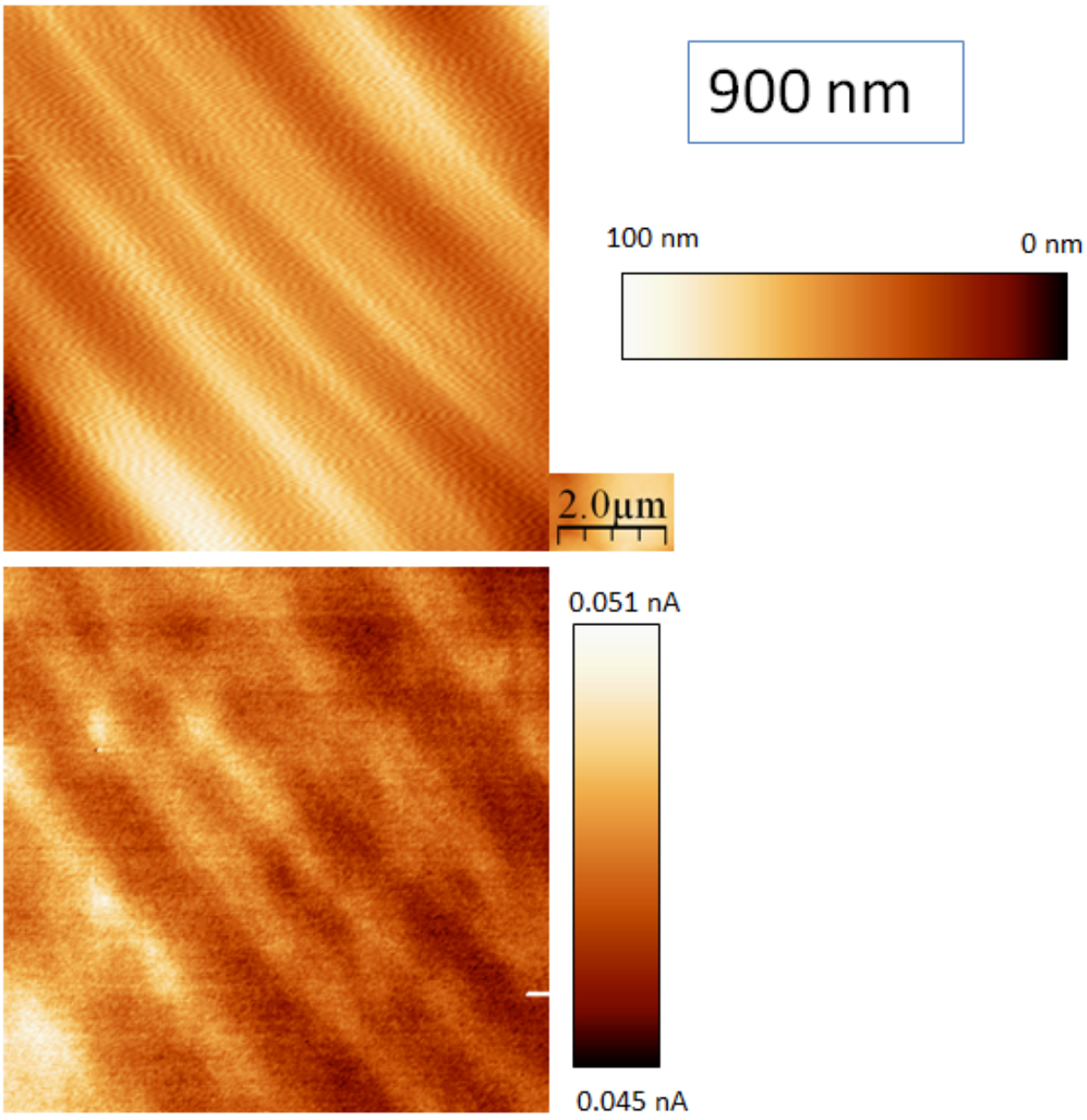

Figure 51: Simultaneously obtained topography (top) and photocurrent (bottom) images of CdTe topography. The sample substrate has a wedge, using focused ion beam, to eliminate topographic effects. The image was taken with a 900 nm optical band pass filter.

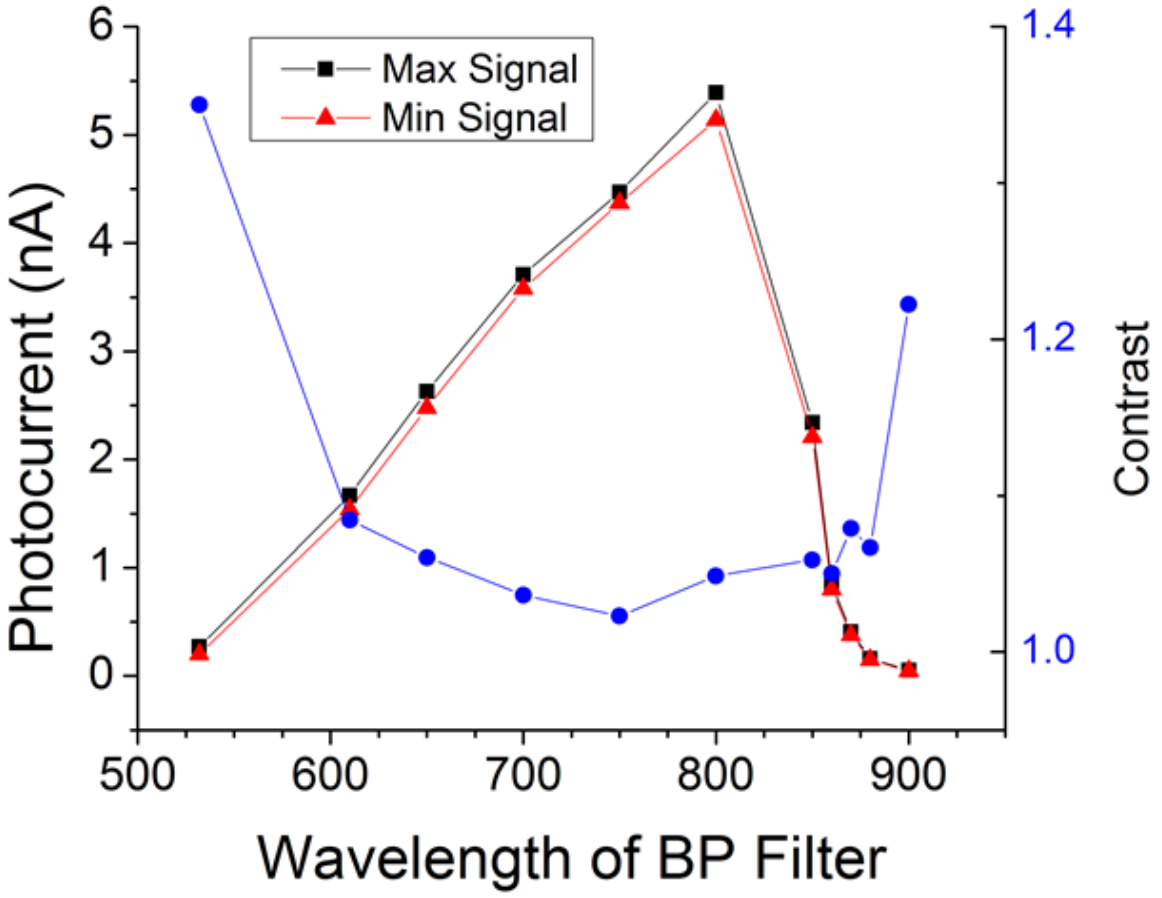

Figure 52: Plot of collected photocurrent versus incident wavelength. The right axis is max photocurrent divided by the min at each incident wavelength.

A.3 Focus Ion Beam Wedge into CdTe Surface : Spot 2

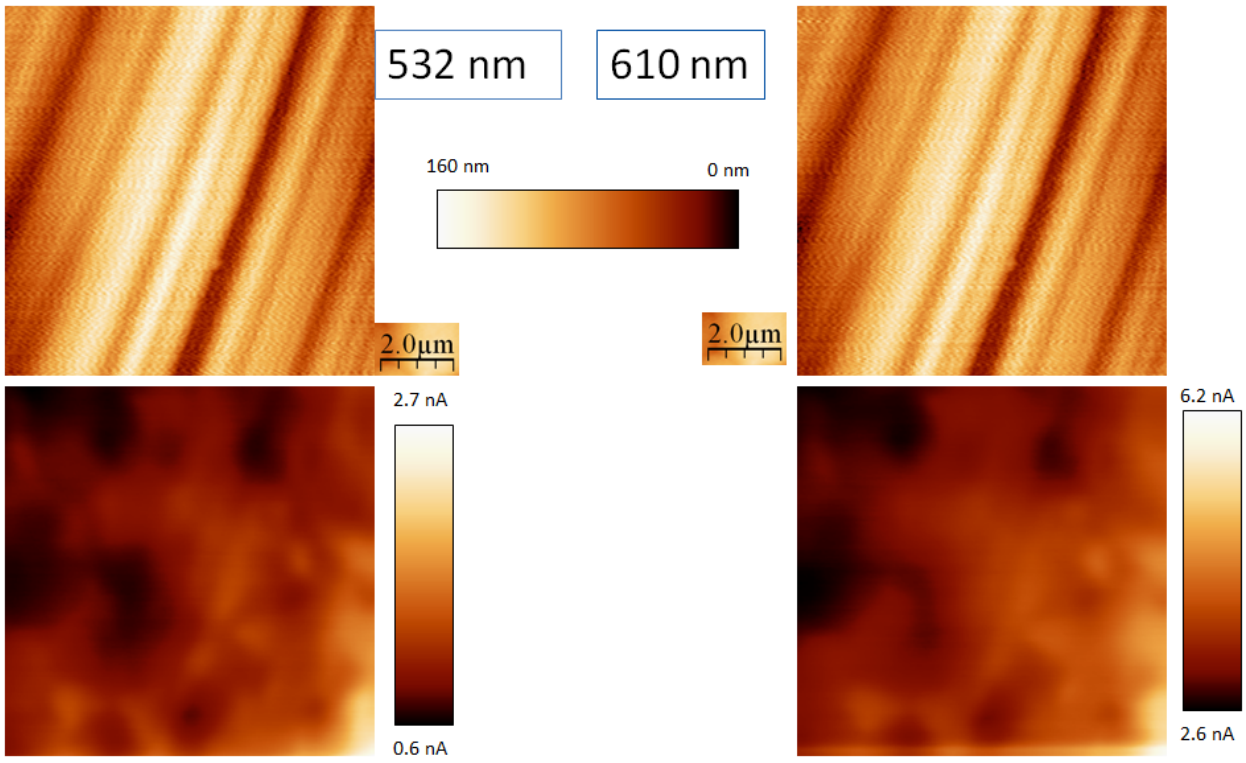

Figure 53: Simultaneously obtained topography (top) and photocurrent (bottom) images of CdTe topography. The sample substrate has a wedge, using focused ion beam, to eliminate topographic effects. The image on the left was taken with a 532 nm optical band pass filter, and the image on the right was obtained with 610 nm. The scale bar in the middle of the image corresponds to both topography images.

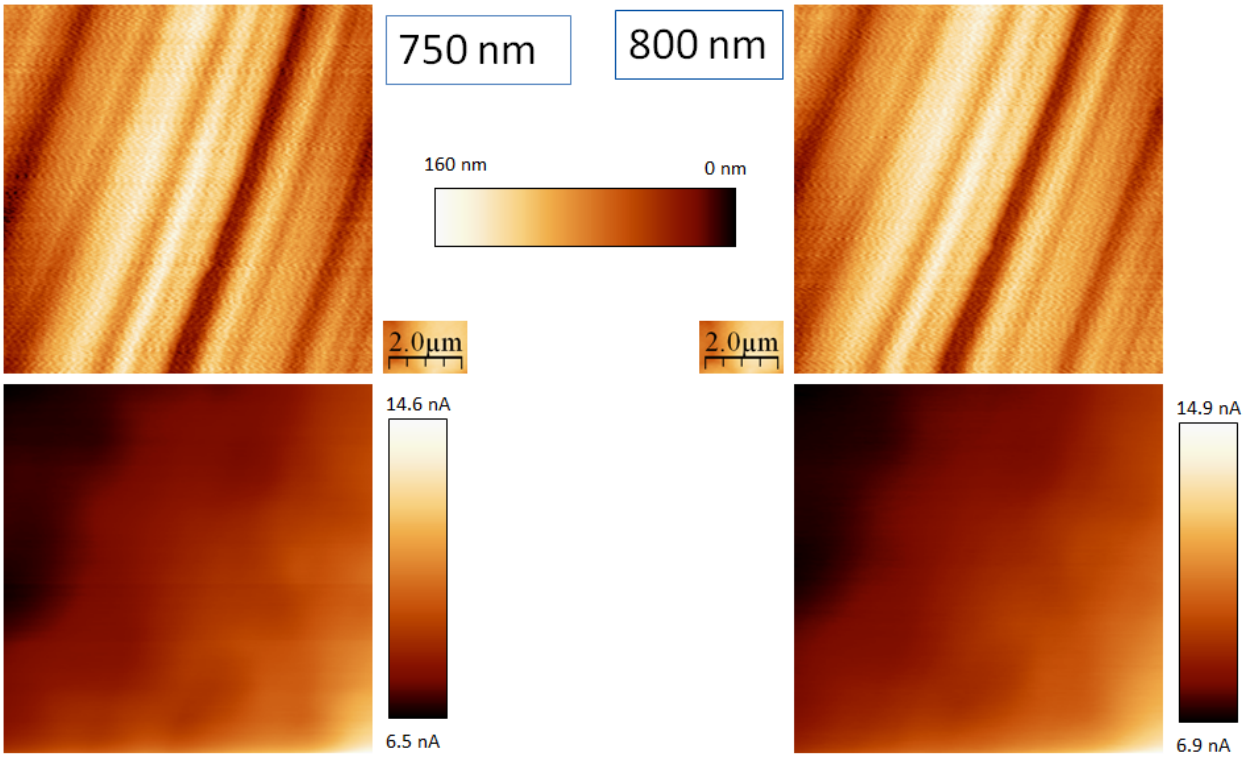

Figure 54: Simultaneously obtained topography (top) and photocurrent (bottom) images of CdTe topography. The sample substrate has a wedge, using focused ion beam, to eliminate topographic effects. The image on the left was taken with a 750 nm optical band pass filter, and the image on the right was obtained with 800 nm. The scale bar in the middle of the image corresponds to both topography images.

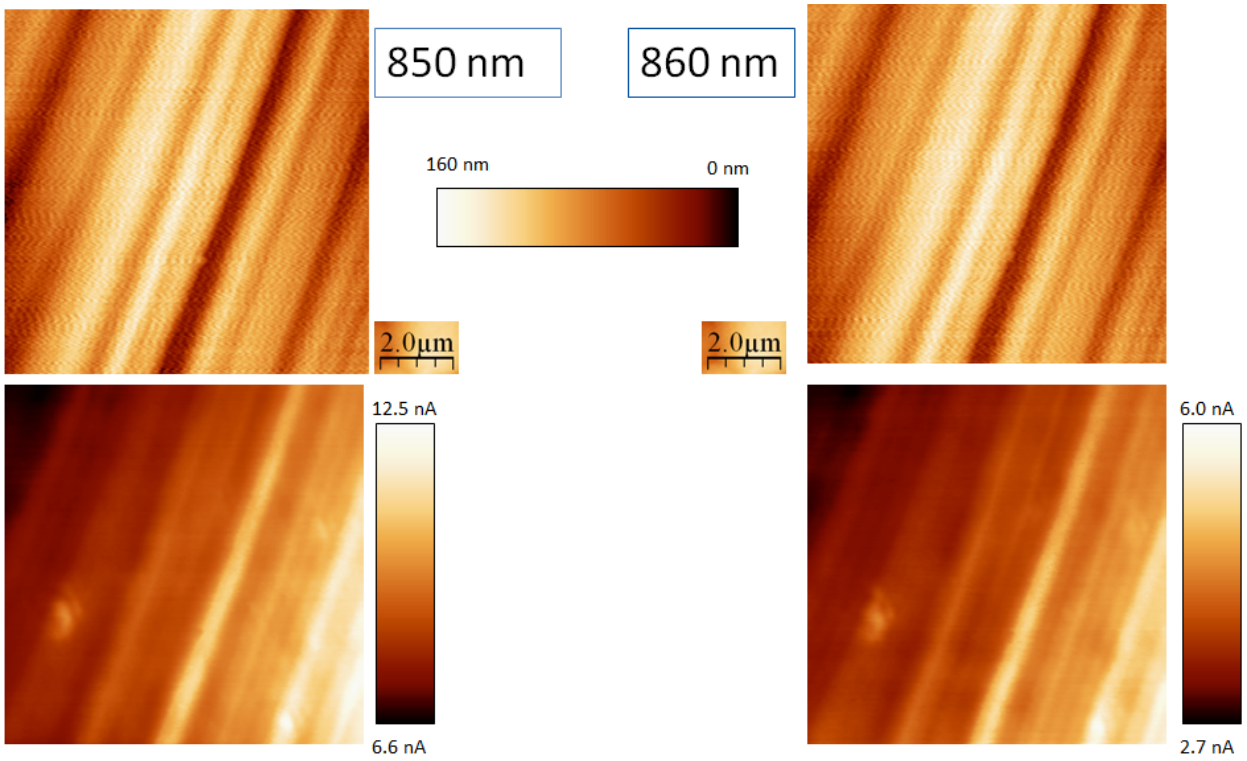

Figure 55: Simultaneously obtained topography (top) and photocurrent (bottom) images of CdTe topography. The sample substrate has a wedge, using focused ion beam, to eliminate topographic effects. The image on the left was taken with a 850 nm optical band pass filter, and the image on the right was obtained with 860 nm. The scale bar in the middle of the image corresponds to both topography images.

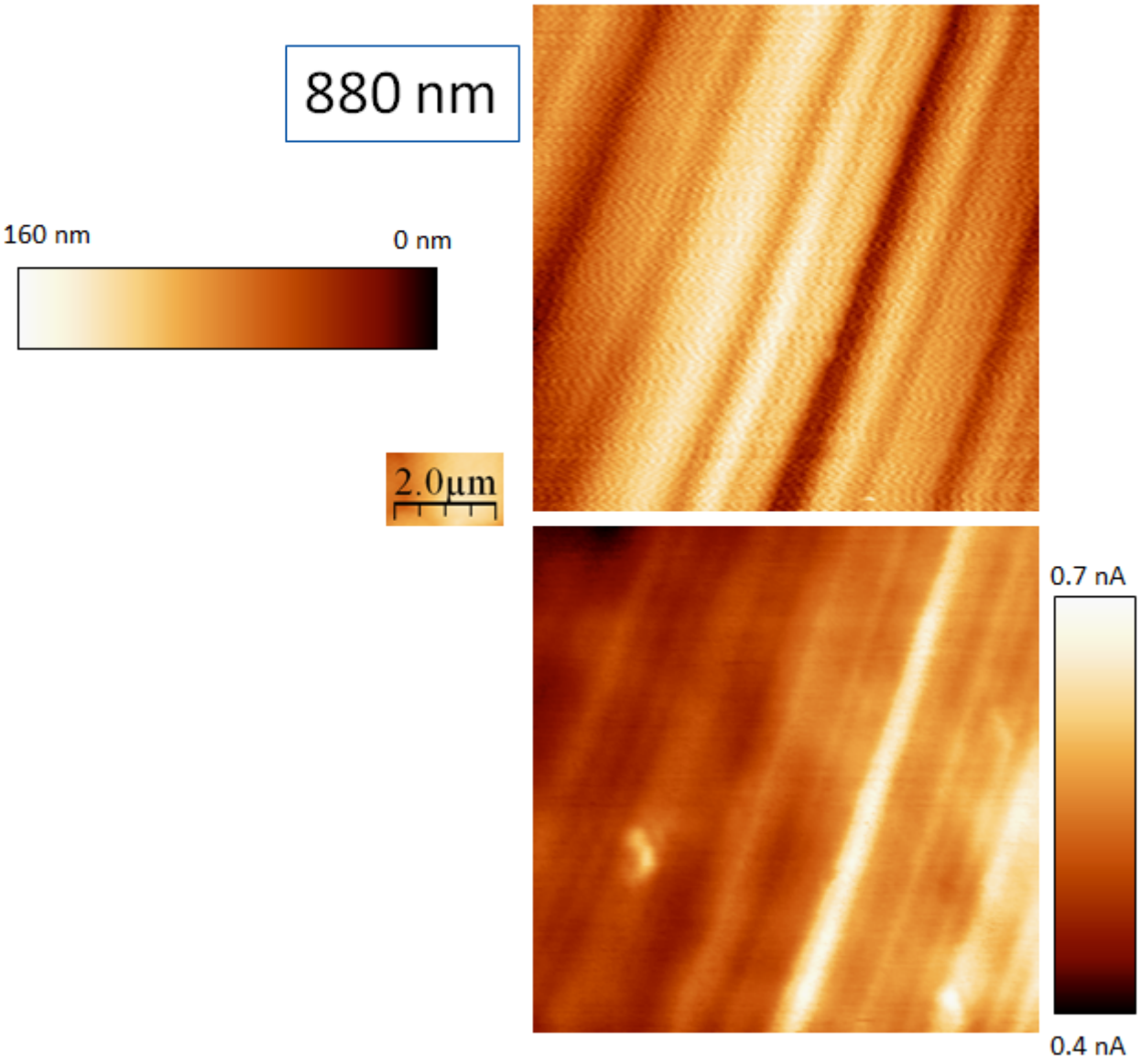

Figure 56: Simultaneously obtained topography (top) and photocurrent (bottom) images of CdTe topography. The image on the left was taken with a 880 nm optical band pass filter.

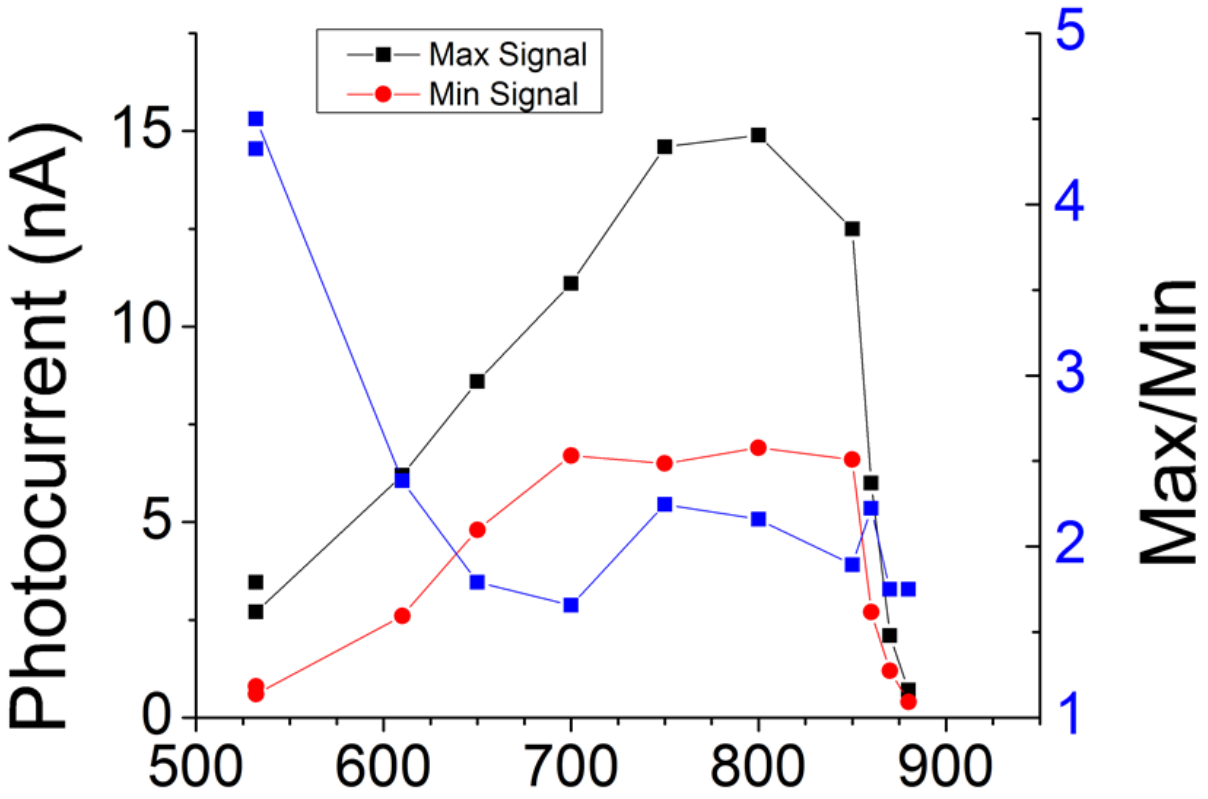

Figure 57: Plot of collected photocurrent versus incident wavelength. The right axis is max photocurrent divided by the min at each incident wavelength.

B Device Performance

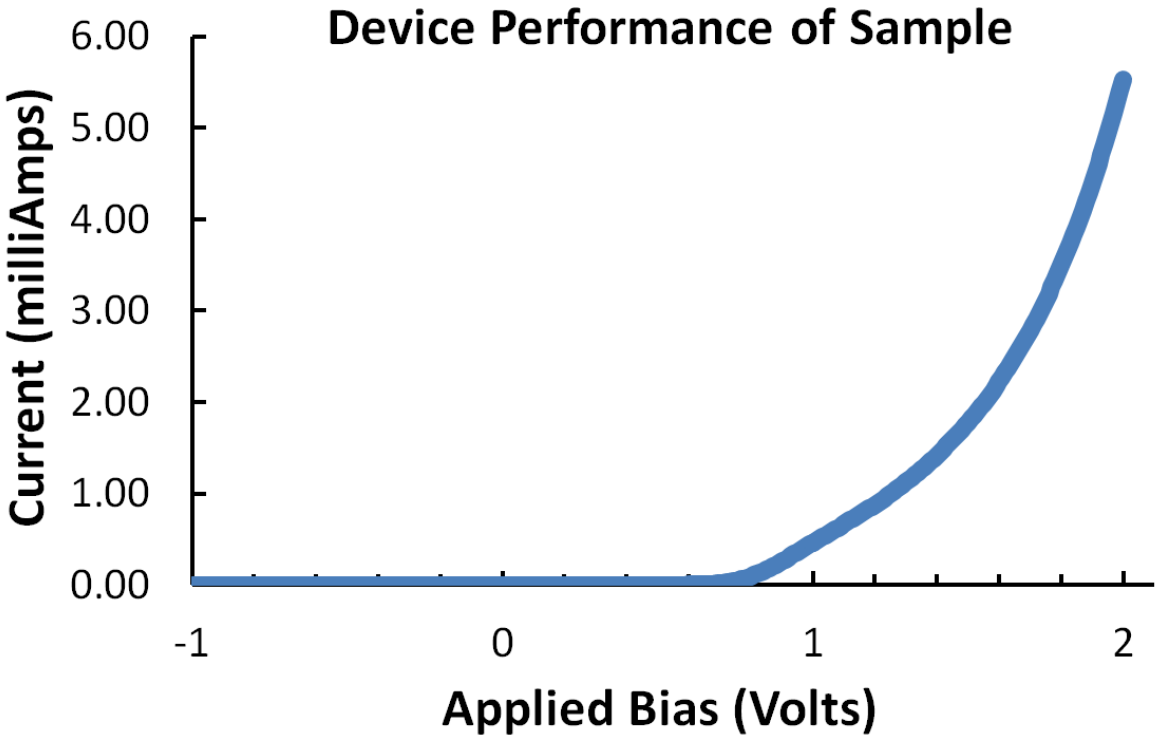

Figure 58: The dark IV curves of the sample used in this experiment. This plot shows that the device kept its diode behavior even after sample fabrication.

C Presentation Materials

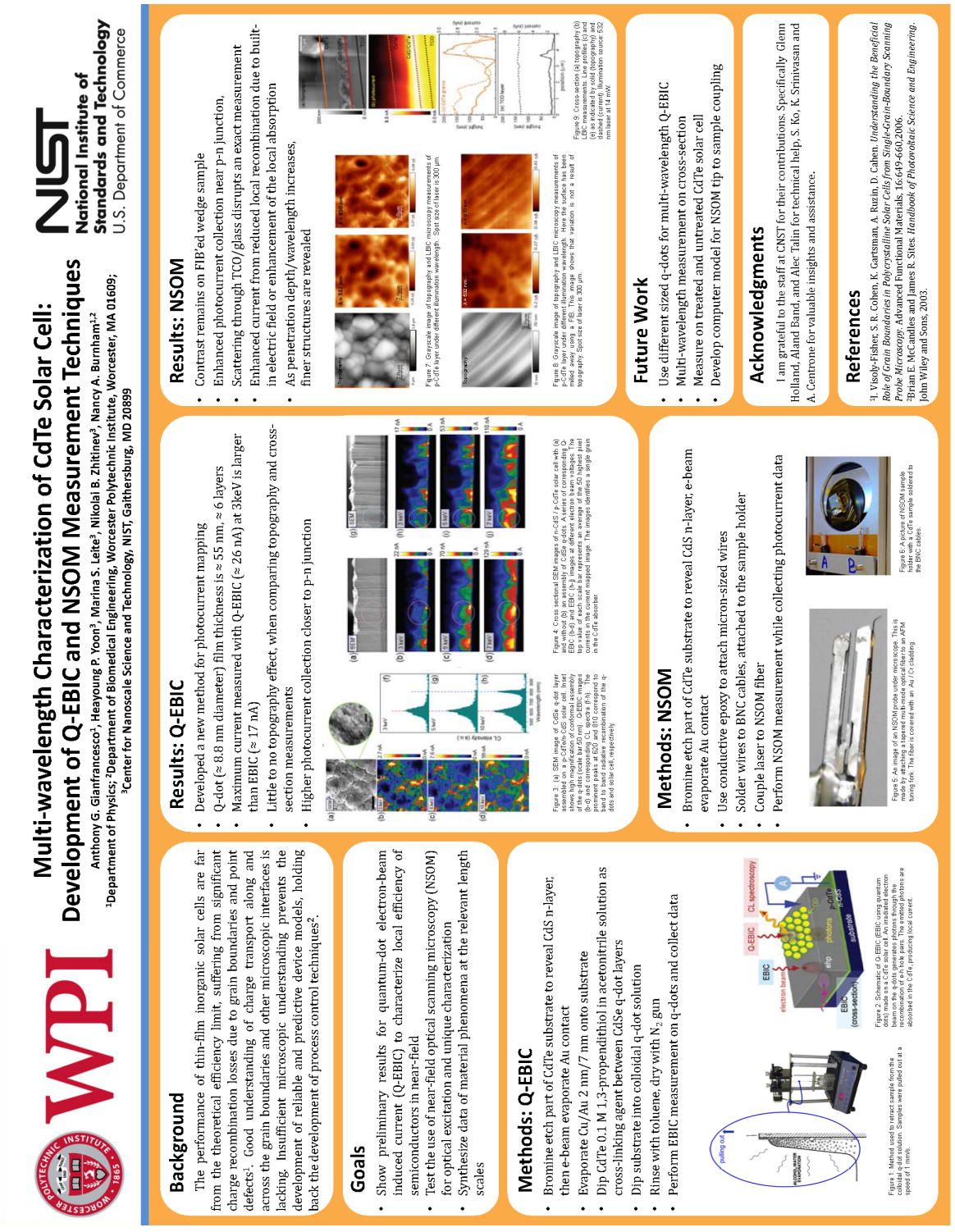

Figure 59: Poster used for presentation at GRAD 2013, graduate student poster presentation, at Worcester Polytechnic Institute in Worcester, MA.

D Detailed Sample Preparation

NSOM Sample Preparation

a. Take a commercially purchased CdTe module. Separate CdTe from bottom piece of glass, so that the CdTe (p-side) is bare.
    i. Strip Glass of solar panel to reveal p-layer side
    ii. Cut into small pieces (approx. 3mm squares)
b. Down etch the CdTe to reveal the CdS layer of the solar cell
    i. Cover a selected polished area with black wax (get chemical name)
        1. Mix hard wax with TCE to soften it
        2. This allows the black wax to be painted onto the CdTe
    ii. Mix 10 parts methanol to 1 part bromine
    iii. Submerge the partially covered CdTe into the methanol/bromine solution.
    iv. Let sit for 5-10 min, partially stirring/moving sample to remove etched pieces of CdTe.
        1. Bromine will not etch into the CdS
    v. Take the CdTe out of the bromine/methanol mixture and wash off black wax with TCE.
c. Inspect CdTe etched surface with SEM to see if it contains any particles that aren't CdTe, or to inspect small (1 nm) and large (1 um) scratches.
    i. What kind of contaminates can reside on the surface after polishing and etching?
d. Use E-beam Evaporator to place Platinum (Pt) contact(s) on clean areas of CdTe.
    i. Create a shadow mask of the shape of contact you would want to use
    ii. Use the e-beam evaporator in the clean room to put the platinum on the CdTe.
e. Test to see if contacts/solar cell are working properly using the probe station.
    i. Shunt resistance
    ii. Short circuit resistance
    iii. Rough Fill factor
f. Glue gold (Au) wires to Pt contacts using EPO-TEK E4110 Epoxy
    i. Mechanically rigid
    ii. Very conductive
g. Test wire contact using probe stations
    i. Shunt R
    ii. Short R
    iii. FF
    iv. Compare to values in step 6 to see if you did a bad job attaching wires
h. Solder Au wires to NSOM BNC holder using indium solder, then test with voltmeter for connection, test also on probe station.
i. Sample is ready for NSOM measurement

Figure 60: Detialed list of sample preparation steps for NSOM sample fabrication.